Final Progress Report

Project Title
Wearable Microsystem for Continuous Multi-Vapor Monitoring

Principal Investigator
Edward T. Zellers, PhD, Professor
Department of Environmental Health Sciences
1415 Washington Heights
University of Michigan, Ann Arbor, MI
ezellers@umich.edu; 734-936-0766

Institution Awarded
University of Michigan
School of Public Health
1415 Washington Heights
Ann Arbor, MI, 48109-2019

Co-Investigators
Stuart A. Batterman, PhD, Professor
Department of Environmental Health Sciences
University of Michigan, Ann Arbor, MI

Katsuo Kurabayashi, PhD, Professor
Department of Mechanical Engineering
University of Michigan, Ann Arbor, MI

Collaborator/Sub-Contractor:
William Steinecker, PhD
VGC Chromatography/TCM Global, LLC.
531 E. Third St., Dayton, OH

Sponsor
National Institute of Occupational Safety and Health
of the Centers for Disease Control and Prevention

Grant
R01-OH-010297

Project Period
September 1st, 2013 – August 31st, 2017

Report Submitted
July 23rd, 2018

Table of Contents

List of Abbreviations

ACE	Acetone
ARM	STM32F303 microcontroller
BAC	Butyl acetate
BEN	Benzene
BTEX	Benzene, toluene, ethylbenzene, and xylene
BTM	Band trajectory model
C_0	Inlet concentration to µPCF
C_{10}	n-Decane
C_{11}	n-Undecane
C_{12}	n-Dodecane
C_5	n-Pentane
C_7	n-Heptane
C8	n-Octanethiol
C-B	Carbopack B
C-C	Carbopack C
C-F	Carbopack F
C_i	Heat capacity of µcolumn segment i
CSV	Comma-separated values
CUM	Cumene
C_x	Downstream concentration from µPCF
C-X	Carbopack X
d	Effective inner diameter of the µcolumn
DAQ	Digital-to-analog-converter
DCM	Dichloromethane
DE	Desorption efficiency
DEE	Diethyl ether
d_Q/d_t	Rate of heat flow
DRIE	Deep-reactive-ion etching
EAC	Ethyl acetate
EBK	3-Heptanone
$Ecij$	Energy lost to the adjacent segments
EDM	Electrical discharge machining
E_G	Energy required for a separation via global heating
E_{ij}	Energy consumed to raise the segment to a specified set-point temperature
EOE	Isooctyl-3-mercaptopropionate
E_R	Fract. energy reduction due to zone (vs. global) heating

ETB	Ethylbenzene
E_Z	Energy required for a separation via zone heating
fwhm	Full width at half-maxima
GC	Gas chromatography
GC-MS	GC-mass spectrometer
GUI	Graphical user interface
H	Height equivalent to a theoretical plate
HME	Methyl-6-mercaptohexanoate
H_{min}	Minimum plate height
IDE	Interdigital electrode
ISR	Instrument scheduling routine
k	Retention factor
L	Length of the µcolumn
LIM	d-Limonene
LOD	Limit of detection
M	Temperature ramp rate
MBK	2-Hexanone (Methyl n-butyl ketone)
MC-EDPCR	Monte Carlo simulations coupled with extended disjoint principal components regression
MCR	Multivariate curve resolution
MEK	2-Butanone (methyl ethyl ketone)
MIBK	4-Methyl-2-pentanone (methyl isobutyl ketone)
MIMO	Multiple-input/multiple-output
MOH	Methanol
MPN	Thiolate-monolayer protected gold nanoparticle
N	Total number of theoretical plates
NBZ	Nitrobenzene
N_{max}	The maximum plate count
OPH	1-Mercapto-6-phenoxyhexane
P	The ratio of p_i/p_o
p_0	Outlet pressure
PCA	Principal comment analysis
PCB	Printed circuit board
P_{ci}	Added power to compensate for inter-segment heat transfer
PDMS	Polydimethylsiloxane
PEMM	Personal Exposure Monitoring Microsystem
PF	Preconcentration factor
P_i	Power of µcolumn segment i
p_i	Sum of p_o and applied pressure at the GC injection port

Pi/o	Inlet:outlet pressure ratio
PIC32	PIC32MX320 microcontroller
PID	Proportional-integral-derivative
PIN	α-Pinene
p_o	Atmospheric pressure
ppb	Parts-per-billion
PPB	n-Propylbenzene
ppm	Parts-per-million
PWM	Pulse-width modulated
R_b	Baseline resistance
R_c	Resistance to heat transfer between µcolumn segments
R_{ci}	Inter-segment resistance to heat transfer
R_i	Thermal resistance of each µcolumn segment i
RIE	Reactive-ion-etched
RP	Raspberry Pi
RR	Recognition rate
R_s	Chromatographic resolution
RTD	Resistance temperature detector
S/N	Signal to noise ratio
t_a	Entire analysis time or retention time of the analyte of lowest volatility
TCB	1,2,4-Trichlorobenzene
TCE	Trichloroethylene
TEG	1-Mercapto-(triethylene glycol) methyl ether
t_h	Retention time of the analyte of highest volatility
t_i	Time window when segment i is heated
TLV	Threshold Limit Value
TLV-STEL	Short Term Exposure Limit TLV
TLV-TWA	Time-Weighted Average TLV
t_M	Hold-up time
TMB	1,2,4-Ttrimethylbenzene
TOL	Toluene
t_R	Retention times
t_s	Segment heating time
$t_{x'}$	Total time for an analyte band to migrate a distance, x’
$\bar{u}_{opt}$	Optimal average velocity
V_{b10}	Breakthrough volume at $C_x/C_0 = 0.1$
VOC	Volatile organic compound

$WIMS^2$	Center for Wireless Integrated MicroSensing & Systems
XYL	m-Xylene
ZDV	Zero dead volume
ΔR	Resistance change
ΔV	Voltage change
η	Viscosity of the carrier gas
θ_c	Inter-segment temperature
θ_i	µColumn segment temperature
θ_s	Specified set-point temperature difference
σ_a	Average standard deviation
µCR	µChemiresistor
µGC	Gas chromatographic microsystem/microGC
µPCF	µPreconcentrator/focuser
µSC	µSeparation column

List of Figure Captions

2.4 Phase 1/Aim 1

benzene and trichloroethylene. Mass in b) is the average mass of trichloroethylene and benzene in the injection, and the binary mixture was in a 1.5:1 ratio, respectively, to account for differences in FID sensitivity (i.e., to maintain similar peak sizes).

Figure 1.11. Chromatograms of 25 compound hypothetical exposure scenario mixture, separated using Gen-1.5 2x3-m µcolumns with a) N2 b) He as carrier gases. Conditions: syringe injection, 3 mL/min, temperature programs were optimized for each chromatogram.

Figure 1.12. Photographs of a) original µPCF; b) a single-cavity device that will not be discussed in this report (on U.S. dimes for scale); and c) the µPCF inverted and mounted to a custom printed circuit board; device is suspended by the inlet/outlet capillaries that are epoxied to the board for mechanical and thermal isolation. Wire bonded leads are for (bulk) heating and for monitoring temperature via the patterned RTD extending into the center of the chip.

Figure 1.13. Desorption bandwidth (i.e., fwhm) from the µPCF as a function of flow rate for benzene (triangles), toluene (squares), and n-dodecane (circles), tested individually without a downstream column; FID. Error bars represent 95% confidence intervals (n=3). Curves represent the least-squares fits to the data. Inset shows the effect of the injection split-flow ratio (vent:analysis) on the fwhm values for benzene and n-dodecane; analytical path flow rate was maintained at 3.0 mL/min.

Figure 1.14. a) Superimposed chromatograms of benzene (1^{st} peak) and trichloroethylene (2^{nd} peak) collected at three flow rates (as indicated), with the corresponding R_s values for the pair. Samples of the binary vapor mixture (~50 ng each) were pre-loaded into µPCF-2, desorbed/injected splitless in He, and separated on a 6-m long, PDMS-coated capillary column isothermally at 30 °C; FID. b) R_s (squares), average peak height (circles), and average peak area (triangles) for benzene and trichloroethylene plotted as a function of the injection split-flow ratio (vent:analysis), with the column (analytical path) flow rate maintained at 3.0 mL/min.

Figure 1.15. Representative breakthrough curves of µPCF-2 challenged with a mixture of benzene, toluene, ethylbenzene and m-xylene (i.e., BTEX) at 1, 20, 20, and 100 ppm, respectively (i.e., TLV concentrations for all except benzene) in N_2. C_x/C_o is the breakthrough fraction. V_{b10} values for benzene (33 mL) and toluene (90 mL) are designated by the vertical arrows. V_{b10} values for ethylbenzene and m-xylene were > 150 mL. Conditions: flow rate = 5 mL/min; temperature = 30 ^{0}C; FID.

Figure 1.16. a) Breakthrough curves of µPCF challenged with the 17-VOC mixture (see Table 1.1 for acronym definitions) at 30 °C and 5 mL/min with C_o = 10 ppm for each compound; only the first seven compounds to break through were monitored. Shaded region corresponds to $V \leq V_{b10}$ for benzene. b) Chromatogram of a 20-mL sample of the same 17-VOC test atmosphere injected from µPCF-2 and separated on a 6-m capillary column; inset shows enlargement of the first seven compounds to elute (see Table 1 for peak # assignments). Conditions: 3 mL/min; 2:1 split injection; column held at 28 °C for 0.5 min, then 10 °C/min to 33 °C, then 50 °C/min to 125 °C.

Figure 1.17. Range of peak shapes among the µCR sensors in the array for the representative compound 2-hexanone (MBK, compound 13 in Table 1.4, t_R = 67 s) from calibration test series. From left to right, the sensor and corresponding peak

2.5 Phase 2/ Aim 2

2.6 Phase 3/Aim 3

2.7 Phase 4/Aim 4

List of Table Headings

2.4 Phase 1/Aim 1

2.5 Phase 1/Aim 2

2.6 Phase 3/Aim 3

2.7 Phase 4/Aim 4

Project Title

Wearable Microsystem for Continuous Multi-Vapor Monitoring

Principal Investigator: Edward T. Zellers, PhD, Professor
Department of Environmental Health Sciences
1415 Washington Heights, University of Michigan, Ann Arbor, MI
ezellers@umich.edu; 734-936-0766

Abstract

This report concerns the successful development and characterization of a wearable prototype instrument that uses a gas chromatographic microanalytical system (μGC) for near-real-time recognition and quantification of the components of moderately complex mixtures of airborne volatile organic compounds (VOC) encountered in working environments. Over the course of the project, we developed new microfabricated (Si-glass) components for preconcentration/injection, separation, and detection, and we assembled and characterized the performance of two prototype μGC-based instruments, referred to as Personal Exposure Monitoring Microsystems (PEMM). The first prototype, PEMM 1, is a compact benchtop instrument that operates on AC power and is controlled by a laptop computer through a graphical user interface. The second prototype, PEMM 2, is a belt-mountable, battery powered instrument run by an embedded microcontroller. PEMM 1 is the progenitor of PEMM 2 and both instruments can operate autonomously.

Innovative designs and strategies were implemented to create the component devices and configurations used in both prototypes. For both PEMM 1 and PEMM 2, a simple wall-coated capillary pre-trap is used to selectively retain intractable (low-volatility) interferences, and then purge them at room temperature between sequential measurements. VOCs above a threshold vapor pressure (p_v) of ~0.03 kPa pass into the partially selective, dual-adsorbent micro-preconcentrator/focuser (μPCF). Those vapors with p_v values from 0.03 to ~13 kPa are quantitatively trapped, focused, and injected into the downstream microcolumn(s). For PEMM 1, a pair of series-coupled μcolumn chips with integrated heaters and temperature sensors and stationary phase of cross-linked polydimethylsiloxane (PDMS) is used for temperature-programmed chromatographic separations. For the PEMM 2, a single μcolumn chip with three independently heated zones is used to afford more power-efficient, high-resolution, high-speed separations of VOC mixture components. For both prototypes, detection is achieved with an array of 4-5 microsensors comprising chemiresistors with monolayer protected nanoparticle interface layers. By using differently functionalized monolayers on the nanoparticles, each eluting VOC generates a set of responses from the array that differ from the set of responses for other VOCs. Detection limits in the sub-ppm range are achieved for all vapors from collected air samples of 5-10 mL. By combining retention times and response patterns, it is possible to differentiate and recognize all of the VOCs in a mixture.

The μGC components of the PEMM 2 are combined with a commercial mini-pump, a small on-board He gas supply, mini-valves, interface circuitry, an embedded microcontroller for operating the instrument, and a mediated wireless link for and storing exposure data and post-shift downloading of data to a remote host computer. Subsequent chemometric analysis of the chromatographically resolved array response patterns for each mixture component permits construction of time-exposure profiles for comparison with occupational exposure limits or classification of exposure frequencies and intensities for epidemiologic studies. The PEMM 2 is powered by a separate battery pack and is small/light-weight enough to mount on the belt of a worker. It is capable of simultaneous personal exposure measurements of at least 21 specific, user-selectable VOCs every 6-10 minutes. The capability for assessing worker exposures to VOCs was demonstrated through a series of mock-field tests. *No such instrument existed prior to this study.*

1. Findings and Impacts

1.1 Significant Findings

We designed, developed, and characterized the performance of two prototype multi-VOC analyzers referred to as Personal Exposure Monitoring Microsystems (PEMM): PEMM 1 is a compact portable instrument operated from a laptop computer and PEMM 2 is a belt-mounted prototype with embedded microcontrol. Both contain gas chromatographic microanalytical systems (μGC) and both are capable of the selective determination of multiple airborne volatile organic compounds (VOCs) at concentrations in the vicinity of recommended occupational exposure limits. The PEMM 2 fills the long-standing need for small, inexpensive, wearable, turn-key instrumentation capable of direct, autonomous identification/quantification of VOCs in complex workplace-air mixtures with high temporal resolution.

Numerous innovations were incorporated into the design and operating conditions of both prototype instruments. The core microsystems are similar in both prototypes and consist of a set of discrete Si-microfabricated devices: a dual-cavity, adsorbent-packed micro-preconcentrator/focuser (μPCF) chip that quantitatively captures and thermally desorbs/injects VOCs with vapor pressures between ~0.03 and 13 kPa; single or tandem μcolumn chips with cross-linked PDMS wall-coated stationary phase capable of temperature-programmed separations; and an integrated array of four or five μchemiresistors (μCR) coated with different thiolate-monolayer protected gold nanoparticle (MPN) interface films that quantifies and further differentiates among the analytes by virtue of the response patterns generated. Other components include a pre-trap for low-volatility interferences, a split-flow injection valve, and an onboard He carrier-gas canister.

The PEMM 1 unit measures 19×30×14 cm, weighs ~3.5 kg, operates on AC power, and is laptop/LabVIEW controlled. Component- and system-level tests of performance demonstrated injection bandwidths <1 sec, a μcolumn capacity of ≥8 μg injected mass, linear calibration curves, no apparent humidity effects, excellent medium-term (i.e., 1 week) reproducibility, autonomous operation for 8 hr, detection limits below Threshold Limit Values (TLV) for 10-mL air samples, and response patterns that enhanced vapor recognition. The determination of a 17-VOC mixture in the presence of 7 interferences was performed in 4 min.

Each PEMM 2 unit measures 20×15×9 cm, weighs 2.1 kg, is powered by a separate battery pack. System level performance tests demonstrated linear calibration curves, excellent medium-term (i.e., 1 week) reproducibility, autonomous operation for several hours, detection limits 10× lower than TLVs for 5-10 mL air samples and response patterns that enhanced vapor recognition. The determination of a 21-VOC mixture was performed in < 4 min. A series of mock-field tests showed highly accurate measurements of time-varying concentrations of simple VOC mixtures collected autonomously every 5 min.

In summary, the project has produced instrumentation with unprecedented capabilities for measuring individual worker exposures to multiple specific VOCs, with respect to accuracy, specificity, portability, temporal resolution, and the number of contaminants measured simultaneously.

1.2. Translation of Findings

The instruments developed in this project have unprecedented capabilities with respect to the quantitative measurement of individual components of multi-VOC mixtures at concentrations encountered in a wide range of workplaces. Such capabilities address the long-standing need for more and better-quality exposure data, which has been consistently cited as

the most critical factor limiting efforts to define exposure-response relationships in epidemiologic studies of disease in worker populations, particularly where complex mixtures are involved. This, in turn, greatly facilitates efforts to establish meaningful workplace exposure limits and to determine compliance with such limits once established. Results were published in conference proceedings papers and in peer-reviewed articles. Numerous invited and contributed conference presentations were delivered to national and international audiences comprising practitioners, researchers, advocacy groups, faculty members and students representing the disciplines or sub-disciplines of industrial hygiene, environmental science, environmental justice, analytical chemistry, sensor science, and microsystems engineering (among others). Presentations were also made to representatives of numerous private-sector technology companies with interests or exiting product lines in VOC monitoring instrumentation. The technology has also been discussed in seminars and courses on environmental monitoring and worker exposure assessment in the graduate-level curricula in Industrial Hygiene at the University of Michigan. Students involved in the project have included their investigations and results in their doctoral dissertations. Collaboration with a small company throughout the project spawned new business plans, proposals for funding, and collaborative business ventures in related application areas wherein this technology figured prominently. One of the doctoral students working on this project took a position with a major air-monitoring instrument manufacturer and another student is actively seeking investment funding for a start-up company focused on the instrumentation developed in this project.

1.3. Research Outcomes/Impact

The outcomes of this project would be classified as either “potential” or “intermediate”. No so-called “end outcomes” have been produced as yet. Innovative designs and strategies for selective, power-efficient, preconcentration/injection, high-resolution/high-speed separation, and microsensor-based detection with chemometric peak deconvolution have be implemented in the PEMM prototypes, and operating conditions are adjustable to permit accurate measurements of VOC concentrations spanning a >40-fold range for any compound. The capabilities of these instruments were demonstrated through laboratory calibrations and a series of mock-field tests using target and background VOC mixtures of varying complexity representative of those that might be encountered in several NIOSH-NORA-defined industry sectors. Thus, the project has yielded tools with unprecedented capabilities for measuring individual worker exposures to multiple specific VOCs, with respect to accuracy, specificity, portability, temporal resolution, and the number of contaminants measured simultaneously. In addition, the methods used in producing and optimizing the devices in the instrument, as well as the integration of all the devices, ancillary components, and software used to control the instrument and acquire data have been communicated to those in the research community who can benefit from them in taking this and similar technologies to the next stages of development.

This research addressed a strategic goal in the NIOSH *Exposure Assessment* Cross Sector and it also has indirect impact on the *Emergency Preparedness and Response* Cross Sector. In response to the NIOSH Research-to-Practice initiative, this project engaged a private-sector business partner to build the prototypes and facilitate commercialization, thereby making available a valuable addition to the repertoire of monitoring technologies used to assess worker exposures more frequently and accurately. The students working on this project have gained valuable experience in new technology development, instrument design/construction, data interpretation, and testing, which they have carried or will carry with them in their careers following graduation.

2. Scientific Report

2.1 Specific Aims

The broad goal of this project was to develop and characterize a wearable gas chromatographic microanalytical system (μGC) for near-real-time recognition and quantification of the components of moderately complex mixtures of volatile organic compounds (VOC) encountered in working environments. The proposed μGC, referred to as a Personal Exposure Monitoring Microsystem (PEMM), would be battery operated, autonomous, and small/light-weight enough to mount on the belt of a worker, yet capable of simultaneous personal exposure measurements of at least 10-15 specific, user-selectable VOCs every 10-15 minutes in a complex matrix of background VOCs. Wireless communication would facilitate display via smart-phone and post-exposure data analysis by a remote host computer.

The performance of the PEMM would rely on an ensemble of Si-microfabricated devices for selective sampling/preconcentration, focused injection, temperature-programmed chromatographic separation, and 'spectral detection' with a microsensor array. These were to be combined with a commercial mini-pump, possibly a small on-board He gas supply, mini-valves, interface circuitry, an embedded microcontroller for operating the instrument and storing exposure data, and a wireless link for post-shift or on-the-fly downloading of data to a remote host computer. Off-line chemometric analysis of the chromatographically resolved array response patterns for each mixture component would permit construction of time-exposure profiles for comparison with occupational exposure limits or classification of exposure frequencies and intensities for epidemiologic studies.

Innovative designs and strategies for selective, power-efficient, preconcentration/ injection, high-resolution/high-speed separation, and microsensor-based detection with chemometric vapor recognition would be implemented in the PEMM, and operating conditions were to be adjustable to permit accurate measurements of VOC concentrations spanning a ~100-fold range for any compound, with detection limits as low as 0.05 ppm achievable for compounds (e.g., benzene) with sub-ppm exposure guidelines, or higher for others.

The capability of this instrument for assessing human exposures to VOCs was to be demonstrated through laboratory calibrations and a series of mock-field tests using target and background VOC mixtures of varying complexity representative of those that might be encountered in NORA-defined construction, manufacturing, and health care sectors. The successful project was to yield a tool with unprecedented capabilities for measuring individual worker exposures to multiple specific VOCs, with respect to accuracy, specificity, portability, temporal resolution, and the number of contaminants measured simultaneously. This would address one of the strategic goals in the NIOSH Exposure Assessment Cross Sector and would also have indirect impact on the Emergency Preparedness and Response Cross Sector. In response to the NIOSH Research-to-Practice initiative, this project was to engage a private-sector business to build the prototypes and facilitate commercialization, and local stakeholders and NIOSH researchers to devise mock field-test scenarios responsive to various specific workplace exposure hazards.

The aims of the project (originally presented as "hypotheses") remained as follows:

Aim 1: A 1st-generation (Gen-1) PEMM can be constructed and the components, fluidic configuration, operating conditions and data management algorithms required for simultaneous quantitative determination of up to 10-15 VOCs of arbitrary composition, in complex mixtures, at relevant concentrations, in 10-15 min can be devised, optimized, and verified.

Aim 2: Guided by modeling, a set of redesigned 2nd-generation (Gen-2) micro-scale devices can be fabricated, integrated, and tested to provide higher sensitivity, chromatographic resolution, and speed with power dissipation commensurate with battery operation for >8 hr.

Aim 3: Construct three PEMM 2 field-ready prototypes with embedded microcontrollers and wireless interfaces that operate autonomously for >8 hrs on battery power.

Aim 4: Demonstrate through a series of well-controlled, mock-field tests that the PEMM is suitable for use as a personal direct-reading instrument for target contaminants in mixtures representative of exposures encountered by workers in several different industry sectors.

2.2 Significance

The lack of adequate exposure data has been consistently cited as the most critical factor limiting efforts to define exposure-response relationships in epidemiologic studies of systemic disease in worker populations.[1,2] This, in turn, impedes efforts to establish meaningful workplace exposure limits that rely on the accuracy of such relationships.[3-6] The assessment of personal exposures (and establishment of limits) in working environments with diverse sources of volatile organic compound (VOC) contaminants is a particularly difficult problem.[3,7] Attempts to correlate exposures to multiple VOC contaminants and health effects have been hampered, in large part, by a lack of cost-effective, analyte-specific monitoring capabilities; thus such correlations remain poorly understood.[2] In particular, for chronic VOC toxicants with short biological half-lives, the dose-rate dependence of health effects is often not known with certainty due to a lack of data on short-term excursions in exposures, and for all toxicants the influence of co-contaminants on the degree of hazard posed is similarly murky.[2-4] Emerging interest in the human exposome is spawning a new paradigm for biological monitoring that will need time-correlated air monitoring to identify specific contributors to proposed composite/summative biological and epigenetic indicators within the body,[8-9] creating additional demands for inexpensive, high-performance tools to characterize inhalation exposures to complex (VOC) mixtures.[10]

The need to quantitatively analyze personal exposures to specific VOCs spans numerous industry sectors defined by NIOSH, including manufacturing, agriculture/forestry/ fishing, construction, oil and gas extraction, health care, and public safety.[11] Generating new technology to meet this need would have direct implications for the strategic goal identified in the NIOSH Exposure Assessment Program to *"develop or improve specific methods and tools to assess worker exposures to critical occupational agents and stressors"* and the associated NIOSH direct-reading methods (DREAM) initiative.[12] VOC air concentrations of most concern in industrial workplaces are in the mid-parts-per-billion (ppb) to mid-parts-per-million (ppm) range; bracketing the occupational exposure standards/guidelines (TLVs, PELs, RELs).[13,14] Sorbent tubes or passive samplers are labor-intensive, require shipment to a lab for (expensive) analysis, and usually collect long-term samples (i.e., 8hr); exposure dynamics that may be relevant to health effects or work-practice modifications are missed. Performing measurements directly, on the worker, over short averaging times could improve the quality, quantity, and frequency of data gathered, reduce the cost per measurement, and permit timely feedback/interventions where necessary; particularly where rapid toxicokinetics or interactions with other mixture components may potentiate the hazard. Unfortunately, current field-portable VOC-monitoring instruments are too large/expensive for routine implementation for personal monitoring[15,16] or they lack capabilities for quantitative VOC *determinations* (i.e., identification/quantification) demanded by compliance monitoring or clinical or epidemiologic investigations.[17] *There are currently no wearable instruments capable of multi-VOC determinations.*

Research on miniature or micro-scale VOC-monitoring instrumentation containing microfabricated components has produced significant advances in recent years, addressing some of the shortcomings of current instrumentation.[18-33] Yet, the capability for rapid determinations of even moderately complex VOC mixtures has thus far eluded all but a few pioneering efforts. Arrays of microsensors based on several different transducer designs have

been developed for such applications, and are often referred to as electronic noses.[34,35] But it has become apparent that they can only differentiate up to three vapors from one another (via chemometrics) when presented to the array simultaneously.[36-41] Tao, et al. recently reported an array of polymer-coated quartz tuning forks in smart-phone-linked wearable packages with engineered selectivity for non-polar VOCs (and acidic gases). These clever systems are small and partially selective, but only provide a single composite (i.e., unspeciated) measure of all responding compounds in a class from a single sensor in the device.[30,32,33] Thus, while the attributes of microsensor arrays (small size, low power, crude response pattern, and low-cost via high-volume microfabrication) are compelling, they cannot serve as effective stand-alone analyzers that provide the multiple VOC-specific concentrations needed for compliance or epidemiology.

Reliable quantitative analysis of specific VOCs in complex mixtures generally demands temporal/spatial separation prior to measurement. Gas chromatography (GC) is the most effective approach to such separations, and GC microsystems (μGC) made from Si using microfabrication processing techniques[35] have enjoyed resurgent interest in recent years.[18-21,25,43-47] μGC is arguably the most promising technology for personal occupational VOC monitoring due to its versatility, small size, low cost, and potential for low-power battery operation. Although most of the scaling laws favor miniaturization of GC system components, due to the limited length (and minimum diam.) of separation columns employed in a μGC, it suffers an inherent constraint with regard to resolution and peak capacity, which limits the complexity of mixtures it can effectively analyze. This applies to all portable GC instruments using shorter (faster) columns.[48,49]

In response, efforts have been mounted to use microsensor arrays as μGC detectors.[18-21,45-47] The simple response pattern afforded by the detector constitutes a crude spectrum, which can assist in identifying eluting vapors and deconvoluting overlapping peaks (if needed), analogous to GC-mass spectrometer (GC-MS) systems, but much smaller, simpler, power-efficient. Thus, the inherent limitations of microsensor arrays and microcolumn separation modules can both be mitigated by their integration. Tao et al., (like others[51,68]) coupled their small sensors to conventional upstream GC columns; but only crude separations were achieved, they could not *identify* eluting peaks (retention time only), and units were not wearable.[31]

The PI has led one of the more prominent recent μGC research and development efforts through his role, since 2000, in the NSF-funded Michigan Center for Wireless Integrated Microsystems (WIMS).[50] Many of the issues requiring resolution to create effective μGC systems with detectors comprising microsensor arrays have been defined/resolved.[18,19,36-39,51-54] Our group developed the first lab-prototype μGC capable of *determining* VOC mixture components at ppb levels.[36,55,56] Since then, additional progress has been made in refining and developing new μGC components, and integrating them into working microsystems by the group at Michigan[57-63] and several other groups.[64-68] Some commercial efforts have emerged, as evidence of the viability of the technology and the promise of practical application.[69-72]

For personal monitoring, several design innovations are required, including a reduction in size, weight, and power dissipation (to permit battery operation), on-board control and data logging, and wireless interfacing. Since allowable concentrations in workplaces are generally in the mid-ppb to mid-ppm range, the air volume required in order to reach the detection limits (LOD) of the downstream sensor array is only a few mL and the sampling time can be reduced to < 5 min.

The research proposed here focused on streamlining, redesigning, miniaturizing, and drastically reducing the power dissipation of the μGC system in order to realize a belt-mounted configuration that operates for 8 hr and collects 6-10 samples/hr. It also focused on maximizing the number of VOCs analyzed in a single sample. The project succeeded in demonstrating that this μGC technology can fill the need for small, inexpensive, wearable, turn-key instrumentation

capable of direct, autonomous identification/quantification of VOCs in complex workplace-air mixtures with high temporal resolution. In regard to the NIOSH r2p initiative, we have included on our team a small start-up company to lead the Gen-2 construction effort and look to commercialize the technology. We also engaged NIOSH researchers to guide us in the selection of target analytes we used for the mock field tests so as to be responsive to their views on ultimate application.

2.3 Summary of Project Scope, History, and Completion

Aim 1. Construct a Gen-1 PEMM prototype and obtain baseline data. Optimize/verify components, configuration, conditions, data management for determinations of 10-15 VOCs every 10-15 min.

Phase 1. (100% complete)

Milestone 1.1. Assemble Gen-1 PEMM; show baseline performance (100% compl. revised)
Milestone 1.2. Optimize separation conditions/decide on carrier gas (100% compl.)
Milestone 1.3. Determine desorption efficiency/bandwidth from μsampler (100% compl.)
Milestone 1.4. Establish transfer efficiency from μsampler to μfocuser (not needed)
Milestone 1.5. Establish breakthrough capacity of μsampler (100% compl.)
Milestone 1.6. Develop pre-trap for low-volatility interferences (100% compl.)
Milestone 1.7. Apply chemometric algorithms to response data (100% compl.)
Milestone 1.8. Assemble Gen-1 PEMM; show comprehensive performance* (100% compl.)
* this was a (major) new Milestone added in Year 1

Aim 2. Design, fabricate, integrate, and test new micro-scale devices for Gen-2 PEMM for higher sensitivity, chromatographic resolution, speed with low enough power for battery operation for >8 hr.

Phase 2. (100% complete)

Milestone 2.1. Modeling and fabrication of new micro-scale components (100% compl.)
Milestone 2.2. Characterization of Gen-2 devices & subsystems (100% compl.)

Aim 3. Construct 3 Gen-2 PEMM field-ready prototypes with embedded microcontrollers and wireless interfaces capable of operating continuously/autonomously for >8 hrs on battery power.

Phase 3. (97% complete)

Milestone 3.1. Detailed design and planning of Gen-2 PEMM (100% compl.)
Milestone 3.2. Microcontroller programming and implementation (100% compl.)
Milestone 3.3. Modified interface circuitry; microcontroller integration (100% compl.)
Milestone 3.4. Assemble first Gen-2 PEMM prototype; test (100% compl.)
Milestone 3.5. Demonstrate/verify performance of first Gen-2 prototype (100% compl.)
Milestone 3.6. Construct two additional prototypes; calibrate, compare* (80% compl.)

*3 prototypes were built and each was revised once. Testing to date has been confined primarily to the first and second PEMM 2 prototypes, hence the 80% completion assignment

Aim 4. Demonstrate via mock-field tests that the Gen-2 PEMM can serve as a personal direct-reading instrument for target contaminants in mixtures representative of worker exposures.

Phase 4: (mos 25-36) (90% complete)

Milestone 4.1. Construction of test chamber (100% compl.)

Milestone 4.2. Test atmosphere generation system (100% compl.)
Milestone 4.3. Perform mock-field testing * (60% compl.)
Milestone 4.4. Preparation of final report (100% compl.)
* some mock field testing was performed, but less than proposed. Work is on-going.

2.3.1 Progress/Completion

Excellent progress was made toward the goals of this project. There were 4 Specific Aims, several Milestones within each Aim, and several Tasks within each Milestone. As summarized above, and described in detail in the following pages, the project proceeded relatively few modifications, though with several delays. In the end, we completed 100% of the Milestones within Aims 1 and 2, and we completed 100% of all but one Milestone in each of Aims 3 and 4.

2.3.2 History and Changes

As described in our Year-1 progress report, the decision by NIOSH to fund this grant came in mid-September, 2013, with very little advanced notice, and the grant was back-dated to an official start date of September 1st, 2013. With the abruptness of the funding decision, it took us approximately 2 months to hire personnel to start on the project, get the internal funding dispersed to our UM collaborator, and initiate work on Milestones 1, 2, and 3. In addition, our original commercialization partner, 3DS/APIX, had to back out of the project due to uncertainties in their core funding. As a result, we had to secure an alternate commercialization partner, VGC Chromatography, which was originally to play a supporting role to 3DS/APIX, but which took over all tasks originally assigned to 3DS/APIX. VGC came on-board in January, 2014. They have been good partners, though toward the end of the project could not deliver work in a timely manner and they have yet to return the 3rd prototype with revised hardware and software suitable for field deployment. This was not a serious constraint because we have the other two prototypes, and delays on our end have been more of a hindrance than delays on their end.

In the wake of this, we made some changes to Milestone 1.1, replacing it (and many of its constituent Tasks) with a new Milestone (1.8), as part of Aim 1/Phase 1. We also initiated some of the work on Phase 3 that was originally assigned to the commercialization partner, to reduce delays in getting the prototype planning/development effort underway. Thus, as of the Year 1 progress report (March, 2014), we were about 2 months behind schedule on certain tasks, but we had completed or advanced a few others ahead of schedule. We made every effort to make up for this over the ensuing 5 months to meet our Year 1 Milestones, but were only partially successful. That is, we were still about 2 months behind schedule in meeting our Year 2 Milestones by the end of year 2 (September, 2016).

We then suffered a change of personnel – the lead student working on the project defended his dissertation and left the group to take a job. His replacement student took a significant amount of time to come up to speed, even with the help of a post-doc hired to help with microcolumn characterization and initial mock field testing. Tasks listed under Milestone 1.1 were partially completed during Year 1, but then the same or similar tasks were shifted to Milestone 1.8 to be completed using the Gen 1 PEMM prototype components, subsystems, and full system (in lieu of the originally proposed test bed). The construction of the revised PEMM 1 prototype took longer than expected, but we eventually created a fully operational instrument. Problems with our sensor array fabrication (poor metallization) led to a 6-month delay in final tests of the Gen 1 PEMM prototype.

At about this time, our collaborator, Prof. Kurabayashi, resigned from the study, which left the modeling and characterization of the microcolumn to us to do on our own. We are indebted to Prof. Kurabayashi and his group (Mr. Buggaveeti and Dr. Nidetz) for extensive initial modeling and for fabricating the Gen-2 µPCF devices and monolithic 6-m µcolumns, which

allowed us to complete Aim 2 (and to use the devices to complete Aim 3). Unfortunately, their initial modeling was rendered unusable by their use of Al as the heater metal, which turned out to be a major error (Si and Al interdiffuse at elevated temperature, leading to failure of the heaters). We/they replaced the heaters with Pt but the modeling based on Al was not applicable and modeling with Pt was limited to constant-voltage scenarios and to a device smaller than the final device that were not applicable to the actual heating profiles used in the devices. Luckily, our electronics technician was able to perform the modeling and assist our post-doc with the characterization of the microcolumns, to salvage the effort. Aim 2 was thus completed and the results submitted for publication in September, 2016.

Aim 3 was delayed because of delays in fabrication of the microcolumns and problems with the fabrication of chemiresistors. In addition, the subcontractor's approach to onboard battery power proved infeasible in the end, requiring us to devise an alternate plan, employing external battery packs. We had hoped to avoid the need for a Raspberry Pi device, but in the end had to use it because of limitations of the PIC32 and ARM on-board microcontrollers. The sub-contractor eventually succeeded in creating working prototypes, but the first versions were difficult to program. Thus, a revision to the electronic hardware and firmware was necessary to achieve optimal performance for all three prototypes. All told, the delays set the project back by 1 year. We were able to operate and generate data from one of the earlier prototype versions, but received 2 of 3 of the revised working prototypes by April, 2017. The sub-contractor retained one of the prototypes to use as an exemplar for seeking first- adopter partners for commercialization.

Aim 4 entailed calibrations of the PEMM 2 prototype(s) and some "preparative" mock-field testing conducted by members of the research team in preparation for such testing with volunteers, per the original proposal. At this point, we lost another member of the team, and had to deal with competing projects, so progress was further impeded. Although we succeeded in demonstrating the prototype with a limited set of mixtures and exposure scenarios, and it performed extremely well(!), we did not complete the scope of such testing originally planned. Thus, we continue to pursue more extensive testing in this post-award period.

2.4 Phase 1/Aim 1

2.4.1. Introduction to Phase 1/Aim 1

Phase 1 addressed **Aim 1**, which was to entail construction of an initial, single PEMM laboratory prototype using existing microscale devices with a goal of packaging the system within a 4×8×10" chassis. Microsampler capacity and transfer efficiency were to be determined. The choice of on-board He-cartridge carrier gas vs. scrubbed ambient air was to be assessed and decided. Operating conditions and data management algorithms required for the capture, transfer, separation, and array detection of targeted VOC mixtures at relevant concentrations were to be adapted from the SPIRON prototype (note: SPIRON was a predecessor technology). Interference rejection was also to be tested. Chemometric algorithms were to be further developed. AC power and laptop control were to be used. This Gen-1 prototype was to be calibrated in the lab using test atmospheres of VOCs in mixtures at different temperatures and humidities. The components, configurations, and operating conditions required for the quantitative determination of 10-15 VOCs in < 10 min were to be established.

One significant change made to this Phase/Aim was that we decided to alter the Gen-1 PEMM system configuration so as to retain its suitability for generating baseline data, as originally intended, but to create a Gen-1 PEMM prototype that improved on the proposed Gen-1 PEMM and allowed us to test some of the innovations we were planning to incorporate into the ultimate Gen-2 prototype. This change altered our path significantly and resulted in a shift of most of the tasks originally directed toward Milestone 1.1 to a newly created Milestone 1.8. In effect, Milestone 1.8 replaced Milestone 1.1 and represented the culmination of work done to meet Milestones 1.2-1.7. This was very successful and led to a very effective prototype that was characterized to a greater extent than any other µGC prototype ever reported.

Below, we describe the salient results of work resulting in the achievement of Milestones 1.2-1.8. The order of presentation deviates from the numerical order of the Milestones because it provides a more logical flow. That is, following some introductory comments, we discuss the development and characterization of the pre-trap (Milestone 1.6) because it is at the inlet to the system. We then present the characterization of the PEMM 1 microcolumns (Milestone 1.2) because their operating conditions constrain those used for the µPCF. We then discuss the development and characterization of the capacity and desorption efficiency of the µPCF (Milestones 1.3 and 1.5) because it is the second device in the sample flow path and we devoted considerable time and effort to its characterization. Milestone 1.4 was not met because it was found during preliminary testing that the downstream focuser device did not improve injection bandwidths as compared to the µPCF itself. Work on chemometric analyses (Milestone 1.7) was abbreviated and was folded in to the presentation of the assembly and characterization of the fully assemble PEMM 1 prototype (Milestone 1.8).

Some of the results relevant to this Aim were presented in the Year-2 (Summative) Progress Report submitted in March, 2015. A subset of those have been reiterated here where it made sense to do so. Most of the results summarized here have also been presented in the following two peer-reviewed publications, and the reader is invited to read those for additional details, particularly about methodology, which will not be covered in as much detail here:

Z1. Wang J, Bryant-Genevier J, Nuñovero N, Zhang C, Kraay B, Zhan C, Scholten K, Nidetz R, Buggaveeti S, Zellers ET: [2018] Compact Prototype Microfabricated Gas Chromatographic Analyzer for VOC Mixtures at Typical Workplace Concentrations. Microsystems and Nanoengineering 4: 17101.

Z2. Bryant-Genevier J, Zellers ET: [2015] Toward a Microfabricated Preconcentrator-Focuser for a Wearable Micro-scale Gas Chromatograph. Journal of Chromatography A 422: 299-309.

Figure 1.1 shows a block diagram of the fluidic and analytical components of the PEMM 1 prototype and Figure 1.2 shows the microdevices and fully assembled prototype. It is designed and operated to perform generalized VOC measurements in industrial workplaces, with a capability for quantitatively analyzing up to ~20 VOCs per measurement at a rate of ~6-8 measurements per hour. For practical reasons, we focused on VOCs falling within a moderate volatility window defined by their vapor pressures, p_v. For quantification, it was assumed that concentrations would fall in the high parts-per-billion (ppb) to high ppm range, which is the most relevant range for workplace exposure monitoring. Following the presentation of component-level test results intended to confirm critical performance capabilities, we present a comprehensive series of system-level test results intended to demonstrate reliable mixture-component determinations and autonomous operation. The implications of the results for the design and operation of the PEMM-2 prototype are then assessed.

2.4.2. System Design and Operation Specifications

By design, air samples are drawn by the mini-pump through the inlet, and low volatility interfering VOCs are retained by the wall-coated-capillary pre-trap (Figure 1). The air sample then passes through the μPCF, where target VOCs are quantitatively captured in one of the two adsorbent beds. After turning off the pump and switching the valves to start the flow of He through the microsystem, the μPCF is rapidly heated to thermally desorb the captured VOCs for passage to the μcolumns in a narrow band. Temperature-programmed separation of the VOC mixture components is performed, with detection provided by the transient changes in the resistance of the MPN-coated μCRs in the array as VOCs reversibly sorb into the MPN films to different extents, giving rise to a response pattern. The flow is then redirected to backflush the pre-trap and the fore-line to purge any residual VOCs, and the μcolumns are allowed to cool in preparation for the next cycle.

Several performance criteria were used to rationalize the design, integration, and operation of the instrument components.[39] The primary constraint placed on the target VOCs was that they fall within a p_v range of ~0.03 to 13 kPa. Less volatile compounds would tend to adhere to surfaces in the (unheated) fluidic pathways, and more volatile compounds would be difficult to trap, separate, and detect because these functions rely on partitioning phenomena. Where possible, target VOCs were chosen that also had assigned Threshold Limit Values (TLV®),[56] which serve as reference values for specifying the ranges of concentrations to be encountered. To assess the selectivity of the pre-trap and μPCF, we included several potentially interfering compounds outside of the designated p_v range. For the target VOCs, a set of 17 common workplace VOCs was selected with the understanding that actual workplace exposures might involve greater or fewer VOCs in practice. Table 1 lists the set of 24 target and interfering VOCs selected, together with p_v values and assigned TLVs.

Results from previous studies were considered in the selection of the μPCF adsorbents, the μcolumn length and stationary phase, the number of sensors and nature of MPN coatings for the μCR array, and the 5- and 10-mL air sample volumes used at the outset. For the latter, we assumed a working limit of detection (LOD) of ~5 ng for the μCR sensors. A 40-fold concentration range limit was imposed, indexed to the TLV Time-Weighted Average (TLV-TWA, 8-hr average) for each VOC. That is, it was assumed that 0.1×TLV was a suitable LOD-level concentration to measure and that 4×TLV was a suitable maximum quantification limit for any given measurement. Several target compounds also have an assigned Short-Term Exposure Limit TLV (i.e., TLV-STEL), which is a 15-min average limit set to protect against acute health effects, and is usually within 4× the TLV-TWA. The challenge of specifying a fixed sample volume for mixtures of VOCs with widely different TLV values is discussed in ref. Z1.

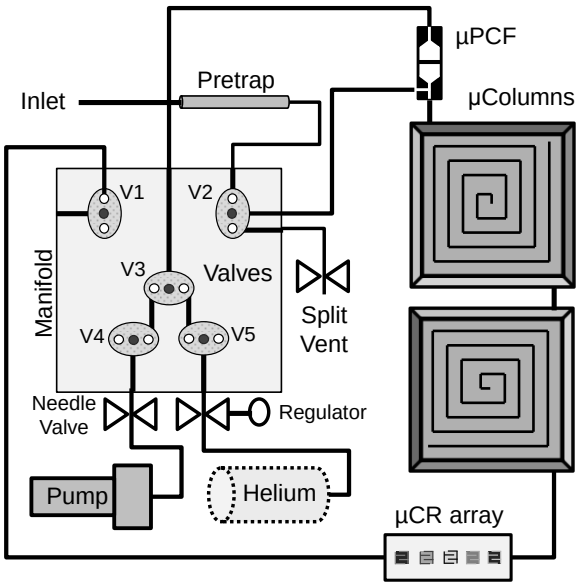

Figure 1.1. Layout diagram of fluidic and analytical components of the PEMM-1 prototype µGC.

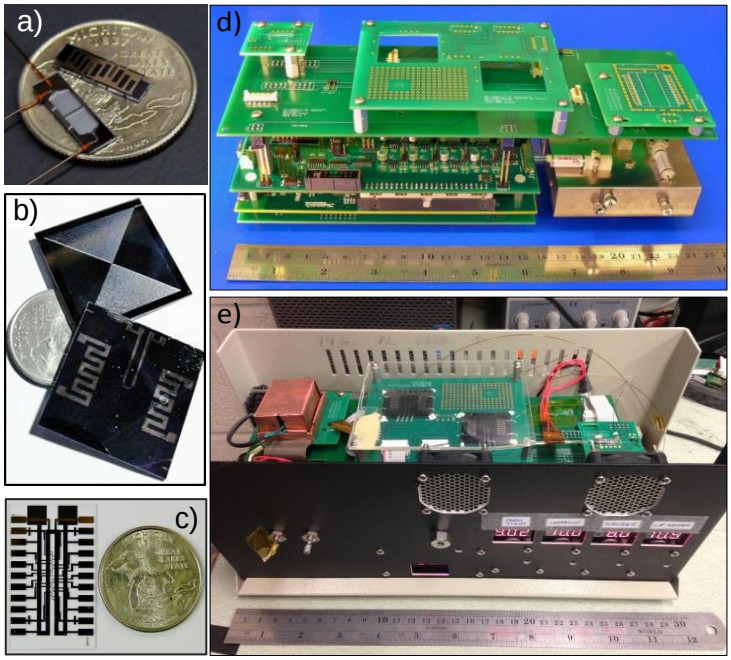

Figure 1.2. Photographs of a) the front and back side of an unloaded µPCF fitted with capillaries (U.S. quarter for scale); b) the front and back side of a µcolumn (U.S. quarter for scale); c) the µCR array with backside heater and RTD (U.S. quarter for scale); d) assembled PCBs (sans fluidic components) and valve manifold; and e) the fully assembled PEMM-1 prototype with lid removed.

2.4.3. Pre-trap

Two configurations of pre-traps for precluding low-volatility interferences from entering the system were explored. The first, referred to as pre-trap A, consisted of a thin-walled stainless-steel tube (1.58 mm i.d.) packed with up to 5.4 mg of either Carbopack C (C-C, 10 m^2/g) or Carbopack F (C-F, 5 m^2/g) (both 60/80 mesh) and retained with glass wool. The second consisted of short sections cut from commercial capillary columns, 250 μm or 530 μm i.d., with stationary phases of PDMS (Rtx-1; pre-trap B1) or polymethylphenylsiloxane (Rtx-20; 80:20 methyl:phenyl; pre-trap B2), respectively (Restek, Bellefonte, PA). The effects of several relevant variables on the breakthrough volumes of representative test compounds were evaluated.

Our working goal was to pre-trap compounds with p_v values similar to or lower than that of n-tridecane (C_{13}, p_v = 0.0075 kPa) while allowing compounds with p_v values similar to or greater than that of C_{12} (p_v = 0.027 kPa) to pass through with negligible retention. Compounds of intermediate volatility would be partially retained, as a practical concession. Additionally, the pre-trap had to be regenerable via backflushing without heating.

Devices were challenged with test atmospheres of one or more VOCs in N_2-filled sampling bags, which were placed in a sealed drum and pressurized to push the atmosphere through the pre-trap at a known rate. A bench scale GC (Agilent 6890, Agilent Technol., Palo Alto, CA) was used downstream to monitor the VOC concentrations directly or via a sampling loop that was periodically injected. Either a short segment of uncoated, deactivated capillary or a short PDMS-coated separation column was used between the GC inlet port and the FID.

Initial tests used packed-tubes containing 5.4 mg of either C-F or C-C (i.e., pre-trap A) and entailed individual challenges with n-alkanes C_{11} to C_{13} at ~200 ppm. Both adsorbents showed significant fractional retention of C_{11} from 10 mL sample volumes and, while the C-F provided a 10% breakthrough volume of ~25 mL for C_{13}, it required heating with backflushing for regeneration. Additional experiments with different bed masses and at different temperatures and concentrations failed to arrive at a viable arrangement with these granular adsorbents. We also tried glass beads, but these did not show sufficient retention of C_{13}.

We then explored capillary-column pre-traps B1 and B2, again using C_{11} and C_{13} as our primary test vapors. With pre-trap B1, the breakthrough volumes of both analytes were independent of flow rate, from 4 to 11 mL/min, and concentration, from ~0.4 to ~2 ppm, and linearly dependent on the length of the pre-trap, from 4 to 10 cm. Increasing the pre-trap temperature from 20 to 25 °C resulted in a 10% decrease in the 10% breakthrough volume for C_{13}. Both pre-traps B1 and B2 showed similar retention behavior. Pre-trap B2, however, showed slightly better discrimination between C_{11} and C_{13} based on the ratio of 90% and 10% breakthrough volumes, respectively (Figure 1.3). For mixtures of compounds with p_v values similar to that of C_{11}, the presence of additional compounds did not decrease the breakthrough volume relative to that of any single compound for either pre-trap (Figure 1.4). Regarding regeneration, after passing 10 mL of a 3 ppm sample of C_{13} through pre-trap B2 and reversing the fluidic connections to allow monitoring with a downstream FID while backflushing at ambient temperature, it required 20 mL before the FID had returned to baseline (Figure 1.5). As discussed below, we ended up using pre-trap B1 in the final testing of PEMM 1 in this study. Additional results relevant to the pre-trap were collected with the fully assembled PEMM 1 prototypes, as described below.

All the experiments described above were done using representative compounds. In order to assess how the pre-trap functioned with compounds relevant to industrial workplace air monitoring a number of compounds of similar vapor pressure were selected and the breakthrough was determined (Figure 1.3a). One important function of the pre-trap is that breakthrough is independent on the number of different vapors present in the test atmosphere. As shown in Figure 1.3b it is seen that the breakthrough curves of a mixture can be represented

from a linear combination of the individual breakthrough curves of the mixture's components. In this way it is demonstrated that test atmosphere composition has no impact on breakthrough volumes.

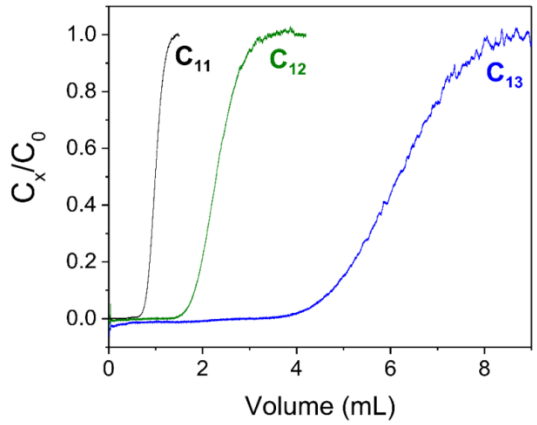

Figure 1.3. Fractional breakthrough of C_{11}, C_{12}, and C_{13} vapors (individual exposures at ~ 100 ppm each) as a function of sample volume (5 mL/min) for pre-trap B2 (consisting of 6.5 cm long segment of 250 µm i.d. capillary with a 0.1 µm thick wall coating of Rtx-20). Note that the 10% breakthrough volume for C_{13} was ~5 mL while the 90% breakthrough volume for C_{11} was 1.2 mL.

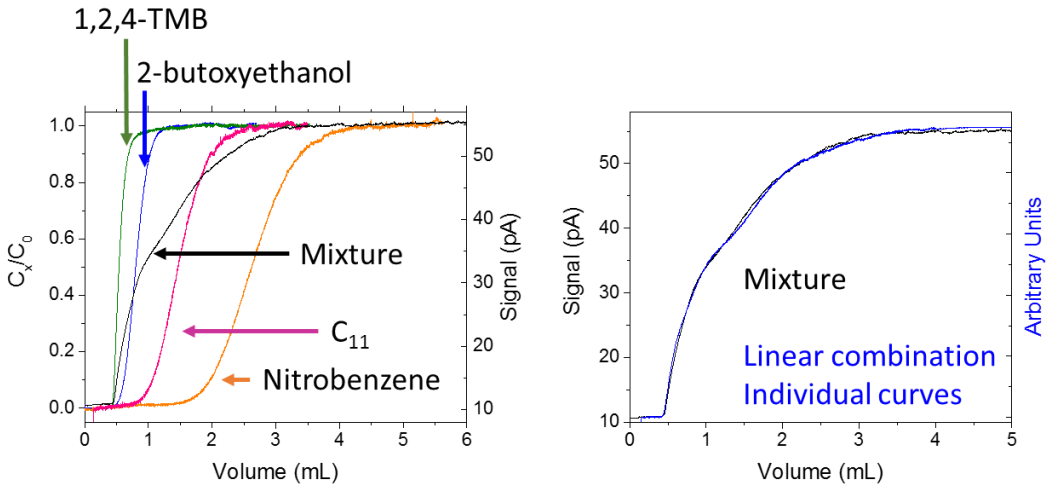

Figure 1.4. (a) Breakthrough of target compounds (colored curves) through pre-trap and breakthrough of a mixture containing all individual compounds (black curve). (b) Comparison of experimental mixture breakthrough (black curve) with theoretical breakthrough (blue curve) which was constructed from a linear combination of individual breakthrough curves from Fig. 1.4a.

The defining feature of the pre-trap characterized here is the ability to regenerate the trap to its initial state after sampling. In experiments to regenerate the pre-trap vapor, 10 mL of air was passed through the pre-trap followed by backflushing with purge gas. Downstream FID was used to monitor concentration at all times. As shown in Figure 1.5 for a sample volume of 10 mL it is necessary to backflush for 20 mL before the FID has returned to baseline.

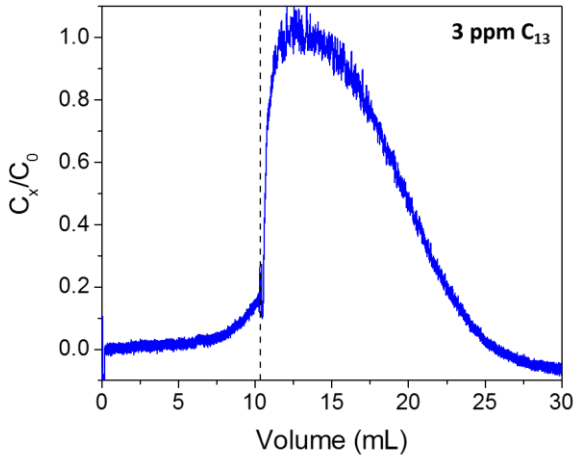

Figure 1.5. Fractional breakthrough vs. breakthrough volume for C_{13} showing 10 mL sampling followed by 20 mL of backflush using N_2 purge gas.

In summary, breakthrough volume varied linearly with pre-trap length at a fixed flow rate. There was no effect of flow rate on breakthrough volume. Thinner, less polar stationary phases showed better discrimination between high vapor pressure target compounds and low vapor pressure interferences. Breakthrough volumes were unaffected by test atmosphere composition for tests with multiple analytes present. For pre-trap regeneration, a 20 mL backflush was necessary to completely purge the pre-trap to its initial state given a 10 mL sample volume. Based on the characteristics of the pre-traps described above it was decided to use a pre-trap consisting of 6.5 cm long segment of 250 µm i.d. capillary with a 0.1 mm thick PDMS stationary phase. Using this length leads to 10% breakthrough of C_{13} at about 5 mL, which is not ideal, but the 90% breakthrough volume for C_{11} is only 1.2 mL which is a low enough fraction of the anticipated 10 mL sample to minimize losses (i.e. retention) of the less volatile compounds in the pre-trap (Figure 1.3). The breakthrough volume of C_{12} was ~2.6 mL. For a sample of 5-10 mL, this pre-trap was considered to offer an acceptable tradeoff in performance. Backflushing/cleaning of the pre-trap required ~2× the sample volume. This solution was not perfect, but it would suffice.

2.4.4 µColumns

Since the flow rates used to inject samples from the µPCF are constrained by the fact that they impact the chromatographic efficiency of the microcolumns, it is appropriate to discuss the device-level testing of the microcolumns before discussing the µPCF.

Each of the two µcolumn chips (Figure 1.2b; 3.1×3.1 cm) contains a single DRIE channel (240 µm (h)×150 µm (w); 3.1 m long) that spirals in to the center and back out to the edge of the chip in a square pattern with chamfered corners. A 500 µm thick Pyrex cap was anodically bonded to the top face to seal the fluidic channel at wafer scale. A pair of heaters and an RTD were patterned from Ti/Pt onto the backside. Deactivated capillaries (250 µm i.d.) inserted into the inlet and outlet ports of each µcolumn were sealed with Duraseal.

A previously described static method was used to deposit and crosslink the PDMS stationary phase on the inner walls of the channels to a nominal thickness of 0.20 µm.[14,40] After coating, the inlet and outlet capillaries were replaced with fresh uncoated (deactivated) capillaries sealed to the chip with Hysol. The capillaries emanating from the outlet of the first µcolumn and the inlet of the second µcolumn were cut to ~5 mm, inserted into opposite ends of a short (i.e., ~1.2 cm) Pyrex/Si conduit interconnect with a Ti/Pt meander-line heater patterned

on the Pyrex, and sealed (Hysol). The assembly was inverted, affixed with Hysol to a custom PCB with rectangular cutouts below the μcolumns, and wire-bonded.

Although, the microcolumns used in the PEMM 1 prototype have been used before, we re-tested their chromatographic efficiency. The Golay plot using N_2 as carrier gas shown in Figure 1.6 permits an evaluation of the number of theoretical plates per meter of length, and shows that the minimum plate height is 0.025 cm, and that the total plate count is 4,000 plates/meter. This is comparable to what we found in our initial tests of these microcolumns, and indicates the columns are in good shape.

The optimal velocity (curve minimum) corresponds to a flow rate of 0.2 mL/min, which is quite low. The plot only goes out to about 1 mL/min (45 cm/s), but these curves are ~linear past ~15 cm/s, so extrapolating out to 3 mL/min (135 cm/s) would yield about 623 plates/m. 3 mL/min is currently the default flow rate for reasons explained below, related to microsampler desorption performance. This reduction in plate count was expected. Using He as carrier gas leads to higher plate counts at higher flow rates (see below), and argues for using He to the extent that this performance criterion dictates the decision.

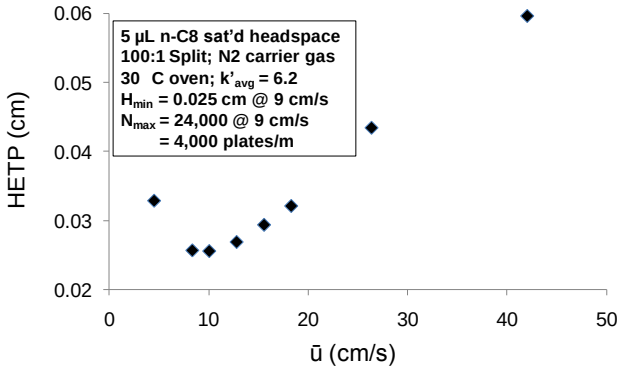

Figure 1.6. Golay plot for 6-m PEMM 1 microcolumn ensemble using air as carrier gas.

Over the course of the project we had new 3-m microcolumn devices made and we have coated several of them with PDMS for the purposes of performing band trajectory modeling (to be ultimately applied to the Gen-2 microcolumns) and to have a fresh set for the PEMM 1 prototype testing. These columns were mounted and wire-bonded to carrier printed-circuit boards, and tested for efficiency as described above and yielded efficiencies (plate counts) similar to those of the previously tested microcolumns.

Shown below in Figure 1.7 is another Golay plot for a representative additional 3-m microcolumn coated with PDMS and eventually crosslinked in-situ. The maximum number of plates (N_{max}) for the μcolumn was 4200 plates/m at an optimum velocity ($\bar{u}_{opt}$) of 10 cm/s which was typically of the μcolumns produced for this project. Post-crosslinking reduced the N_{max}, though never by more than 5%. This column and others like it were used in conjunction with other devices to complete tasks in other Milestones throughout this report.

As an initial test of microcolumn performance with the sensor array detector installed, we performed a simple separation using a conventional bench scale GC inlet with sample loop injection. Figure *1.8a* shows a 6 component mixture separation using a new (Gen-2) CR array for detection and 2 3-m-long PDMS coated μcolumns for separation. This array was coated only with C8 and OPH MPNs (C8 and OPH are acronyms for two of the nanoparticle materials used as sensor coatings, defined in Section 2.4.6); 5 sensors each (out of 10 in the new arrays). Data are for C8 sensor in position 2 and OPH sensor in position 8. The columns were mounted

inside a GC oven at 30 °C. The GC also provided the carrier gas (1.5 mL/min He) and injection (6-port gas sampling valve).

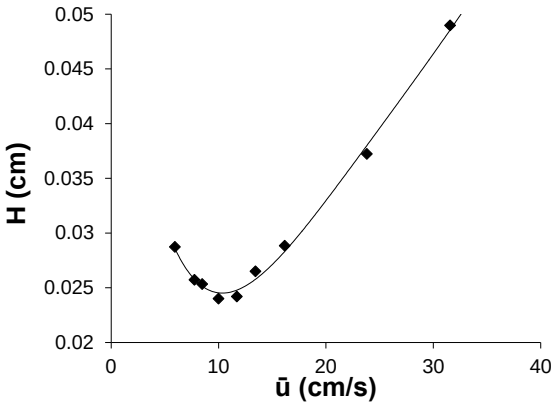

Figure 1.7. A Golay plot typical of those obtained during µcolumn coating quality control. Conditions: n-octane probe; 5 µL static headspace injection; 1000:1 split ratio; N_2 carrier gas; 30 °C GC oven; 3 m PDMS (0.2 µm thick) µcolumn; FID. This Golay plot was obtained after coating but before stationary phase cross-linking.

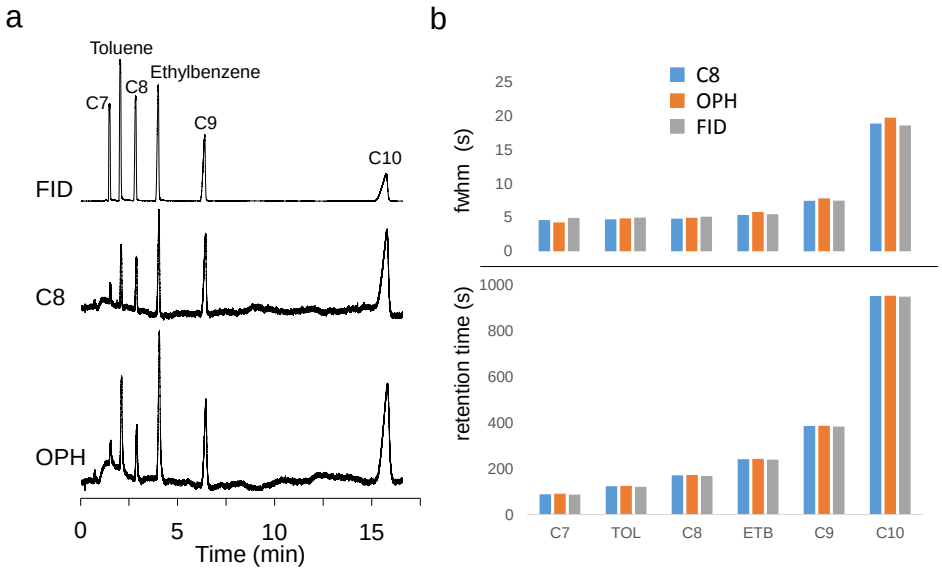

Figure 1.8. a) 6 component mixture separation using 2 3-m-long µcolumns for separation. The FID trace (top) was obtained as a separate run for comparison, with the flow rate adjusted to match n-heptane retention times. The C8 (middle) and OPH (bottom) traces were obtained from the 2nd and 8th channels respectively of the same CR array. b) Bar charts of fwhm values (top) and retention time values (bottom). Conditions: ~100 ng injection from a static test atmosphere; 1.5 mL/min He carrier gas; 30 °C GC oven.

Values of full-width at half maximum (*fwhm*) and retention time are shown in Figure *1.8b.* The same experiment was repeated at 2 mL/min and 3 mL/min flow rate with similar results (data not shown). Differences in analyte retention times between the FID and either CR sensor were <1.5% at 1.5 mL/min, <2.2% at 2 mL/min and <3.4% at 3 mL/min. The smallest difference

was 0.2% for n-decane at 1.5 mL/min. Differences in the values of *fwhm* between the FID and either CR sensor were <10% for all flow rates and analytes.

Despite being performed at a very low column temperature (and, thus, over a long period of total separation time), these are excellent results as they show that the columns perform well in separating compounds and maintaining sharp peaks, and that the sensors can provide responses comparable in time and shape (though now sensitivity) to those from an FID.

2.4.4.1 Carrier Gas. Given the availability of small, inexpensive He canisters and regulators (8"×2") with sufficient capacity for numerous analyses at anticipated low flow rates and separation cycles, the tradeoffs between scrubbed ambient air vs. He carrier gases need to considered. Separation theory and empirical evidence suggest that He allows higher flow rates to be used without significant loss of chromatographic efficiency. This affords more rapid analyses for a given mixture or more complex mixture separations in a given time. Use of inert He also reduces degradation of the stationary phase at high temperature. Although we have documented that the use of scrubbed ambient air as carrier gas is not a critical problem with the polydimethylsiloxane (PDMS) phase, He may improve long-term stability, and allow for eventual use of more polar stationary phases that degrade more rapidly in air at high temperature. Use of He would eliminate the scrubber and reduce power dissipation by eliminating one valve and reducing pumping time. In addition to its superior chromatographic performance relative to scrubbed ambient air at typical operating flow rates, the 2.4 g of He in each canister is projected to allow 228 analyses, corresponding to 30 hr of continuous operation at 8 min (and 63 mL of He) per cycle.

For tests of the separation efficiency as a function of carrier gas, the dual μcolumn ensemble was installed in the oven of the bench scale GC-FID and connected between the inlet and FID via press-tight unions. Analytes were introduced by autosampler syringe or by sample loop connected to a 6-port valve (Model AC6WE, Vici Valco, Houston TX) mounted to the GC. The FID was calibrated with analytes diluted in CS_2.

Injections of a vapor-phase mixture of methane and n-octane were made at each of several flow rates in both N_2 and He carrier gases at 30°C. Plate height, *H*, determined by standard methods, was plotted against flow rate as shown in the Golay plots in Figure 1.9 for both carrier gases. Results yielded optimal average volumetric flow rates of 0.17 and 0.56 mL/min for N_2 and He, respectively (Figure 1.9) and a maximum plate count N of ~4,300 plates/m. At our anticipated operating flow rate of 3 mL/min (i.e., >> the optimal flow rate), the values of N were 150 and 570 plates/m for N_2 and He, respectively, which highlights the improvement observed when switching to helium (vs. air or N2). Chromatographic performance near the respective Golay minima is almost identical for both gases (similar minimum plate heights), however at the higher flow rate of 3 mL/min needed for the system to provide sharp injection pulses (see below) and sharp sensor peaks (see below), chromatographic efficiency is much greater for helium. This argued for including helium in the PEMM 1 and PEMM 2 designs.

2.4.4.2 μColumn Capacity. Tests of the μcolumn capacity indicated that the *fwhm* values of the peaks from several test compounds started to increase significantly and resolution started to degrade significantly at injected masses > 8 μg (see Figure 1.10). For an air sample of 10 mL, 8 μg corresponds to an air concentration of 800 mg/m^3, which is > 2×TLV for most, but not all, compounds with assigned TLVs (see Table 1.1 below). For reference, toluene has a TLV of 20 ppm, or 75 mg/m^3, whereas heptane has a TLV of 400 ppm, or 1600 mg/m^3. Thus, the capacity of the μcolumns, while sufficient for the vast majority of VOCs of interest, might be exceeded for VOCs with high TLVs at concentrations > TLV, with a resulting slight decrease in chromatographic resolution. In such cases, a modest injection split could be used.

Of course, temperature is an important cofactor: higher temperatures reduce the retention factors of all analytes and, thus, the dependence of the *fwhm* on mass injected, because sorption equilibria are shifted in favor of the mobile phase. With temperature programmed separations, the influence of this factor would vary; lighter VOCs would probably elute completely before the μcolumns reached 50°C, increasing the chances of overloading, whereas heavier VOCs would likely elute at > 50°C, reducing the ultimate impact of this factor on the *fwhm*. These data provide some confidence that injections smaller than ~8 μg of any single component would not result in significant reductions in chromatographic performance due to overloading of the stationary phase in most exposure scenarios.

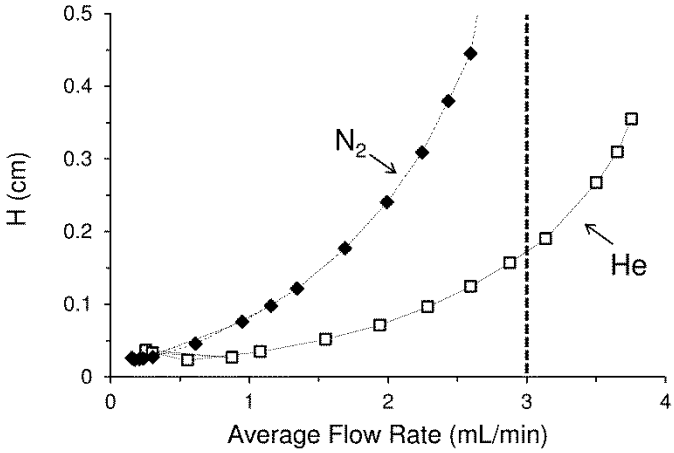

Figure 1.9. Golay plot for the dual 3-m μcolumns to be used in PEMM 1 generated from a mixture of methane (for hold-up time) and n-octane in N_2 and He carrier gases as indicated. Gas-tight syringe injections and FID detection were used. The maximum plate count, N, was ~4,300 plates/m with N_2 or He at optimal flow rates of 0.17 and 0.56 mL/min, respectively. The vertical dashed line highlights the difference in H values at 3 mL/min, which was the analytical-path flow rate used for most testing. The much lower value of H for helium than for nitrogen, strongly argues for He as carrier gas.

To characterize the improvement in performance for the proposed application, further testing was conducted. A hypothetical exposure scenario mixture was analyzed using the columns, first with He as carrier gas, and then with nitrogen (similar to air chromatographically). The results of these tests are shown in Figure 1.11. Both the degree of overlap among peaks in the mixture as well as the number of co-elutions increased when nitrogen was used as carrier gas, as expected. It was concluded that despite the increased size and weight associated with using helium as carrier gas (regulator and pressurized miniature canister), it would be beneficial in light of the chromatographic improvements.

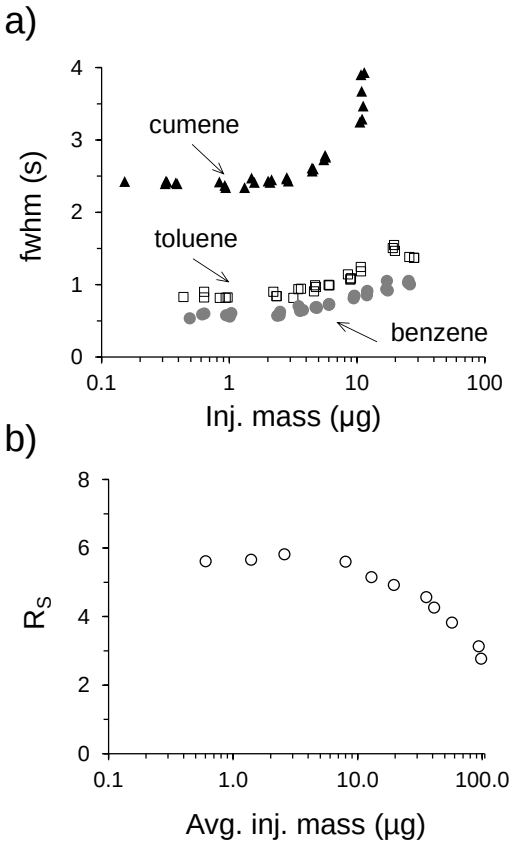

Figure 1.10. Effect of injected mass on chromatographic resolution for the µcolumn ensemble (6 m total length); a) effect of mass on fwhm for three target vapors, benzene, toluene and cumene, and b) effect of injected mass on chromatographic resolution of benzene and trichloroethylene. Mass in b) is the average mass of trichloroethylene and benzene in the injection, and the binary mixture was in a 1.5:1 ratio, respectively, to account for differences in FID sensitivity (i.e., to maintain similar peak sizes).

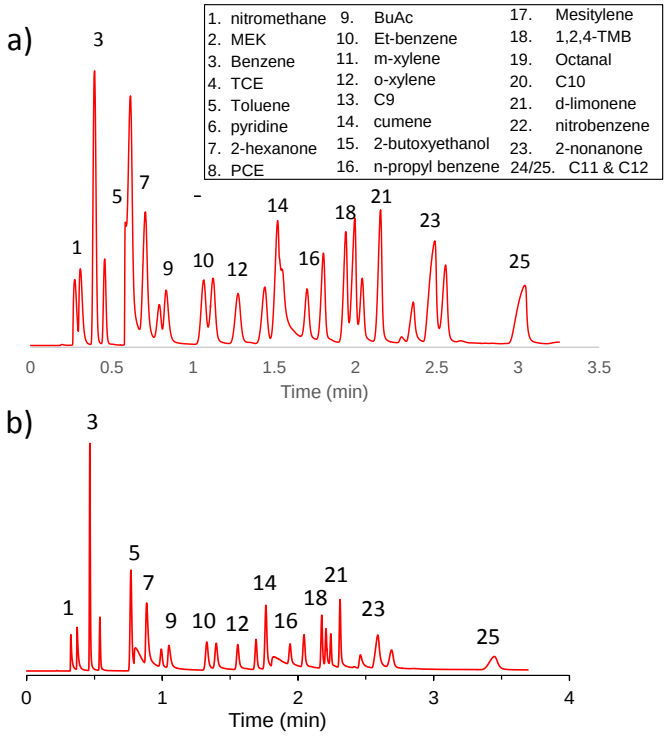

Figure 1.11. Chromatograms of 25 compound hypothetical exposure scenario mixture, separated using Gen-1 dual 3-m µcolumns with a) N2 b) He as carrier gases. Conditions: syringe injection, 3 mL/min, temperature programs were optimized for each chromatogram.

2.4.5 µPCF

Two different µPCF devices were used in the project. The first (Figure 1.12, below) was the original design that used bulk heating of the entire substrate during desorptions. The second (Gen-2) (Figure 1.2a, above) was similar in size but had a more sophisticated (and power efficient) heater design. Most characterization tests were performed with the former devices. The latter were characterized with respect to desorption bandwidth and were incorporated into the PEMM 1 (and PEMM 2) prototypes. In this section we describe tests of both devices starting with the original design. The modeling that was used to designed the Gen-2 devices is described in Section 2.5 of this report.

The original 4.2-mm × 12.1-mm µPCF chips were fabricated from 500-µm thick Si wafers using deep-reactive-ion-etching to create all features. The central cavity, inlet/outlet ports, and the tee-junction adjacent to one side of the cavity were all 380-µm deep (see Figure 1.12). Cylindrical pillars (150-µm spacing and widths) were added just inside the cavity inlet and outlet to retain adsorbent granules, and to divide the cavity into front and back sub-sections, with volumes of 4.7 µL and 2.9 µL, respectively. The walls of the cavity tapered toward the inlet and outlet to reduce turbulence and promote even distribution of the flow stream. Filling ports etched into the sidewalls of each subsection were used for loading adsorbent granules. A 120-µm thick Pyrex plate was anodically bonded to the top surface at wafer level to seal the tops of the devices. Two Ti/Pt contact pads along with a resistive temperature device (RTD) were evaporated onto the backside of the Si for bulk resistive heating and temperature monitoring, respectively. Devices were then diced into individual chips.

Deactivated fused-silica capillaries were sealed into the inlet/outlet ports using silicone adhesive (Duraseal 1531, Cotronics, Brooklyn, NY). Each device cavity or subsection was filled with sieved adsorbent granules using a gentle vacuum. The µPCF device was loaded to capacity, the larger section with 2.0 mg of graphitized carbon Carbopack B (C-B, 100 m^2/g) and the smaller section with 1.4 mg of Carbopack X (C-X, 240 m^2/g). Adsorbent masses were determined by weighing the device with an electronic balance to ±0.1mg before and after loading (note: since C-B has a lower density than C-X, the mass of this adsorbent contained in a given cavity volume is also lower). Devices were then mounted on custom printed circuit boards (PCB) using epoxy (Hysol 1C, Rocky Hill, CT); only the capillaries were bonded to the board to maximize thermal isolation of the device. A rectangular hole in the PCB beneath each device further improved thermal isolation. Al wire-bond wires were used for electrical connections.

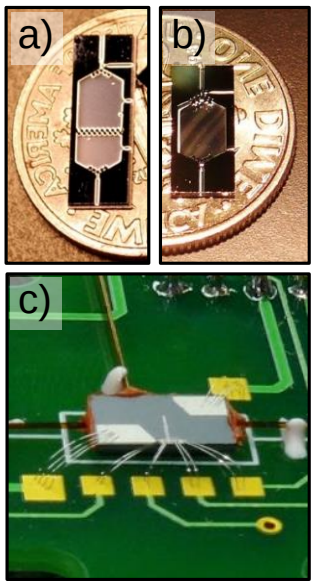

Figure 1.12. *Photographs of a) original µPCF; b) a single-cavity device that will not be discussed in this report (on U.S. dimes for scale); and c) the µPCF inverted and mounted to a custom printed circuit board; device is suspended by the inlet/outlet capillaries that are epoxied to the board for mechanical and thermal isolation. Wire bonded leads are for (bulk) heating and for monitoring temperature via the patterned RTD extending into the center of the chip.*

The redesigned µPCF chip, shown in Figure 1.2a, above, has dimensions of 13.6×4.1 mm and was also fabricated from Si using deep-reactive-ion etching (DRIE). Each cavity is 380 µm deep, has a volume of ~4.7 µL, and is also separated from the adjacent cavity by a row of 150-µm-diameter pillars spaced 150 µm from one another. Filling ports were etched into the sidewalls of each cavity for adsorbent loading. Fluidic ports were etched to snugly accommodate a 250-µm i.d. (380-µm o.d.) fused silica capillary affixed with a flexible, high-temperature silicone adhesive (Duraseal 1531, Cotronics, Brooklyn, N.Y.). The fluidic inlet channel features a tee junction to permit sample loading through one branch and back-flushed injection through the other. A 200-µm thick Pyrex plate was anodically bonded to the top surface at wafer level to seal the cavities and channels. A Ti/Pt resistive heater and resistive temperature device (RTD) were patterned onto the backside of the Si after growing a thin oxide layer for electrical isolation (Figure 1.2a). SolidWorks (R2014, Dassault Systems, Waltham, MA) and COMSOL Multiphysics (R4.2, Burlington, MA) packages were used for heater design and simulations, respectively, to minimize expected temperature gradients across the cavities (discussed more in the next section of this report).

Using mild suction, the front cavity (i.e., during sampling) was loaded with 2.0 mg of C-B and the rear cavity was loaded with 2.3 mg of C-X, as determined gravimetrically to ±0.1 mg. Filling ports were subsequently sealed with Duraseal. The device was inverted, mounted on a custom printed circuit board (PCB) using epoxy (Hysol 1C), and wire-bonded to the PCB bonding pads for electrical connections.

The experimental design and rationale for this set of experiments are described in detail in our publication on the µPCF (ref. Z2 above). Table 1.1 presents the set of 17 test compounds used in the study along with their vapor pressures and TLV values. Desorption testing preceded capacity (breakthrough) testing.

Table 1.1. 17 test compounds with corresponding vapor pressures (p_v) and TLVs.

Compound	Peak #[a]	p_v [b] (kPa)	TLV[c] (ppm)
dichloromethane (DCM)[d]	2	58.0	50
acetone (ACE)[d]	1	31.5	500
2-butanone (MEK)[d]	3	13.3	200
benzene (BEN)	6	12.6	0.5
1,2-dichloroethane (DCA)	5	10.5	10
ethyl acetate (EAC)	4	9.71	400
trichloroethylene (TCE)	7	6.25	10
toluene	9	3.78	20
methyl isobutyl ketone	8	2.65	20
n-butyl acetate	11	1.53	150
2-hexanone	10	1.46	5
ethylbenzene	12	1.27	20
m-xylene	13	1.01	100
cumene	14	0.60	50
1,2,4-trimethylbenzene	15	0.27	25
nitrobenzene	16	0.033	1
n-dodecane	17	0.027	-[e]

[a] Peak assignments for chromatogram in Fig. 1.17.
[b] Values at 25 °C.; [c] TLV-TWA; [d] High-volatility interferences.
[e] No assigned TLV value.

2.4.5.1 Desorption Testing. Three compounds spanning the range of p_v values of the compounds listed in Table 1.1 were chosen for desorption testing: benzene, toluene and n-dodecane. The effects of desorption flow rate, heating period, vapor loading, and split ratio on the desorption efficiency and bandwidth were evaluated for each VOC individually. No column was used for these single-VOC tests; the valve was plumbed directly to the FID via deactivated fused silica capillary, and both were heated to minimize any adsorption during transfer. Where separations were required, a 6-m capillary column (250-µm i.d.; 0.25-µm thick Rtx-1; Restek, Bellafonte, PA) was used. The effect of increasing the desorption flow rate while maintaining a constant flow rate to the detector was explored by splitting the flow downstream from the µPCF using a 'Y' press-tight connector. Split ratios were adjusted using the GC inlet head pressure and lengths of capillary on the vent line to create the appropriate pressure drops.

Figure 1.13 shows the effect of desorption flow rate on the injection band width from the µPCF for benzene, toluene, and n-dodecane. Each compound was tested individually, in

triplicate, by drawing a 5 mL sample of a test atmosphere containing 3-6 ppm of the compound (~50 ng) through the μPCF at 5 mL/min, reversing the direction of flow, and then heating to 225 °C in < 1 sec and holding for 60 sec. As shown, the *fwhm* values of the desorbed peaks were inversely proportional to flow rate, with a dependence that varied inversely with p_v. The ratios of *fwhm* values at 1 and 5 mL/min were 1.8, 2.4, and 2.7 for benzene, toluene, and n-dodecane, respectively. Benzene consistently gave the sharpest peaks, but at the highest flow rate of 5 mL/min its peak was only slightly narrower than that of toluene, and only 28% narrower than that of n-dodecane.

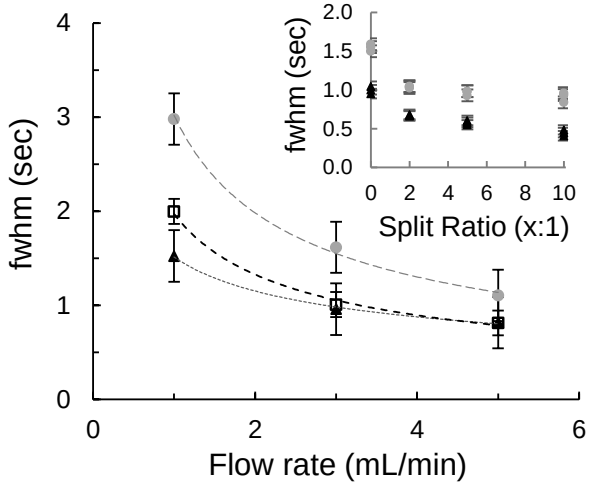

***Figure 1.13**. Desorption bandwidth (i.e., fwhm) from the μPCF as a function of flow rate for benzene (triangles), toluene (squares), and n-dodecane (circles), tested individually without a downstream column; FID. Error bars represent 95% confidence intervals (n=3). Curves represent the least-squares fits to the data. Inset shows the effect of the injection split-flow ratio (vent:analysis) on the fwhm values for benzene and n-dodecane; analytical path flow rate was maintained at 3.0 mL/min.*

The inset in Figure 1.13 shows the effect on the *fwhm* values of benzene and n-dodecane of increasing the desorption flow rate further by incorporating an injection split. By venting a portion of the downstream flow stream, sharper injections are possible without altering the flow rate passing through the GC column. For an analytical path flow rate of 3 mL/min and split ratios of 2:1, 5:1, and 10:1 (i.e. desorption flow rates of 9, 18, and 33 mL/min, respectively), the *fwhm* decreased by 33%, 42% and 55% for benzene and by 36%, 40% and 44% for n-dodecane relative to the splitless injection at 3 mL/min.

For n-dodecane and compounds of similar or lower volatility, on-column focusing can mitigate the effects of injection band broadening and asymmetry,[47] and for compounds of somewhat higher volatility (e.g., toluene), which are not focused at the head of the column, the retention times are long enough to expect reasonable chromatographic resolution. In contrast, for benzene and similarly volatile compounds, injection band broadening has a greater influence on their resolution due to their short retention times. To evaluate the latter, in a subsequent test series, a 6-m capillary column was connected downstream from the μPCF and the chromatographic resolution (R_s) of benzene from a similarly volatile compound, trichloroethylene (TCE), was evaluated as a function of desorption flow rate and injection split ratio. Estimates of R_s (= Δt_R $[4\sigma_a]^{-1}$) were calculated from the difference in retention times, Δt_R, and the average standard deviation of the Gaussian profiles fitted to the peaks, σ_a.

Figure 1.14a shows results for splitless injections of 50 ng of each compound at each of three flow rates. All peaks fit Gaussian profiles with $R^2 > 0.98$. Interestingly, there was little

change in R_s on going from 1 to 3 mL/min; the narrowing of the peaks was accompanied by a commensurate reduction in t_R values. Since the optimal velocity for separations on this type of column corresponds to a flow rate < 1 mL/min, we would have expected a decrease in R_s at the higher flow rate. Evidently, the reduction in the injection band width compensated for the loss in chromatographic efficiency over this range of flow rates. At 5 mL/min, however, the latter factor dominated and there was a significant decrease in R_s, consistent with the data in Figure 1.13 showing relatively little reduction in the injection band width above 3 mL/min.

Figure 1.14b shows the dependence of R_s and sensitivity on the injection split ratio, while maintaining a flow rate of 3 mL/min in the analytical path. The ~linear increase in R_s with the split ratio follows from Δt_R remaining constant while the widths of both peaks decreased at the same rate with increasing desorption flow rate. The tradeoff is a loss in sensitivity from venting large portions of the sample. As shown in Figure 1.14b, the fractional reduction in average peak height was much less than that of average peak area because of the compression of the injection band. In any case, the relative gain in resolution (~1.4 fold) was smaller than the relative loss in sensitivity (~2.5-3 fold) over this range of split ratios.

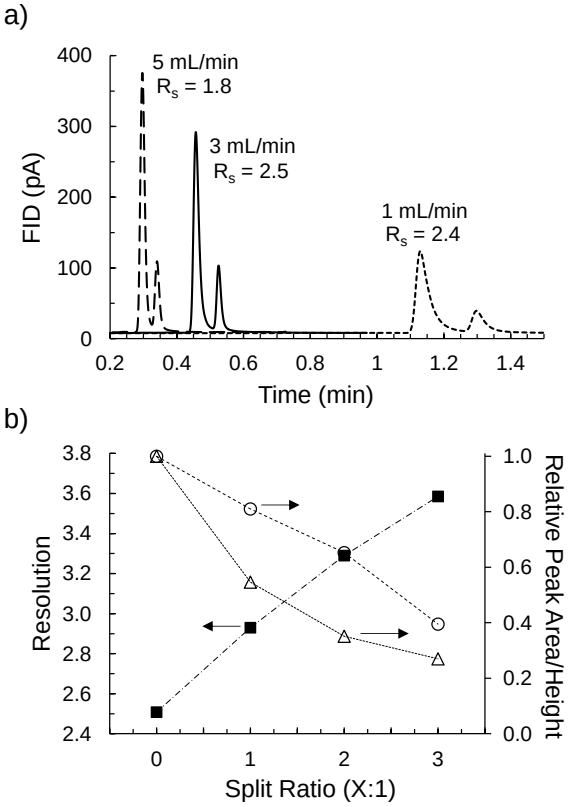

Figure 1.14*. a) Superimposed chromatograms of benzene (1st peak) and trichloroethylene (2nd peak) collected at three flow rates (as indicated), with the corresponding R_s values for the pair. Samples of the binary vapor mixture (~50 ng each) were pre-loaded into μPCF, desorbed/injected splitless in He, and separated on a 6-m long, PDMS-coated capillary column isothermally at 30 °C; FID. b) R_s (squares), average peak height (circles), and average peak area (triangles) for benzene and trichloroethylene plotted as a function of the injection split-flow ratio (vent:analysis), with the column (analytical path) flow rate maintained at 3.0 mL/min.*

2.4.5.2 Desorption Efficiency. Tests were then performed to determine the minimum time period required to remove all traces of analytes from the μPCF during thermal desorption. Once again, benzene, toluene, and n-dodecane were used as the test compounds to span the range of volatility expected of any samples that might be collected. Results are summarized in Table 1.2. Heating for 20 sec was sufficient to desorb >99% of the benzene and toluene, but only 97% of the n-dodecane. For heating periods of 40 and 60 sec, the desorption efficiencies of n-dodecane were 99 and >99%, respectively. Increasing the initial VOC mass loading from 250 ng to 1 μg had no effect on desorption efficiency for benzene and < 1% decrease for n-dodecane. Therefore, 40 sec was deemed sufficient to avoid carryover of any low volatility analytes.

Table 1.2. Desorption efficiencies (DE) of three test compounds from μPCF for different heating periods; T_{max} = 225 °C.

	Avg. DE (%)[a]		
Compound	20 sec	40 sec	60 sec
benzene	>99	>99	>99
toluene	99	>99	>99
n-dodecane	97	99	>99

[a] Compounds were tested individually; ~250 ng of vapor was loaded for each test; desorption flow rate = 3 mL/min; n = 3 for each case (RSD < 8% in all cases); resolution of the determination was 0.5-1%.

2.4.5.3 Breakthrough Testing. Test atmospheres were drawn through the μPCF and a downstream 25-μL or 250-μL sampling loop using the pump at discrete flow rates between 4 and 10 mL/min. At 30-sec intervals, the six-port valve was actuated to inject the contents of the loop into the 6-m capillary column in the GC oven while the pump continued to draw sample through the μPCF. Devices were cleaned after each exposure by heating to 200 °C for 10 min under N_2 flow.

By convention, the sample volume required for the concentration downstream from the μPCF (C_x) to reach 10% of the inlet concentration (C_o), was used as the metric of the dynamic adsorption capacity of the devices, and is designated V_{b10}. This is considered the maximum sampling volume for exhaustive (quantitative) capture. All V_{b10} values were estimated to the closest 0.5 mL.

Following some initial range-finding tests, the μPCF was challenged with a mixture of benzene, toluene, ethylbenzene, and xylene (i.e., BTEX), each at its respective TLV concentration except for benzene, which was at 2×TLV to permit reliable quantification of V_{b10}. Replicate tests (n = 3) were performed under both dry and humid (88% relative humidity, RH) conditions in N_2. A representative set of breakthrough curves is presented in Figure 1.15. Average V_{b10} values for the sentinels benzene and toluene were 33 and 90 mL, respectively (RSD < 3%). For ethylbenzene and xylene, V_{b10} was consistently > 150 mL, at which point the tests were terminated. These results confirm that the μPCF has sufficient capacity to quantitatively retain BTEX mixtures at relevant concentrations above the 31-mL sample volume necessary to detect benzene at 0.1×TLV.

Although it is likely that toluene would start to displace benzene from the C-X by competitive adsorption once it breaks through the C-B bed, this did not occur under these test conditions. No changes in V_{b10} were observed for any of the compounds at a higher background humidity level.

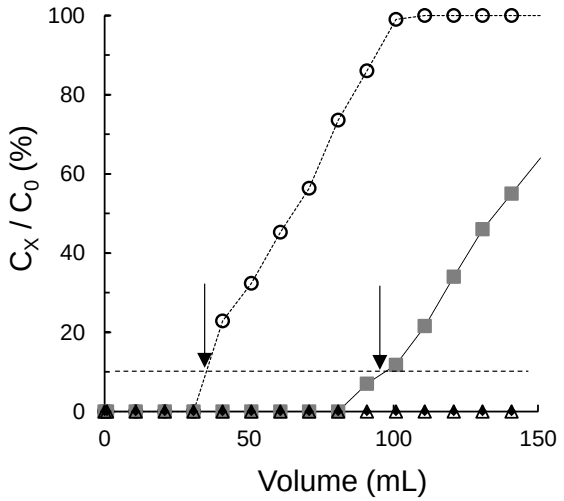

Figure 1.15. *Representative breakthrough curves of µPCF-2 challenged with a mixture of benzene, toluene, ethylbenzene and m-xylene (i.e., BTEX) at 1, 20, 20, and 100 ppm, respectively (i.e., TLV concentrations for all except benzene) in N_2. C_x/C_o is the breakthrough fraction. V_{b10} values for benzene (33 mL) and toluene (90 mL) are designated by the vertical arrows. V_{b10} values for ethylbenzene and m-xylene were > 150 mL. Conditions: flow rate = 5 mL/min; temperature = 30 °C; FID.*

The next set of breakthrough tests was designed to characterize capacity at much higher concentrations. In lieu of using a challenge test atmosphere containing a large number of compounds, mixtures of four representative compounds at higher concentrations were used. This permitted measurements at a higher frequency because chromatographic separation times were shorter. For characterizing C-X, a mixture of 2-butanone, benzene, ethyl acetate and toluene was used, and for C-B a mixture of toluene, cumene, 1,2,4-trimethylbenzene and n-dodecane was used. Within a subset, compounds were included that spanned the range of p_v values appropriate for that adsorbent material, although including toluene in the mixture for C-X was actually a more rigorous test, because the vapors intended to be captured on C-X have higher p_v values. The challenge mixtures contained 100, 150, or 200 ppm of each compound. At 200 ppm, the net (composite) mass per unit volume concentration was roughly equivalent to that of all of the target compounds in Table 1.1 at their respective TLV concentrations (note: since n-dodecane has no assigned TLV, a concentration of 10 ppm was assumed).

Table 1.3 shows the measured V_{b10} values as a function of flow rate and temperature for the subset of compounds intended to characterize the performance of the C-X bed. As expected, V_{b10} varied inversely with p_v among the test compounds under all conditions. Values of V_{b10} for the high-p_v interference 2-butanone (p_v = 13.3 kPa) were consistently the smallest observed, never exceeding 7 mL, while the values of V_{b10} for toluene consistently exceeded those of the other compounds by >2 fold. Benzene had V_{b10} values ranging from only 7.5 to 11 mL. For all concentrations at 30 °C there was a very slight decrease in V_{b10} with increasing flow rate as expected. V_{b10} also decreased with the 2-fold increase in C_o, but only for toluene was the decrease > 12% (i.e., ~26%).

The relative insensitivity to flow rate and concentration are both predicted by the Wheeler Model. The small concentration dependence reflects the increase in the dynamic

adsorption capacity with increasing concentration in the sub-monolayer regime where that model is applicable. The Wheeler Model also predicts the breakthrough volume to increase in proportion to the bed mass.

Temperature had a large impact on V_{b10} for all compounds; an increase from 25 to 40 °C, which corresponds to only a 5% increase on the Kelvin scale (i.e., 313/298) resulted in reductions of 2.5-3.2 fold in V_{b10} among the C-X test compounds. Since diffusion coefficients *increase* with temperature, the loss in capacity must be due to a decrease in the dynamic adsorption capacity, which should vary as $e^{-\alpha T}$, where T is temperature in Kelvin and α is proportional to the enthalpy of adsorption. These results serve to highlight the importance of maintaining the μPCF device at a low temperature and, in particular, to allow it sufficient time to cool down after each injection prior to starting to collect the subsequent sample with the PEMM prototype.

We note that V_{b10} for benzene with the μPCF at 30 °C did not reach the benchmark value of 10 mL for any of these high-concentration challenge mixtures. Similarly, the ethyl acetate V_{b10} values barely exceeded the benchmark value. Although the V_{b10} estimates obtained by testing with these high VOC concentrations are conservative, affording some margin of safety for cases in which additional compounds of similar or lower volatility might be present, these results led us to conclude that the bed mass of C-X in the next-generation dual-cavity μPCF devices to be installed in the PEMM prototype must be increased to 2.3 mg. We conclude that 2.0 mg of C-B is sufficient for trapping the less volatile fraction of anticipated VOC mixtures, and the next-generation μPCF to be used in the PEMM prototype should be designed to hold this mass of C-B.

Table 1.3 Values of V_{b10} for mixtures of representative VOCs drawn through the original μPCF as a function of concentration, temperature, and sampling flow rate.

Compound	Flow rate (mL/min)	V_{b10} (mL)					
		30 °C			100 ppm		
		200 ppm	150 ppm	100 ppm	25 °C	35 °C	40 °C
2-butanone	4	4.5	5.0	5.0	5.0	3.0	2.0
	6	4.5	4.5	5.0	-[b]	-	-
	8	4.0	4.5	4.5	-	-	-
	10	4.0	4.0	4.5	-	-	-
benzene	4	8.5	8.5	9.0	9.5	4.5	3.0
	6	8.0	8.0	8.5	-	-	-
	8	7.5	8.0	8.5	-	-	-
	10	7.5	8.0	8.5	-	-	-
ethyl acetate	4	11.0	11.5	12.0	12.5	7.0	4.5
	6	11.0	11.5	11.5	-	-	-
	8	10.5	11.0	11.5	-	-	-
	10	10.0	11.0	11.0	-	-	-
toluene	4	27.0	32.0	37.0	46.0	27.0	17.0
	6	25.0	30.0	35.0	-	-	-
	8	25.0	30.0	34.0	-	-	-
	10	24.0	29.0	32.0	-	-	-

[a] tested at 5 mL/min instead of 4 mL/min; [b] denotes untested conditions.

2.4.5.4 17-VOC Mixture Capture and Injection. The performance of the original μPCF was then evaluated with a test atmosphere containing a mixture of the 17 compounds in Table 1.1, each at 10 ppm to facilitate rapid separation and detection of low breakthrough fractions with the downstream capillary column and FID. The sampling flow rate was 5 mL/min and the test was concluded when the total sample volume reached 60 mL. The breakthrough curves in Figure 1.16a demonstrate the partial selectivity against high-p_v compounds: the V_{b10} values of dichloromethane, acetone, and 2-butaone were all smaller than that of benzene, and the former two compounds reached 100% breakthrough prior to V_{b10} for benzene. Although a fraction of the sampled mass of each of these compounds was retained, it was much lower than that of the sentinel benzene and other targets. Surprisingly, the V_{b10} of 1,2-dicholoroethane was also slightly smaller than that of the more volatile benzene, which can be ascribed to the dipolarity of this compound and consequent lower affinity for the non-polar C-X surface. Despite the presence of several compounds competing for adsorption sites on the C-X, the V_{b10} of benzene was still 31 mL.

Figure 1.16b shows the chromatogram obtained by sampling at 5 mL/min for 4 min through the μPCF-2, followed by heating, back flushing, and injecting the sample with a 2:1 split and an analytical path flow rate of 3 mL/min of He. A 20-mL sample volume was used for convenience to illustrate the selective preconcentration and, at the same time, generate reasonably large peaks for all compounds. As shown, all 17 compounds were separated in < 3 min. Acetone and dichloromethane eluted first and gave much smaller peaks due to selective preconcentration. The 2-butanone eluted next and gave a large peak due to its being retained to a greater extent than the other two interferences. The remaining 14 compounds were captured quantitatively from the 20 mL sample (see Figure 6a; total mass of ~12 μg) and the injected masses of each ranged from 630 to 1380 ng prior to the split. Notably, both 1,2-dichloroethane and ethyl acetate eluted before benzene due to their higher polarity, and gave somewhat smaller peaks, presumably due to their having smaller response factors in the FID.[47]

Among the 14 targets the chromatographic resolution was quite good, with values of R_S > 1.0 in all cases. Prior work demonstrated about a 10% reduction in resolution of early eluting peaks for the microcolumns to be used in the PEMM prototype relative to a commercial capillary like that used here, indicating that the separation of similar mixtures should be comparable. The inset in Figure 1.16b shows that the first six compounds were separated in < 24 sec. Some tailing was evident in all of the peaks, but asymmetry factors were < 1.6 in all cases due, in part, to the sharp split injection. The small *fwhm* values of peaks 13-17 (i.e., 0.8 to 1.3 sec) reflect the influence of on-column focusing at the outset of the separation. The somewhat larger *fwhm* values of peaks 7-12 (i.e., 1.2 to 1.7 sec) reflect the fact that these compounds are too volatile to be focused, and they have wider effective injection bands and spend more time on the column than the more volatile compounds (i.e., peaks 4-6) for which *fwhm* ranged from 0.8 to 1.1 sec). Regardless, none of the peaks is excessively broad and all are well separated. Moreover, there is additional space available in the mid-range of the chromatogram to accommodate other compounds that might be encountered in practice in this volatility range.

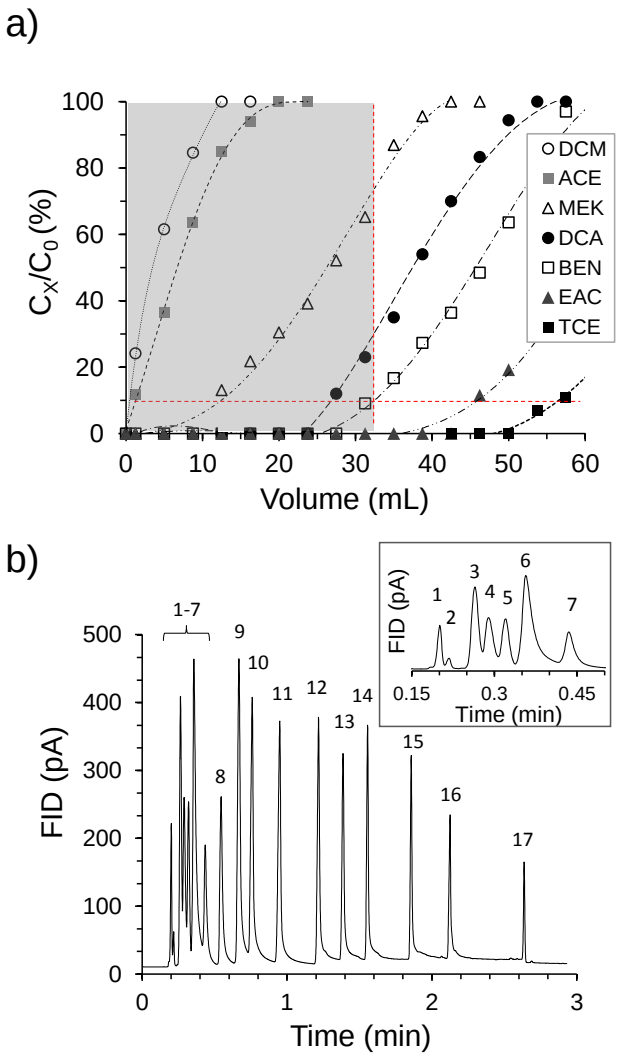

Figure 1.16. *a) Breakthrough curves of μPCF challenged with the 17-VOC mixture (see Table 1 for acronym definitions) at 30 ℃ and 5 mL/min with C_o = 10 ppm for each compound; only the first seven compounds to break through were monitored. Shaded region corresponds to $V \leq V_{b10}$ for benzene. b) Chromatogram of a 20-mL sample of the same 17-VOC test atmosphere injected from μPCF-2 and separated on a 6-m capillary column; inset shows enlargement of the first seven compounds to elute (see Table 1 for peak # assignments). Conditions: 3 mL/min; 2:1 split injection; column held at 28 ℃ for 0.5 min, then 10 ℃/min to 33 ℃, then 50 ℃/min to 125 ℃.*

2.4.5.5 Preconcentration Factors (PF). Assuming no breakthrough, the PF is the ratio of the volume of the air sample collected to the volume in which that same mass is contained at the point of detection. The latter can be taken as the volume of the peak generated directly from the injection or after chromatographic separation. The latter volume will differ from the former due to on-column focusing or broadening of the injection band, but using it to determine an "effective PF", while less rigorous, is more practical, since all analyses will include a separation step prior to detection. Note that the practice of calculating "preconcentration factors" from the ratio of peak areas generated with and without a μPCF included in the system is not recommended, because it does not afford any useful information about the critical performance parameters of a μPCF.

For the most volatile target, benzene, an injection *fwhm* value of 0.90 sec was obtained at 3 mL/min (no split), which corresponds to a preconcentrated volume of 0.048 mL. Assuming a 31-mL sample volume, then we obtain a PF value of ~620 for benzene. For our least volatile target, n-dodecane, the injection *fwhm* value was ~1.7 sec at 3 mL/min (no split), which corresponds to a peak volume of 0.085 mL. For a sample volume of 31 mL, this yields a PF value of only 370. Note, however, that V_{b10} for n-dodecane was > 150 mL under all conditions tested. Increasing the assumed sample volume to 150 mL leads to a PF of 1590, even after allowing for a 10% increase in the *fwhm* value of the peak at the higher injection mass.

If an injection split were used, then there would be a commensurate reduction in PF due to the loss of sample mass, which would greatly exceed the decrease in *fwhm* afforded by the split (see Figure 1.14b). For example, from Figure 1.16b, the *fwhm* values of benzene and n-dodecane after separation on a 6-m column at 3 mL/min with a 2:1 injection split were 1.5 and 1.9 sec, respectively. The effective PF values using the corresponding peak volumes of 0.076 mL and 0.097 mL together with the 20 mL sample volume, were only 88 and 68 for benzene and n-dodecane, respectively, reflecting the small sample volume and the loss of ~67% of the sample from the split injection.

2.4.5.6 Redesigned (Gen-2) μPCF Desorption Efficiency. All of the data generated above was with the original μPCF. We revised the design in light of the results and created a new device. The redesigned device is pictured in Figure 1.2 and was described above in Section 2.4.5. The modeling that ld to the new heater design of this device is described in Section 2.5 of this report (Phase 2/Aim 2).

The redesigned "Gen-2" μPCF was not tested again for capacity, but was for desorption because of the new heater design. The injection bandwidth was characterized using a bench-scale GC-FID (7890 Agilent, Santa Clara, CA) with the μPCF connected across two ports of a 6-port valve. Test atmospheres containing selected VOCs in N_2 were generated in Flex-foil® inert gas sample bags (Supelco). A suction pump (model UMP015, KNF Neuberger, Trenton, N.J.) was used to draw a sample from the bag through the μPCF to load 50-100 ng of analyte, after which the valve was switched, and He from the GC injection port was backflushed through the μPCF while it was heated. An initial fast (uncontrolled) ramp of 400 °C/sec was used to heat from 30 to 100 °C, followed by a pulse-width modulated (PWM) ramp of 150 °C/sec to 225 °C, which was maintained for 40 sec, as subsequently applied for the injection step with the prototype. Passive cooling to 30 °C required ~90 sec. Injected samples were passed to an FID via a section of capillary maintained at 100 °C.

A limited set of tests of the injection band width was conducted at an analytical-path flow rate of 3 mL/min for both splitless injections and injections with a 2:1 split ratio (vent:analysis). Benzene, toluene, and C_{12} (~5 ppm each) were tested to span the range of target-VOC p_v values. The values of full width at half maximum (*fwhm*) of the FID peaks measured with splitless injection were 0.94, 1.0, and 1.4 sec, respectively, and the asymmetry factors were 1.1, 1.7 and 2.3, respectively. Desorption efficiencies were >99%. With a 2:1 split (i.e., desorption, 9 mL/min; analysis, 3 mL/min), the *fwhm* values decreased to 0.59, 0.79, and 0.85 sec,

respectively, and the asymmetry factors for toluene and C_{12} decreased by approximately 10% (data not shown). These *fwhm* values are somewhat smaller than those observed with the original μPCF, attesting to the improved heater of the new device.

The sharp injections for benzene and toluene are more important for achieving good chromatographic resolution because C_{12} and compounds of similar volatility benefit from on-column focusing. Thus, in those cases where separation of earlier eluting compounds is more important than sensitivity, split injection is advantageous.

2.4.5.7 Summary Remarks About the μPCF. The design and operating features of the μPCF developed here meet or exceed the requirements of this component of the (wearable) μGC into which it will be integrated for the specific application of quantitatively analyzing exposures to mixtures of VOCs encountered in workplace environments. Thus, a dual-cavity μPCF containing 2.0 and 2.3 mg of C-B and C-X, respectively, operated at a flow rate of 5-10 mL/min yields V_{b10} values ranging from ~10 mL to > 40 mL for mixtures of ~10-20 compounds in the designated volatility range, with preconcentration factors of ~200 to 1,600 and sampling times of ≤ 5 min.

The approach taken here has entailed careful consideration of device-level and system-level factors, fluidic and thermal factors, and numerous application-specific variables in resolving the trade-offs in selectivity, capacity, desorption efficiency, and desorption bandwidth, which are the critical performance metrics. This study complements others from our group on this topic by further elucidating and addressing the details of μPCF design and implementation in high-performance micro-analytical systems for VOC mixture determinations.

Delimiting the range of target compounds on the basis of volatility (i.e., p_v values from 0.03 to 13 kPa) was rationalized on practical and fundamental grounds, and is a common, if not requisite, feature of fieldable μGC instrumentation; inherent constraints on the complexity of mixtures that can be analyzed by such instrumentation demand such concessions. Delimiting the concentration range for any specific VOC in terms of its ACGIH TLV value (i.e., 0.1 to 2×TLV) was also rationalized on practical grounds, though proved difficult to implement because it translated into a concentration range > 10^4 when all target compounds were considered collectively. This will likely demand the designation of two operating modes (i.e., "high" and "low" concentration) for the μGC, which will differ in sample volume.

Selectivity against high-volatility interferences was achieved/demonstrated while retaining the capability for exhaustive capture of target compounds, in mixtures, at relevant concentrations. The breakthrough volumes and associated quantities of target compounds captured (and subsequently thermally desorbed) were sufficiently large to ensure detection at < 0.1 TLV by the microsensor array to be used as the μGC detectors. Conditions established for desorption and injection into a downstream separation column ensured > 99% desorption efficiency and injection bandwidths narrow enough to permit high chromatographic resolution of mixture components. The latter could be enhanced by use of split injection in cases where the accompanying loss in sensitivity could be tolerated. Given that the PEMM prototype is being designed to operate in a variety of occupational settings and to monitor a variety of possible VOC mixtures, the capability for adjusting the split ratio is to be incorporated via a metering valve downstream from the μPCF.

2.4.6 μCR Array

The μCR array chip (33×20×0.5 mm; Figure 1.2c) has a set of 5 primary and 5 back-up Au (300 nm)/Cr (30 nm) interdigital electrodes (IDE) in a single row, with a Au/Cr RTD at the center that was deposited and patterned via a standard lift-off process onto a Pyrex substrate. Each μCR contains 27 pairs of IDEs 5 μm wide, spaced 4 μm apart, and overlapping by 210

μm. A meander-line Ti/Pt heater was patterned on the backside. Header pins were bent to 90^0 and low-temperature soldered to each of the 22 IDE bonding pads. Cables were soldered to the heater bonding pads. A Si lid (33×10×0.5 mm) was also fabricated with a linear, recessed DRIE channel, 150 μm deep × 350 μm wide, running lengthwise down the center to align directly above the sensors in the array. The linearity of the interconnection with external capillaries was an improvement over previous μCR array configurations. The array was plugged into a socket on a carrier PCB, and the entire assembly was covered with a grounded Cu Faraday cage.

MPNs (3.5-5 nm Au core diameter) derived from the following thiols were used as μCR interface films: n-octanethiol (C8), isooctyl-3-mercaptopropionate (EOE), methyl-6-mercaptohexanoate (HME) and 1-mercapto-(triethylene glycol) methyl ether (TEG). TEG was purchased (Nanoprobes, Yaphank, NY). Other MPNs were synthesized in-house. MPNs were dissolved in suitable solvents (toluene for C8, OPH, and TEG; chloroform for EOE, dichloromethane for HME) at concentrations of ~5 mg/mL. Each sensor was coated with a film of one type of MPN by drop casting from a 1-μL syringe to create multilayer films with baseline resistances between 100 kΩ and 10 MΩ, depending on the MPN and the film thickness. The film thicknesses were not uniform and were not measured but were roughly estimated to be on the order of 200-500 nm on average on the basis of previous work.

After coating, 0.3×2.5 cm strips of 50-μm thick double-sided adhesive tape (VHB tape, 3M, St Paul, MN) were mounted along both sides of the array, the Si lid was pressed down onto the tape, and a narrow bead of Hysol was applied along the outer seam. Short segments of deactivated inlet/outlet capillary (250 μm i.d.) were sealed to the fluidic ports (Hysol) for connection to other devices via press-tight unions. Although the integrated heater on the μCR array could be used to control temperature via a constant voltage bias, it was eventually found to be unnecessary.

2.4.7 PEMM 1 Prototype

2.4.7.1. System Integration and Prototype Assembly. Two custom PCBs were designed, fabricated (Advanced Circuits, Aurora, CO), populated, and checked for proper performance. One PCB was dedicated to the microsystem components and the other to the mini-pump, mini-valves, and fans. Individual carrier PCBs for each microsystem device were mounted on stand-offs to the baseplate board. For more details, please refer to the Ref. 1 above.

Figures 1.2d and 1.2e show the arrangement of the PCBs and fluidic components prior to final assembly and the fully assembled PEMM-1 prototype, respectively. The PEMM-1 measures 15.2 (h) × 30.5 (w) × 14 (d) cm and weighs 3.18 kg. The rear-panel-mounted He canister and regulator increase the net depth by 3.8 cm and the weight by 0.34 kg. In Figure 2d, the three carrier PCBs are shown (*sans* microcomponents) mounted on stand-offs to a single base-plate PCB. Beneath this PCB, arranged in order, are the microsystem control PCB, DAQ board, and fluidic-control PCB. The custom stainless-steel valve manifold accepts zero-dead-volume fittings for capillary interconnects and five face-mounted, 3-way, latching solenoid valves (Model LHLA1221111H, Lee Co., Westbrook CT). A wall-mounted diaphragm mini-pump (NMP-09M, KNF Micro AG, Reiden, Switzerland) collected the air samples. Two miniature needle valves (Beswick, Greenland, NH) were mounted to the front panel (Figure 1.2e) for manual adjustment of the sampling flow rate and injection split-flow ratio.

Sections of stainless-steel tubing (750 μm i.d.) and fused silica capillary (250 μm i.d.) were used for fluidic interconnections. For the latter, press-tight unions (Supelco) were used, with a subset wrapped in polyimide-embedded resistive film heaters (Omega, Stamford, CT) held at ~80 °C. Voltage regulators for the pump and solenoid valves were mounted to the inside of the front panel. Small axial fans were used for cooling. The 24-V DC power was supplied through an AC-to-DC converter connected to wall power. For most initial testing, a separate

compressed gas cylinder of He was connected through the bench-scale GC for pressure regulation and subsequently to the fitting on the prototype used later to connect the on-board He canister regulator. The head pressures necessary to achieve a flow rate of 3 mL/min through the analytical system (both splitless and with a 2:1 split) were 18 and 23 psi, respectively.

2.4.7.2. System Control, Data Acquisition and Processing. The instrument was operated from a laptop computer running a custom LabVIEW (Ver. 14.0, National Instr., Austin, TX) program. Operating parameter settings and control functions were entered through a graphical user interface (GUI) for either manual operation of each run or multiple continuous runs. Independent proportional-integral-derivative (PID) feedback loops were designed to control heating rates and temperatures via solid-state relays and PWM of the generated signals. Although not critical for this prototype, power efficiency was considered in the design of the components. The power and energy per analysis are provided in Ref. Z1.

Raw chromatogram traces were stored as text files and analyzed using OriginPro (Ver. 9.1, OriginLab, Northampton, MA). Calibration curve regression models and response patterns were generated in Excel. Monte Carlo simulations coupled with extended disjoint principal components regression (MC-EDPCR) analyses were implemented in Visual Basic via custom programs.

2.4.7.3. PEMM 1 System Design and Operation Specifications. Per above, by design, air samples are drawn by the mini-pump through the inlet, and low volatility interfering VOCs are retained by the wall-coated-capillary pre-trap (Figure 1.1). The air sample then passes through the µPCF, where target VOCs are quantitatively captured in one of the two adsorbent beds. After turning off the pump and switching the valves to start the flow of He through the microsystem, the µPCF is rapidly heated to thermally desorb the captured VOCs for passage to the µcolumns in a narrow band. Temperature-programmed separation of the VOC mixture components is performed, with detection provided by the transient changes in the resistance of the MPN-coated µCRs in the array as VOCs reversibly sorb into the MPN films to different extents, giving rise to a response pattern. The flow is then redirected to backflush the pre-trap and the fore-line to purge any residual VOCs, and the µcolumns are allowed to cool in preparation for the next cycle.

Several performance criteria were used to rationalize the design, integration, and operation of the instrument components. The primary constraint placed on the target VOCs was that they fall within a p_v range of ~0.03 to 13 kPa. Less volatile compounds would tend to adhere to surfaces in the (unheated) fluidic pathways, and more volatile compounds would be difficult to trap, separate, and detect because these functions rely on partitioning phenomena. Where possible, target VOCs were chosen that also had assigned Threshold Limit Values (TLV®), which serve as reference values for specifying the ranges of concentrations to be encountered. To assess the selectivity of the pre-trap and µPCF, we included several potentially interfering compounds outside of the designated p_v range. For the target VOCs, a set of 17 common workplace VOCs was selected with the understanding that actual workplace exposures might involve greater or fewer VOCs in practice. Table 1.4 lists the set of 24 target and interfering VOCs selected, together with p_v values and assigned TLVs.

Results from previous studies were considered in the selection of the µPCF adsorbents, the µcolumn stationary phase and total length, the number of sensors and nature of MPN coatings for the µCR array, and the 5- and 10-mL air sample volumes used at the outset. For the latter, we assumed a working limit of detection (LOD) of ~5 ng for the µCR sensors. A 40-fold concentration range limit was imposed, indexed to the TLV Time-Weighted Average (TLV-TWA, 8-hr average) for each VOC. That is, it was assumed that 0.1×TLV was a suitable LOD-level concentration to measure and that 4×TLV was a suitable maximum quantification limit for any given measurement. Several target compounds also have an assigned Short-Term

Exposure Limit TLV (i.e., TLV-STEL), which is a 15-min average limit set to protect against acute health effects, and is usually within 4× the TLV-TWA (see Table 1.4).

Table 1.4. List of 24 test compounds with corresponding vapor pressures (p_v), TLVs, and limits of detection (LODs) for the PEMM-1 prototype (10-mL air sample; 2:1 split injection).

No.[a]	Compound	Acronym	p_v[b] (kPa)	TLV[c] (ppm)	LOD[d] (ppm) EOE	C8	OPH	TEG	HME
1	methanol	MOH	16.9	200/250	nd[e]	nd	nd	nd	nd
2	n-pentane	C_5	68.5	1000	nd	nd	nd	nd	nd
3	diethyl ether	DEE	71.7	--[f]	nd	nd	nd	nd	nd
4	acetone	ACE	30.8	250/500	nd	nd	nd	nd	nd
5	dichloromethane	DCM	58.0	50	nd	nd	nd	nd	nd
6	2-butanone	MEK	12.1	200/300	nd	nd	nd	nd	nd
7	ethyl acetate	EAC	12.4	400	nd	nd	nd	nd	nd
8	benzene	BEN	12.6	0.5/2.5	0.89	1.0	3.0	1.8	2.8
9	trichloroethylene	TCE	9.2	10/25	0.56	1.1	4.1	1.0	10
10	n-heptane	C_7	6.13	400/500	1.2	1.7	10	8.1	15
11	4-methyl-2-pentanone	MIBK	2.65	20/75	1.3	2.4	3.7	2.1	4.2
12	toluene	TOL	3.78	20/--	0.69	0.80	2.6	1.7	2.7
13	2-hexanone	MBK	1.46	5/10	1.9	5.4	5.8	3.0	7.4
14	butyl acetate	BAC	1.53	50/150	0.69	0.88	1.3	1.1	2.3
15	ethylbenzene	ETB	1.27	20/--	0.48	0.55	1.8	1.5	2.1
16	m-xylene	XYL	1.01	100/150	0.42	0.48	1.3	1.2	1.9
17	3-heptanone	EBK	0.187	50/75	0.35	0.51	0.71	0.71	1.4
18	n-propylbenzene	PPB	0.456	--[f]	0.43	0.51	2.1	1.9	2.0
19	1,2,4-trimethylbenzene	TMB	0.270	25/--	0.34	0.38	1.7	1.7	1.7
20	n-decane	C_{10}	0.191	--[f]	0.25	0.39	2.4	2.5	3.3
21	nitrobenzene	NBZ	0.033	1/--	0.23	0.66	0.29	0.44	0.34
22	n-undecane	C_{11}	0.055	--[f]	0.61	1.1	4.9	9.4	7.1
23	1,2,4-trichlorobenzene	TCB	0.039	5(C)	0.10	0.12	0.21	0.25	0.44
24	n-dodecane	C_{12}	0.027	--[f]	4.6	6.2	35	28	26

[a] Peak assignments for chromatograms in Fig. 1.18. [b] At 25 °C. [c] 2017 ACGIH TLV booklet; 8-hr TLV-TWA is listed first; if a TLV-STEL is assigned to a cmpd, then it is listed second; for TCB, the C designation indicates that the TLV is a ceiling limit. [d] Lowest detectable air concentration calculated assuming a 10-mL air sample with 2:1 split injection; for splitless injections, LOD would be 2.5-3× lower than shown; acronyms for the MPNs are defined in the text. [e] Not determined (interference). [f] No assigned TLV value.

2.4.7.4. PEMM-1 Calibrations and LODs. Prior to generating the calibration curves, the throughput of a 10-VOC mixture was determined by bypassing the μCR array and connecting the output of the second μcolumn to an FID via a heated transfer line. A 10-mL

sample of the mixture (100 ppm each in a Flex-foil bag) was sampled and analyzed in triplicate with and without the pre-trap installed. The results were also compared with those obtained from the bench scale GC-FID for samples drawn from the same test atmosphere but with sample-loop injection.

For benzene through C_{12}, a <3% reduction in avg peak area was observed with the pre-trap installed. For C_{13}, a 72% reduction in peak area was noted with the pre-trap, indicating substantial retention of this low-volatility interference per the pre-trap design. Yet, data from the reference GC-FID indicated some loss of C_{13} to surface adsorption in the flow path.

Calibrations were performed using a 2:1 split-flow injection setting over a 40-fold range of sample mass (i.e., from 0.1 to 4× TLV-TWA) on two subsets of compounds, i.e., those with TLVs of 0.5 to 20 ppm and those with TLVs of 25 to 400 ppm. Samples of 10 and 20 mL were drawn from each of three test atmospheres in bags to span the injection masses corresponding to these concentration ranges. The analysis proceeded as described above using the same temperature program as in all subsequent testing, and all compounds within a subset were fully resolved chromatographically.

Peak shapes differed significantly among VOCs and sensors, and tailing (i.e., peak asymmetry) generally increased with elution time. The peaks for 2-hexanone (MBK, compound 13 in Table 1.4), which had a mid-range retention time t_R of 63 sec, are shown in Figure 1.17 in order of increasing asymmetry. Sensors coated with HME, EOE, and C8 showed much less tailing than did TEG and OPH, and asymmetry factors ranged from 1.4 to 4.3. Data collected from one of the back-up sensors ruled out location along the flow path as a contributing factor to peak broadening. The trends with VOC elution time indicate that vapor sorption and desorption rates in/out of the MPN films contribute to both peak broadening and tailing, which is consistent with previous reports.

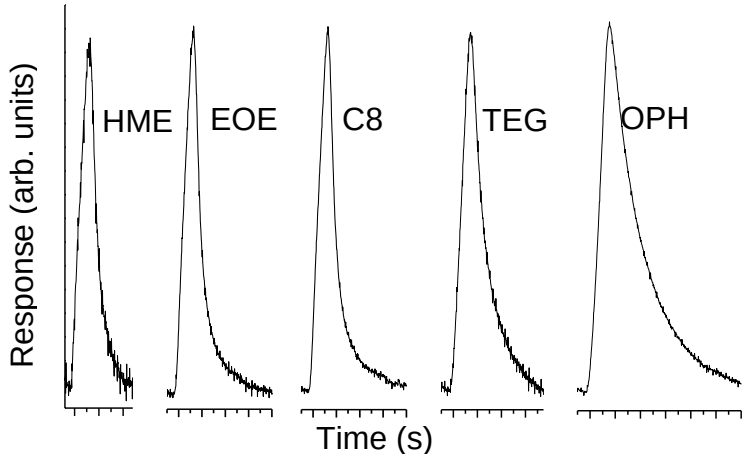

Figure 1.17. Range of peak shapes among the μCR sensors in the array for the representative compound 2-hexanone (MBK, compound 13 in Table 1.4, t_R = 67 s) from calibration test series. From left to right, the sensor and corresponding peak asymmetry factor (at 10% of peak max.) are listed as follows: HME, 1.4; EOE, 1.7; C8, 1.8; TEG, 2.3; and OPH, 4.3. Each small tick mark on the x-axis is 1 sec. Peaks have been scaled vertically to have similar heights such that the y-axis units are arbitrary.

Plotting of peak height versus sample mass yielded straight lines with linear regression R^2 values ≥0.99 (forced-zero y-intercept) for most VOC-sensor pairs and >0.98 for all pairs. The EOE sensor exhibited the highest sensitivity for most VOCs due apparently to its amphiphilicity and the accessibility and flexibility of the thiolate monolayers, which could enhance the rates of sorption and desorption of VOCs in the MPN film. The non-polar C8-coated sensor showed high sensitivity for aromatic and aliphatic hydrocarbons, as expected. Among the more polar VOCs,

the TEG-coated sensor was more sensitive than the OPH- and HME-coated sensors, particularly for ketones and butyl acetate. The generally low sensitivity exhibited by the OPH sensor can be attributed to the greater thickness of the MPN film compared with the others, since previous work with this material as a sensor coating resulted in peak widths similar to those with C8 and HME coatings. This would reduce VOC sorption-desorption rates and thus promote shorter, tailing peaks (see Figures 1.17 and 1.18).

The limits of detection (LOD) were estimated from the slopes of the regression models (peak height vs. injected mass) of each sensor from the equation 3σ/slope, where σ is the RMS baseline noise level from each sensor. Because a 2:1 split injection was used, for the purpose of deriving LODs in terms of air concentrations for a given sample volume, it was necessary to divide the slope by a factor of 3 to account for the loss of 2/3 of the captured mass. Assuming a 10-mL air sample, the LODs range from 0.1 ppm for TCB with the EOE sensor to 36 ppm for C_{12} with the OPH sensor (Table 1.4). The LODs for a given VOC generally differ by <5-fold among the sensors in the array, with the notable exceptions of the alkanes, for which the range is higher due to low sensitivity from the polar sensor films.

Importantly, our decision to use 2:1 split injections gave priority to chromatographic resolution over sensitivity and resulted in a loss in sensitivity of ~3-fold (somewhat less for early-eluting compounds that benefit from peak compression at the higher desorption flow rate). Thus, for splitless injections, the sensitivity should increase ~2.5-3-fold, and the LODs should decrease proportionally from the values listed in Table 1. Assuming that splitless injections are used and further assuming that detectable signals from only 4 of 5 sensors are required for vapor recognition (OPH sensor omitted, *vide infra*), all compounds could be detected and recognized well below their TLV-STEL values, all but benzene could be detected and recognized well below their TLV-TWA values, and all but benzene, MIBK, and MBK could be detected and recognized at or below 0.1×TLV.

2.4.7.5. PEMM-1 Response Stability and Autonomous Operation. Table 1.5 presents the RSDs around the average values of peak area obtained for 9 selected compounds from the C8- and OPH-coated MPN sensors each day for 7 consecutive days on the basis of 4 analyses per day (note: RSD values for peak heights were very similar to those for peak area with the exceptions of those of the last three compounds for the OPH-coated sensor, where the peak height variability was consistently a few % higher, undoubtedly due to the broadness of the peaks). The RSD values for the other sensors fell within the ranges spanned by these two sensors, with a few exceptions for the TEG-coated sensor. For the C8 sensor, the intra-day RSDs ranged from 1.0 to 8.0% among the VOCs, and the OPH sensor RSDs were generally higher and ranged from 0.8 to 9.9%. Later-eluting compounds generally gave higher values, but no trend over time was noted in any case. The greater variability observed for the OPH (and TEG) sensors is consistent with responses that are more highly dependent on sorption/desorption rates and are therefore more sensitive to small flow rate fluctuations. The corresponding RSDs for t_R values were <1.2% for all compounds except for the earliest eluting C_7 (RSD <3.6%).

Also shown in Table 1.5 are the inter-day RSD values calculated from the 7 daily average peak area values. For reference, the RSD values are given for the peak areas from separate analyses of the same test atmosphere performed with a bench-scale GC-FID (loop injection, 1 sample per day). As shown, the PEMM-1 peak area measurements showed excellent stability/reproducibility, with RSD values consistently higher than but comparable to those from the GC-FID for all compounds (i.e., 2.7-9.6% and 1.3-7.5%, respectively). The values of t_R and *fwhm* were similarly stable .

The PEMM-1 prototype was then operated continuously and autonomously for 8 hr on each of two consecutive days (i.e., 8 min/cycle, 60 cycles/day). For this series, the 6-VOC mixture was analyzed in triplicate at the outset, 54 blank analyses were performed, and the

same mixture was re-analyzed in triplicate at the end of the day. The t_R values and sensitivities were notably stable, decreasing only slightly over the course of each day, which we attribute to small increases in flow rate and/or baseline temperature. More specifically, t_R values decreased by <1.6%, and peak heights and peak areas decreased by ≤9.8 % (typically <6%) over the course of 8 hr. Although the average values of these variables were lower on the second day than on the first, differences were again small and sufficiently stable for any practical application.

Table 1.5. Medium-term stability of PEMM-1 analyses as indicated by the RSD of the avg peak area from the least (C8) and most (OPH) variable sensors for a subset mixture of 9 VOCs analyzed 4 times/day for 7 days.[a]

Cmpd	μCR	RSD (%) of Peak Area[b]								
		Intra-day (n = 4)							Inter-day (n = 7)	
		1	2	3	4	5	6	7	PEMM-1	GC-FID
C_7	C8	1.6	2.1	2.4	2.4	2.4	1.1	1.6	3.9	1.9
	OPH	4.1	3.1	4.7	7.3	6.6	3.4	3.0	4.1	
BAC	C8	1.3	2.4	2.1	1.5	3.7	2.9	2.0	2.9	1.3
	OPH	0.8	2.0	1.2	1.4	1.4	2.6	1.5	4.1	
XYL	C8	2.4	3.1	1.8	3.6	4.4	3.0	1.0	2.7	2.2
	OPH	2.2	3.5	3.6	5.0	2.1	4.0	2.8	5.7	
EBK	C8	2.4	4.1	3.5	3.5	3.5	4.2	4.7	4.9	4.6
	OPH	2.3	3.2	1.9	2.4	1.6	3.0	3.5	5.0	
PPB	C8	2.7	3.2	3.4	1.9	4.8	3.2	2.0	5.2	4.3
	OPH	3.0	5.9	4.1	5.1	5.7	7.9	4.0	6.9	
TMB	C8	2.7	3.0	2.8	3.3	2.4	5.9	2.3	6.8	5.3
	OPH	6.3	6.6	9.8	5.4	7.3	7.3	5.1	9.9	
C_{10}	C8	2.3	1.3	1.6	3.7	4.2	4.8	4.4	5.3	4.4
	OPH	6.2	2.3	1.7	5.0	2.0	7.5	6.6	5.7	
C_{11}	C8	4.5	4.2	5.8	3.6	4.5	5.8	3.8	9.0	6.0
	OPH	8.5	9.8	8.5	8.5	5.1	6.2	6.7	11	
C_{12}	C8	4.6	7.4	8.0	4.2	5.8	7.0	5.4	9.6	7.5
	OPH	9.1	7.8	9.9	9.7	6.3	7.6	9.3	13	

[a] *Intra-day RSD is based on 4 samples of the same static test atmosphere containing 9 VOCs at 2×TLV concentrations (see Table 1.4) analyzed approximately every other hour over a single day; inter-day RSD is based on the daily average peak areas.*
[b] *PEMM-1 analytical conditions: 10-mL air sample, 2:1 split injection (3 mL/min analytical path flow rate), and the same temperature program as used in calibrations; reference GC-FID data (1 sample per day) were obtained from the same test atmosphere using 100-μL loop injections.*

2.4.7.6. PEMM-1 24-VOC Analysis with Vapor Recognition. Figure 1.18 shows a set of 24-VOC chromatograms generated from the reference GC-FID (Figure 1.18a) and the five μCR sensors of the PEMM-1 prototype (Figure 1.18b) for a test atmosphere containing a mixture of these compounds at ~100 ppm each (500 ppm for acetone). The separation required only 3 min with PEMM 1. Although the retention order was the same, the specific retention times differed between the reference GC-FID and PEMM 1 traces due to differences in linear velocities. The lower overall resolution for the PEMM 1 traces relative to the GC-FID can be attributed to a combination of lower μcolumn separation efficiency and longer sensor response times. Consistent with Figure 1.17, the C8, EOE, and HME sensors gave relatively sharp peaks. Values of *fwhm* were <2.7 sec in all cases and ≤1.5 sec for the early-eluting target compounds 8-13. With the TEG and OPH sensors, the peaks were broader and more asymmetric, and *fwhm* values were 4.0 sec for C_{12} and <2.5 for compounds 8-13.

The first (broad) peak in each PEMM-1 trace was water vapor presumably present at trace levels in the liquid samples from which the test atmosphere was generated. Peaks 1-7, most of which co-elute, were from the interferences, which were well resolved from the first target compound of benzene (peak 8). The separation of the 17 target mixture components with the PEMM-1 was excellent with the EOE, C8, and HME sensors (R_s >1.5), somewhat less good with TEG, and rather poor with the OPH sensor. The observed increases in peak width with increasing elution time were expected and were also observed in the GC-FID trace. Notwithstanding the OPH sensor, the excessive tailing of which renders it of less value as a detector, the speed and resolution obtained were quite good. Taken together with the peak capacities, which ranged from 80-103 among the sensors for a 4-min separation based on MBK, and the peak production rates, which ranged from 20-25/min (also based on MBK), the chromatographic performance of the PEMM-1 exceeds that of other reported GC prototypes employing microfabricated separation components.

The normalized response pattern for each compound was obtained by dividing the calibrated slope (i.e., sensitivity) from each sensor by the slope from the sensor that gave the highest sensitivity in the μCR array for that compound. The patterns for all compounds are not shown, for brevity, but those for the four partially co-eluting target VOC pairs in Figure 1.18b are shown above the set of chromatograms. The ability to differentiate individual VOCs was assessed via Monte Carlo (MC) simulations coupled with extended disjoint principal components regression (EDPCR) classification models. This technique yields statistical estimates of single-vapor recognition rates (RR,%) based on the actual response variabilities and calibrated sensitivities.

The resulting confusion matrix for all 17 target compounds obtained using the responses from all 5 sensors in the array shows that 8 of the 17 targets could be recognized with <10% error based on their response patterns alone if they were chromatographically resolved from other compounds. Even for the other 9 compounds with lower RR values, the use of t_R values together with the response patterns could lead to unequivocal confirmation of their identities by reference to a calibration library. Removing the OPH sensor and re-running the MC-EDPCR analysis with the remaining 4 sensors resulted in relatively little change in RR values for most VOCs (with certain exceptions) and no net loss in the effective vapor recognition capability. Regardless of the number of sensors used, it was not possible to differentiate m-xylene (XYL) from ethylbenzene (ETB) at a high rate based on their response patterns. The n-alkanes were also difficult to differentiate, as were 3-heptanone (EBK) and butyl acetate (BAC). Fortunately, homologous n-alkanes are always well resolved chromatographically, as were EBK and BAC (due to large differences in p_v values).

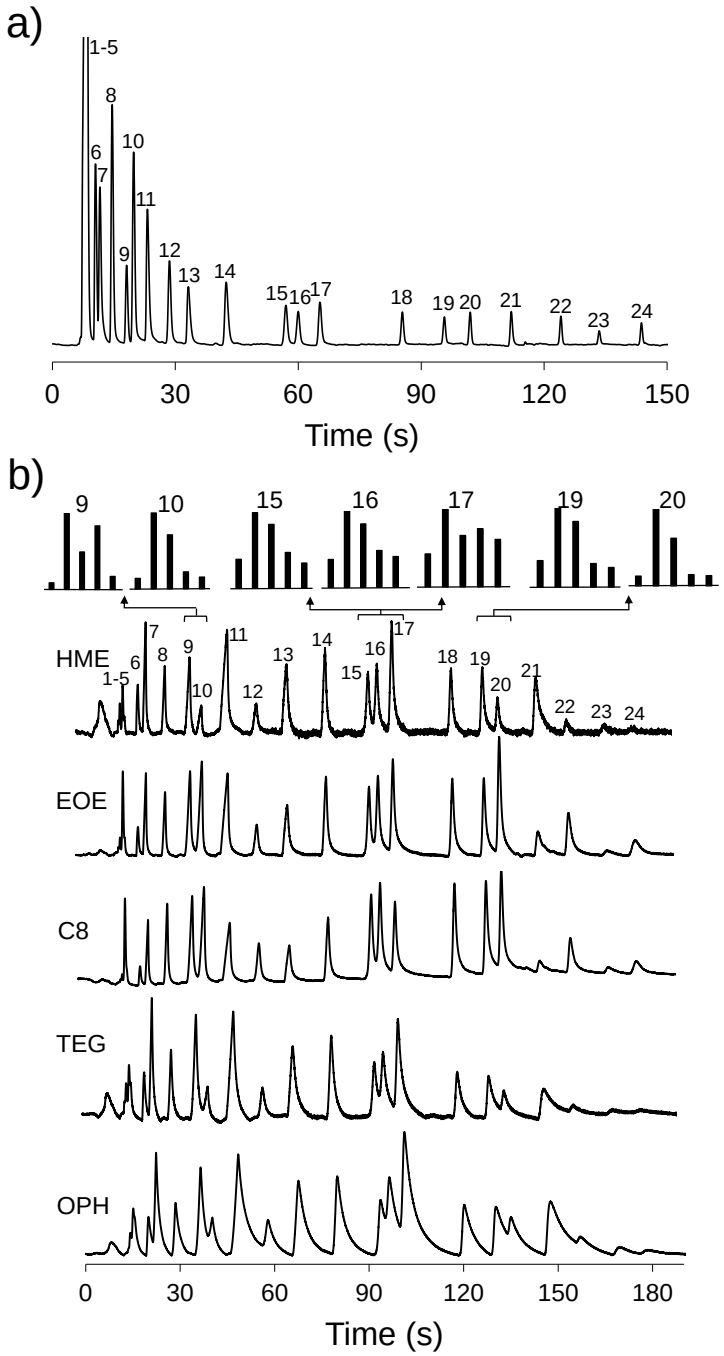

Figure 1.18: a) Reference GC-FID chromatogram of the 24-VOC mixture. Conditions: 6-m capillary column (PDMS); He carrier gas; 50 μL loop injection; and each vapor at ~100 ppm except for acetone (500 ppm) in a Flex-foil bag in N_2. b) Corresponding PEMM-1 chromatograms from the 5 μCR sensors. Conditions: 1-min sample at 5 mL/min; 60 sec desorption at 225 °C; 2:1 split injection (3 mL/min for analysis); He carrier gas; μcolumns at 28 °C for 0.5 min, followed by 10 °C/min to 33 °C then 50 °C/min to 125 °C, then hold; and μCR array at 30 °C. See Table 1.5 for peak assignments and text for sensor acronym definitions. Normalized response patterns (pk. ht.) shown for 7 vapors (order, l-to-r: HME/EOE/C8/TEG/OPH).

For those pairs of peaks that were not fully resolved with all sensors (i.e., those for which patterns were included in Figure 1.18b), MC-EDPCR analyses were run on each binary mixture to assess the capability for local discrimination. To simplify the analysis, the peaks from each pair were assumed to completely overlap. The RR values were ≥95% for TCE+C7, TMB+C10, and XYL+EBK. Only the XYL+ETB pair (RR = 77%) could not be effectively differentiated from its individual component compounds. This exceptional case notwithstanding, it is clear that this feature of the PEMM-1 prototype significantly enhances its analytical power.

2.4.7.7. Conclusions about PEMM 1. We have demonstrated that the PEMM-1 prototype μGC described in this work is capable of direct, autonomous, multi-VOC determinations at concentrations relevant to workplace applications. The speed, reliability, selectivity, limits of detection, dynamic ranges, low operating power, and types of VOCs amenable to accurate detection and recognition render the PEMM-1 an effective new addition to the repertoire of quantitative exposure assessment tools available to occupational health scientists. Reconciling the tradeoffs among VOC mixture pre-selection, pre-concentration, separation, and recognition/detection functions was central to realizing effective system-level performance. Collectively, the operational features and performance characteristics of the PEMM-1 prototype demonstrated in this study exceed those demonstrated with other prototype μGCs reported to date. Future work on optimizing sensor coating strategies should yield improvements in peak shapes and reductions in LODs. The results obtained from this study have been used to inform the design of a battery-powered, wearable prototype (PEMM-2). The results from that effort will be the subject of a forthcoming article.

2.5 Phase 2/Aim 2

2.5.1. Introduction to Phase 2/Aim 2

Phase 2 addressed **Aim 2** and entailed modeling, re-designing, fabricating, mounting, and characterizing a set of "Gen-2" micro preconcentrator/focusers (µPCF) and microcolumns for more power-efficient heating than Gen-1 predecessors, and to test their performance individually and in subsystems. The primary objective was to realize lower power dissipation, commensurate with 8-hr battery operation. Modeling was used to guide designs of devices that were subsequently fabricated. Additional modeling of the microcolumn was performed to demonstrate how the energy savings could be realized by using zone heating. Thus, our modeling served to guide the details of device design, construction, and operation. Additional performance testing was performed in the PEMM 1 and PEMM 2 prototypes described in other sections of this report. Also reported in this section are the fabrication of the new sensor arrays used in the PEMM 2 prototype.

2.5.2. Computer Modeling and Simulations for Designs of Gen-2 µPCF and µColumn

Initially, SolidWorks and COMSOL were used for the design and simulation purposes, respectively. 3D designs of the micro components were first developed in SolidWorks and then imported to COMSOL, a Finite Element Solver, to perform multi-physics simulations covering both the electrical and the thermal domains to predict the performance. An exhaustive analysis of the microcolumns and µPCF was performed. The simulations account for heating of microcomponents due to Joule effect, heat losses from the surface of the chip due to natural convection, thermal losses due to printed circuit board (PCB) contact, and finally cool down phases. Mesh sizes for simulations were in the range of 40,000-50,000 elements for a tetragonal meshing type.

2.5.2.1. Design of the Gen-2 µPCF. The most distinctive change in the µPCF for Gen-2 is the use of efficient heaters. Gen-1 µPCF were bulk heated, a method in which a high potential difference was established across two platinum terminals and the current would flow through the bulk of the device, and thus heating up in the process. However, bulk heating is inefficient method of heating because of the high thermal gradients it creates and because it needs a very high voltage to achieve the required temperature ramps. The efficiency and achievable heating rate of the µPCF was increased by switching from bulk heating to thin-film resistive heaters.

The characteristics of the µPCF are described below. Figure. 2.1 depicts a 3D view of the Gen-2 µPCF. The dimensions of the cavity region are the same as Gen-1. A Pyrex layer (~100 um) forms the lid for the cavity and is followed by a Si region of 500 um thickness. The cavity region is etched into the silicon to a depth of 400 um and the open surface faces the Pyrex lid. Tapered edges of the cavity at the entry and exit ensure uniform distribution of air flow in the cavity. The heater profile shown in Figure 2.1b assumes an Al-metal heater of 300 nm thickness. The heater profile has been optimized to reduce thermal gradients by designing the heater with sub branches of different resistances in parallel, with three such branches connected in series. This ensures identical current flow in each branch and eventually results in uniform heating.

The thermal gradient, or the temperature difference between the hottest and the coldest spot in the cavity predicted for the new heater based µPCF, is 11^{o}C. This is a major improvement over the Gen-1 µPCF which has a much higher gradient of 18^{o}C. The hold-phase power requirement has been estimated by identifying the voltage required to achieve a 225^{o}C temperature at steady state. From finite element simulations this value is 0.5 V, and the power requirement is measured to be 0.32W.

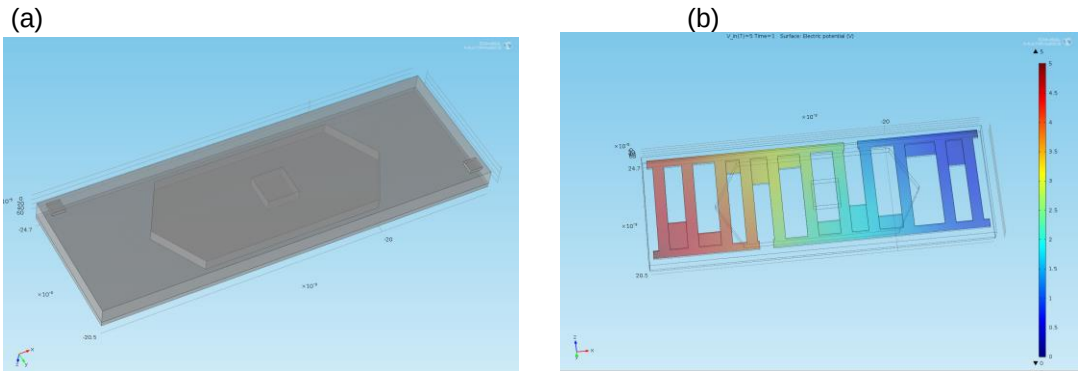

Figure 2.1. (a) Gen-1 µPCF design with a cavity region packed with Carbopack X. (b) Gen-2 microsampler heater design. The dark red edge represents the source terminal while the dark blue edge represents the ground terminal. The colors represent the gradient of the electrical potential.

We initially advocated the use of Al micro heaters in order to reduce the voltage requirement. However, we discovered that Al-based micro-heaters were susceptible to premature failure due to electromigration, forcing the shift to Pt. The lower resistance of the Al heaters allowed large current flow rates wherein the electrons acquired momentum sufficient to displace atoms of the material. This resulted in non-uniform and unpredictable metal displacement in the form of hillocks, where material accumulated, and voids from where metal was displaced. The heaters subsequently failed due to an open circuit caused by the voids.

Additional issue of heater resistance increase due to aluminum oxidation has been a contributing factor guiding the material change. Oxidation of Al is a natural phenomenon and occurs even at ambient temperatures and is further accelerated at higher temperatures. The increase in Al resistance directly corresponds to higher joule heating and higher voltage requirement compared to initial specification. From an energy budget perspective, the new devices have identically the same energy consumption with the Pt. heaters albeit at a higher voltage and smaller current compared to the Al. based design. The increased voltage demand was tackled by acquiring a battery with a higher voltage rating. Figure 2.2 shows an image of the device with the initial cavity size. This was later extended but the basic design was retained.

Our simulation predicted the heating profiles, energy consumption, and thermal gradients of the new µPCF design. The µPCF was predicted to exhibit superior performance both electrically and thermally compared to the previous generation devices. Application of 12 V to the 7.7Ω micro-heater would result in a temperature ramp of 410ºC/sec with the C-X cavity temperature reaching nearly 380ºC/sec. While the predicted power requirement was 18.69 W, marginally higher than the Gen-1 µPCF, reduction of device voltage requirement proved to be beneficial due to the elimination of step up circuits that were necessary for operation. Application of 12 V to the 7.7Ω micro-heater for nearly 0.6 seconds is predicted to heat the cavity bed to 240ºC. The simulated thermal gradients across the Pt-heater device are < 8ºC.

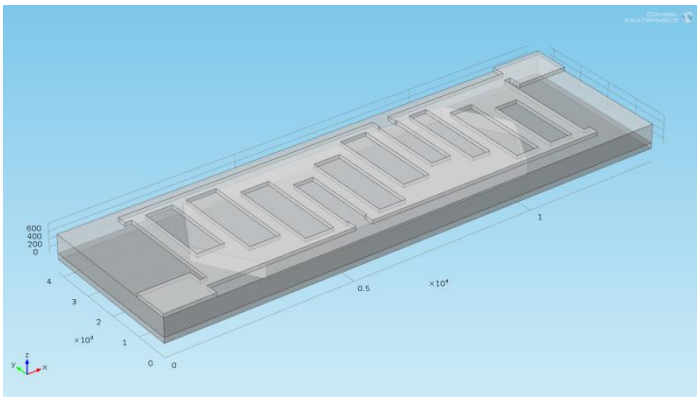

Figure 2.2. A CAD model of the 300 nm thick micro Pt-based microheater with larger contact pads deposited atop the μPCF.

2.5.2.2. Design of the Gen-2 (Segmented, Zone-Heated) Microcolumn. The concept diagram of the channel configuration of the new microcolumn is shown in Figure 2.3a. The Gen-2 microcolumn houses three 2-m long spiral segments of a single channel. Such an etched channel in a monolithic integration obviates the need for externally connected capillaries, thus minimizing dead volume and improving device performance and resolution. However, monolithic integration of the micro-columns introduces large amounts of thermal cross talk which needs to be mitigated to prevent co-elution of analytes within the micro-column, as well as thermal gradients due to added mass and larger thermal footprint.

To address the issue of thermal crosstalk, we proposed to etch silicon at multiple locations using DRIE to create fin structures with air pockets between them. These 500μm tall and 30 μm wide fin structures enclosed each individual 2-m spiral segment except at locations for interconnect channel sections allowing for superior thermal isolation. The fin structures were predicted to essentially inhibit in-plane thermal conduction and enhance out-of-plane thermal convection. Optimal thermal design of the fins was achieved using both analytical methods and FEA tools.

Simulations accounted for Joule heating of the μcolumn segments and convective, radiative, and conductive heat losses. Several different slot and fin configurations were assessed, and the final configurations included tradeoffs related to fabrication, such as pattern fidelity and mechanical strength. Details have been omitted for brevity. For the final heater design, simulations indicated that the microcolumn would have thermal gradients of only ~ 1 ^{o}C across all segments when all three segments were heated to as high as 180 °C and only ~ 6 ^{o}C when heated individually.

The pitch, cross section, length, and spiral patterns of the channel mimic those of the early μcolumns reported in the literature and developed by our group. The chamfered-square spiral pattern (apparent in the micrograph in Fig. 2.3b, but not in Fig. 2.3a) offers a tighter packing than a circular-spiral or serpentine channel layout, and thus a smaller thermal mass. Chamfering the corners reduces turbulence and, thus, band dispersion.

The thermal isolation structures (Fig. 2.3e) consist of slots etched through the substrate with fins extending lengthwise within each slot to increase surface area for dissipating heat convectively to the ambient while reducing in-plane heat conduction. These are similar to those reported by Manginell, et al. for thermally isolating their μcolumn from a μsensor integrated on the same Si substrate. The meander-line heater dimensions were designed to minimize temperature gradients across a segment while also minimizing power dissipation. Fluidic inlet

and outlet ports are located on one edge of the chip, opposite that where the heater bonding pads are located, to facilitate integration into the PEMM prototype.

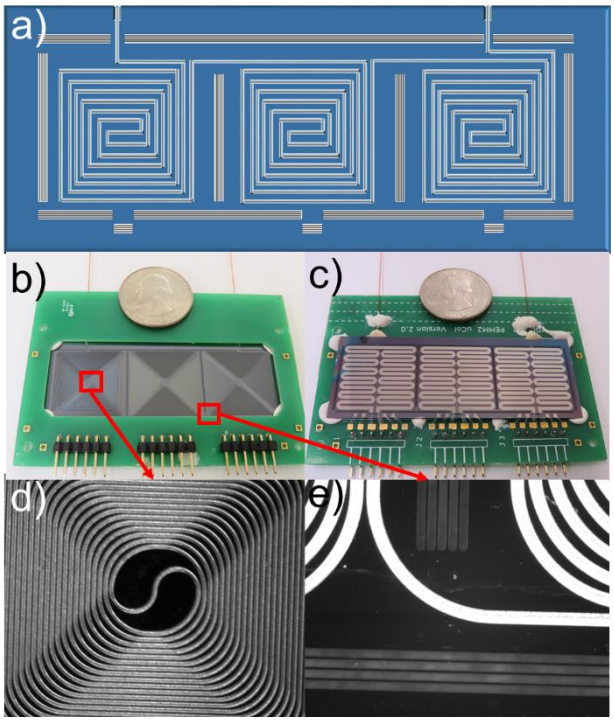

Figure 2.3. a) concept diagram of the segmented µcolumn; b) top-side view and c) bottom-side view of the µcolumn mounted on its printed circuit (carrier)board, with the channel visible from the top side and heater patterns visible from the bottom; d) enlargement of the center of the spiral of one µcolumn segment; e) enlargement of the slot/fin thermal isolation structures.

2.5.2.3. Fabrication of the Gen-2 Segmented Microcolumns. The µcolumns were fabricated from 0.5-mm thick, 100-mm diameter, <100> double-side polished Si wafers (University Wafer, Boston, MA). The main steps of the process are summarized in Figure 2.4. First, a 1.5-µm thick layer of thermal SiO2 was grown on both sides of the wafer. Then, the µcolumn channel (150 µm wide, 50 µm wall within spiral area), thermal isolation slots (600 µm wide) and fins (50 or 80 µm wide, spaced by 80 µm gaps) and expansion sections at the inlet and outlet of the channel (430 µm wide, 1950 µm deep) were defined photolithographically and the SiO2 layer was reactive-ion-etched (RIE) to form a hard mask on the substrate (note: horizontal thermal-isolation slots have 3 fins, vertical slots have 4 fins, and the vertical fins at the outer edges of the chip are 80 µm wide while those between segments are 50 µm wide). A new layer of photoresist was then used to selectively pattern the fluidic expansion ports and slot struts on the front side, and deep reactive ion etching (DRIE) was used to etch these regions of the Si substrate to depth of 140 µm. The photoresist was then stripped and, using the initial SiO2 hard mask, DRIE was used to create the µcolumn channel and to continue to etch the fins and inlets. DRIE was concluded once the µcolumns and inlets reached depths of 250 and 400 µm, respectively.

Next, the front-side oxide mask was selectively stripped with buffered HF, and then a 0.2-mm thick, 100-mm diameter Pyrex wafer was anodically bonded to the front side of the wafer, sealing the µchannel. Ti/Pt (30/360 nm) was then patterned on the backside using e-

beam evaporation and liftoff to generate the heaters, resistive temperature devices (RTD), and dice lines. The fin structures were then patterned on the backside of the Si wafer and, after removing the oxide by RIE, DRIE was used to complete the thermal isolation slots and fins. Etched feature dimensions were confirmed throughout the fabrication process using a 3-D optical profiler (NewView 5000, Zygo, Middlefield, CT). Finally, the wafer was diced into µcolumns, and water and air were used to clean out dicing debris. Sections of deactivated fused-silica capillary (250 µm i.d.,) were inserted into the inlet and outlet ports and sealed with epoxy (Hysol 1C, Rocky Hill, CT).

The µcolumn was then statically coated with PDMS from a solution (4.38 mg/mL, methylene chloride/n-pentane, v/v = 1) that contained dicumyl peroxide (1% w/w of PDMS) as curing agent according to reported methods. Briefly, the solution was drawn through the µcolumn until the entire volume was filled. Then, one end was sealed with a septum, the µcolumn chip was placed in a water bath (30 °C) and gentle suction was applied to the other end to evaporate the solvent. The µcolumn was heated to 180 °C under N_2 atmosphere in a GC oven to cross link PDMS. On the basis of the internal surface area of the channel and the concentration of PDMS used, the average thickness of PDMS coated on the channel wall was 0.20 µm. The sections of interconnecting capillary, which were also coated and crosslinked, were cut to 4 cm.

The µcolumn was then affixed with a minimum of epoxy at each corner onto a printed circuit board (PCB) that had a slightly smaller rectangular hole cut out beneath the µcolumn chip, and the bonding pads for the heaters and RTDs were wire-bonded to the corresponding pads on the PCB. Additional epoxy was used to mechanically anchor the capillaries to the PCB. During testing the PCB was suspended by clips on a clamp-stand fixture.

Photos of the new microcolumn are shown in Figure 2.3 as well as in Figure 2.5. Golay plots run with one of the new microcolumns gave excellent results (Figure 2.6 below).

The Golay plot (Figure 2.6) was obtained after coating but before stationary phase cross-linking. The quality of the 3 2m-µcolumns was evaluated with both N_2 and He carrier gas. The minimum of plate heights (H_{min}) of the µcolumn were 0.024 cm and 0.026 cm for N_2 and He, respectively. The maximum number of plates (N_{max}) for the µcolumn was 4,161 plates/m at N_2 optimum velocity ($\bar{u}_{opt}$) of 11 cm/s and 3,856 plates/m at He optimum velocity ($\bar{u}_{opt}$) of 34 cm/s. These are excellent results.

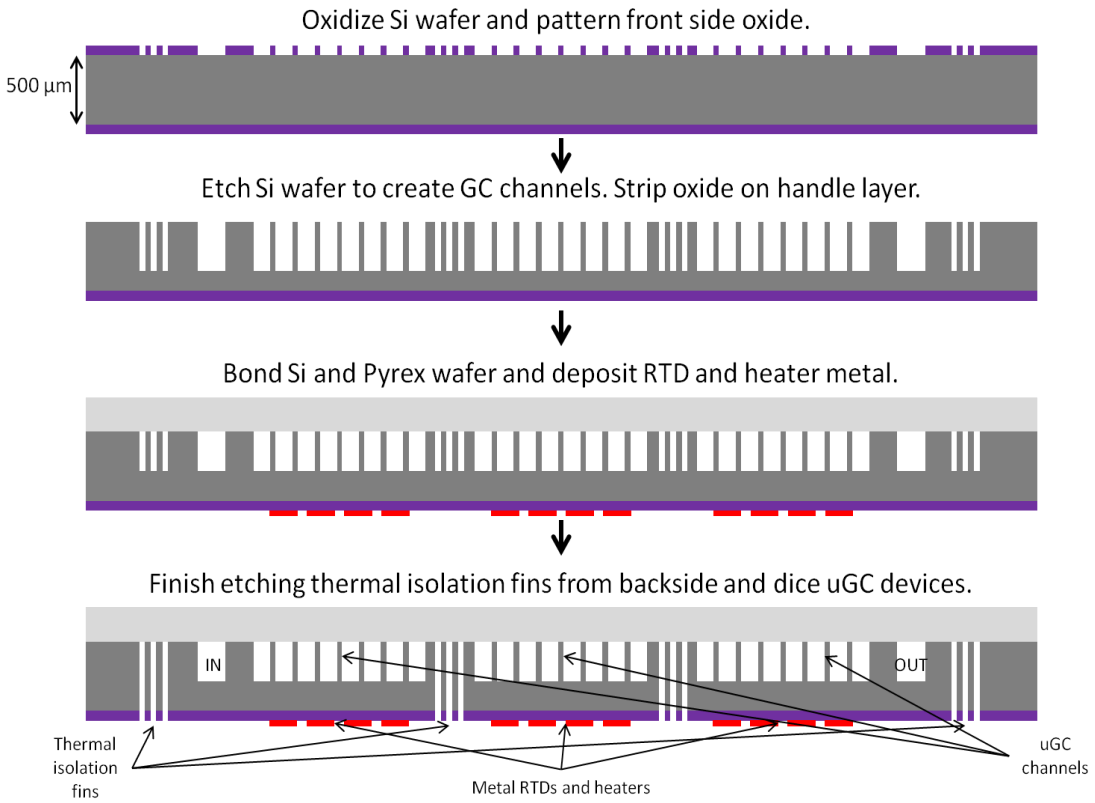

Figure 2.4. Side view schematics showing the new fabrication process developed for Gen-2 monolithic microcolumn device.

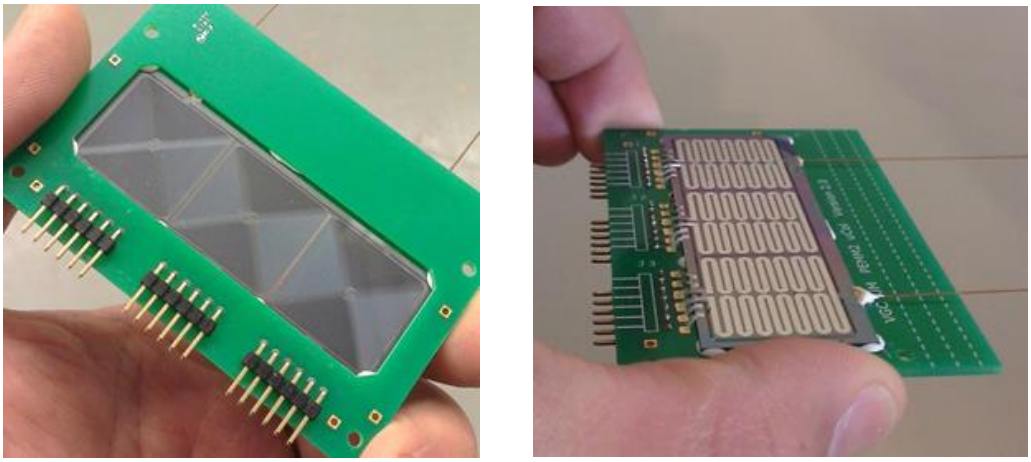

Figure 2.5. Gen-2 6-m segmented microcolumn mounted on a PCB. Left: topside with meander line heater showing; right: underside with the etched channel comprising the separation column showing.

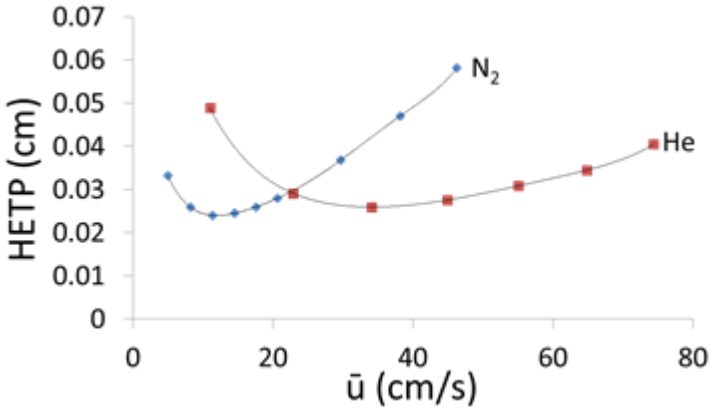

Figure 2.6. A Golay plot of segmented microcolumn coated with 0.2 µm thick PDMS. Conditions: n-octane probe; 5 µL saturated headspace injection;30 °C GC oven; 250 °C inlet injection and FID detection.

2.5.3. Performance Modeling and Implementation of Zone-Heated Microcolumns

This section of the report concerns the performance modeling and experimental implementation of the monolithic segmented, zone-heated microcolumn, with an emphasis on demonstrating energy efficiency. Although a thorough description of the methodology and results is provided here, additional details can be found in our publication on this topic:

Z3. Lin Z, Nuñovero N, Wang J, Nidetz R, Buggaveeti S, Kurabayashi K, Zellers ET: [2018] A Zone-Heated Gas Chromatographic Microcolumn: Energy Efficiency. Sensors and Actuators B: Chemical 254: 561–572.

As described above, the monolithic µcolumn chip measures 7.1 × 2.7 × 0.075 cm and contains a 6-m long, 250 × 140 µm deep-reactive-ion-etched Si channel with a Pyrex cap, wall-coated with a cross-linked polydimethylsiloxane (PDMS) stationary phase. Along the channel are three serial 2-m long spiral segments, each with an independent integrated resistive heater and thermal isolation features etched in the substrate. By turning the segment heaters on and off at strategic points during a separation, significant energy savings could be realized relative to heating the entire chip simultaneously (i.e., globally), with no loss in chromatographic resolution. A classical lumped element model was used as the basis for simulations of energy consumption, and a published band trajectory model was used to estimate analyte residence times in each segment.

Four simple mixtures of volatile organic chemicals were used to evaluate the models and assess the energy consumed for zone heating and global heating under isothermal and temperature-ramped conditions. Results indicate that reductions in the required energy per analysis using zone (vs. global) heating ranged from 14 to 31% among the cases considered, depending on the heating profile (i.e., isothermal or ramped), heating schedule, and the retention times of the analytes in the mixture. Modeled energy reductions tended to underestimate experimental reductions, but differed by <2% in all cases considered. This approach to µcolumn design and operation shows promise for extending battery life in wearable µGC instrumentation.

2.5.3.1. Introduction to Band Trajectory Model (BTM) & Thermal Model. Implementation of the zone heating approach to μcolumn design and operation requires knowledge of the locations of eluting compounds along the channel, and thus in each segment, over the course of a separation. Toward this end, we adapted the BTM reported by McGuigan and Sacks original developed for use in dual-column, pressure-tuned ensembles. The key expression from the model is given in Eq. 1:

$$t_{x'} = \sum_0^{x'} \frac{64\eta \cdot \Delta x \cdot (k-1)\sqrt{P_{i/o}^2 - (x/L)\left(P_{i/o}^2 - 1\right)}}{d^2 p_0 (P_{i/o}^2 - 1)} \quad (1)$$

where $t_{x'}$ is the total time required for an analyte band to migrate a distance, x' (= $x + \Delta x$), along the length, L, of the μcolumn, d is the effective inner diameter of the μcolumn, p_0 is the outlet pressure, $P_{i/o}$ is the inlet:outlet pressure ratio, η is the temperature-dependent viscosity of the carrier gas, and k is the temperature-dependent retention factor of the analyte. By dividing L into a series of incremental length intervals, Δx, Eq. 1 allows the trajectory of each analyte to be mapped over time. Values of η are available in the literature, and k can be determined empirically. A plot of time vs. distance gives the segment-specific retention times, t_R, needed to effectively implement the zone heating technique.

Assuming uniform temperature within each segment, the heating of the segments of the μcolumn can be represented by a classical lumped capacitance model, the equivalent circuit of which is given in Figure. 2.7, which considers three adjacent μcolumn segments, each with a heat capacity, C_i, thermal resistance, R_i, and source of power, P_i, that is capable of generating a certain rate of heat flow, dQ/dt, to the segment. The resistance to heat transfer between segments is R_c and the additional power required to compensate for such inter-segment heat transfer (i.e., thermal cross-talk) can be expressed simply as P_{ci}. According to this model, the power required to create a temperature difference above ambient, θ_i, is given by:

$$P_i = \frac{dQ}{dt} = C_i \frac{d\theta_i}{dt} + \frac{\theta_i}{R_i} + P_{ci} \quad (2)$$

where each R_i would be measured experimentally and therefore would implicitly account for convective heat transfer to the surroundings.

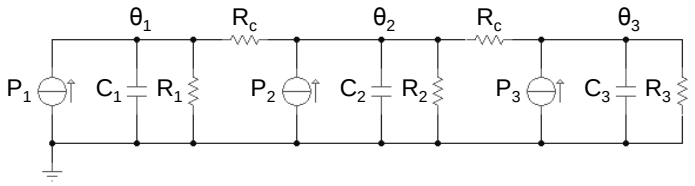

Figure 2.7. Thermal model of the segmented μcolumn for zone heating energy analysis.

The energy, E_{ij}, consumed to raise the segment to a specified set-point temperature, θ_s, and maintain it there for some time period, t_j, as in an isothermal separation, can be expressed as

$$E_{ij} = \int_0^{t_j} P_i dt = C_i \theta_s + \frac{\theta_s}{R_i} t_j + E_{cij} \quad (3)$$

where E_{cij} accounts for the energy lost to the adjacent segments. If enough time elapses for steady-state conditions to be reached and maintained, then we can approximate E_{ij} as follows:

$$E_{ij} = P_i t_j = \left(\frac{\theta_s}{R_i} + \frac{\theta_c}{R_c}\right) t_j \quad (4)$$

where θ_c is the inter-segment temperature difference at steady state.

For the case of a linear temperature ramp, as is often employed in a temperature-programmed separation, θ_i, and therefore P_i, increase with time and the energy consumed can be expressed as

$$E_{ij} = C_i M t_j + \frac{M}{2R_i} {t_j}^2 + E_{cij} \quad (5)$$

where M is the temperature ramp rate. Since E_{ij} is a quadratic function of time and it also depends on C_i, a linear approximation like Eq. 4 no longer applies.

For the purpose of this analysis we next consider an isothermal separation and compare the total energy required to perform such a separation via zone heating of the individual segments, E_Z, to that required via "global" heating, E_G, where the three segments are heated simultaneously to achieve θ_s for the entire analysis time period, t_a. For the latter scenario, $\theta_c \approx 0$ (Eq. 4), and assuming, for simplicity, that $R_1 = R_2 = R_3$, then we can express the total energy as

$$E_G = 3\frac{\theta_s}{R} t_a \quad (6)$$

In the simplest zone heating scenario, there would be a sequence of three discrete time windows: t_1, when only segment 1 is heated; t_2 when only segment 2 is heated (segment 1 is turned off); and t_3 when only segment 3 is heated (segment 2 is turned off). The sum of these t_i values is t_a, and for the special case where $t_1=t_2=t_3$, the segment heating time is t_s. Regardless of the duration of each time window, if we consider the ideal situation where R_c is infinitely large, then the E_Z/E_G is 0.33 and the energy reduction from zone heating is 0.67 (i.e., 67%). This represents the maximum possible energy savings.

In fact, this simple case would rarely occur in practice because it requires that the analytes migrate in close proximity throughout the separation. Normally, there would be a larger range of migration rates and associated retention times (and residence times) such that some analytes would be present within all three segments for a significant portion of time. Acknowledging this, another isothermal scenario can be considered for which we designate five discrete time windows (t_1 - t_5), wherein heating of the first segment for t_1 would be followed sequentially by heating of the second and third segments for t_2 and t_3, respectively, all to the same θ_s. At the end of t_3, the first segment heating would be discontinued, and then at the end of t_4, the second segment heating would be discontinued. The last period (i.e., t_5) would extend to the point where the last compound elutes from the μcolumn, marking the end of the run, at $t = t_a$.

From Eq. 4 we can express E_Z as the sum of the energies consumed during each t_i, i.e.

$$E_z = \sum_{i=1}^{3} \sum_{j=1}^{5} E_{ij} \quad (7)$$

and for any isothermal scenario we expect the migration rates of the analytes to be nearly constant throughout the separation (*vida infra*), so that each analyte spends an equal amount of time in each 2-m segment. Since the schedule of segment heater turn-on and turn-off times is specified by the retention time of the analyte of highest volatility (t_h) and the retention time of the analyte of lowest volatility (t_a), respectively, we can express the time windows t_j in terms of those limiting values (i.e. $t_1 = t_2 = t_h/3$, $t_3 = t_a/3 - 2t_h/3$, *and* $t_4 = t_5 = t_a/3$). If we designate the range of analyte retention times spanned in a given analysis as $\Delta t_R = t_a - t_h$, then we can express the fractional reduction in energy attributable to zone (vs. global) heating, E_R (= $1 - E_Z/E_G$) as follows:

$$E_R = \left(1 - \frac{1}{3}\left(\frac{1}{1+Rc/R} + \frac{1}{(1+(1+Rc/R)^{-1})^{-1}+Rc/R}\right)\right)\left(\frac{2}{3} - \frac{\Delta t_R}{3t_a}\right) \quad (8)$$

Eq. 8 shows the two main factors that influence the attainable energy savings due to zone heating. The first term on the right-hand side (within large parentheses) accounts for inter-segment thermal isolation, expressed as the ratio R_c/R. When R_c/R is << 1 (i.e. poor isolation), this first term approaches zero and there would be little or no reduction in energy with zone heating. As R_c/R becomes larger, the term gradually approaches unity, and the energy reduction would be maximized with respect to this factor. Thus, the μcolumn should incorporate design features that increase R_c to the extent permitted by the physical constraints of the device structure and material properties.

The second term on the right-hand-side of Eq. 8 accounts for the fraction of the total separation time the segment heaters are off. As in the ideal scenario presented above, this term approaches its highest value of 2/3 when Δt_R (= $t_a - t_h$) is small, which would occur for a set of compounds with very similar retention times for which the three segment heaters could be switched on and off in succession (i.e. $t_s \approx t_a/3$). For a broader spectrum of compound retention times, Δt_R would be a larger fraction of t_a, the heating times of the segments would overlap, and E_R would decrease. This second term would approach its minimum value of 1/3 as Δt_R approaches t_a. However, even for modest values of t_h there would be delays in the turn-on of segment 2 and 3 heaters and commensurate savings of energy. In practice, the schedule of segment heating would be determined by the residence times of the mixture components in each segment, which could be accurately predicted by BTM (*vida supra*).

For the more complicated cases involving temperature programmed separations, account must be taken of the scheduling and durations of the different time windows, segment heating rates, minimum and maximum temperatures, and thermal capacitances, as well as the temperature dependence of thermal resistances, the use of PWM with feedback control, and the limited power available to actuate the heaters. Computer simulation was used to account for these factors using algorithms that allowed E_Z and E_G to be evaluated for any conceived heating scenario.

2.5.3.2. Experimental Methods for Microcolumn Characterization. All GC measurements were collected with a bench scale GC equipped with a flame ionization detector (FID) (Model 7890B, Agilent Technologies, Palo Alto, CA). The μcolumn was connected between the inlet and FID with sections of deactivated fused silica capillaries using press-fit connectors. GC injection port and detector temperatures were both 250 °C. For determinations of μcolumn efficiency the μcolumn temperature was controlled by the GC oven. For collecting *k* values used for BTM and for subsequent testing, the μcolumn temperature was controlled by the on-chip heaters.

For isothermal separations with global heating, all three heaters were turned on 35 s prior to the injection to allow all segments to come to the set-point temperature (note: this could have been done faster but there was need to do so for this set of tests). For temperature

ramped separations with global heating all segments were ramped at the same rate to the same temperature. For isothermal separations with zone heating, segment heaters were turned on and off in sequence as dictated by BTM for the subset under test. For comparisons of global and zone heating retention times, the rate of heating was between 41 and 55 °C/min and segments were heated sufficiently early to achieve the set-point temperature at the required time. For comparisons of power dissipation between global and zone heating, segments were heated at 200 °C/min. For temperature ramped separations with zone heating, segments 2 and 3 were rapidly preheated in sequence to bring the segments to the temperatures needed to maintain the temperature ramp rate for the experiment.

The separation efficiency of the µcolumn was determined at 30 °C (GC oven) using n-octane as the probe by serial injections (splitless) with an autosampler and gas-tight syringe of headspace vapor from a septum-sealed vial containing liquid n-octane to which methane was added from the house supply. The adjusted retention times ($t_R' = t_R - t_M$) and full width at half-maxima (*fwhm*) of eluting peaks were measured as a function of average N_2 carrier gas velocity, where the hold-up time, t_M, was taken as the methane retention time. The average velocity was calculated as L/t_M. The plate number, $N = 5.545(t_R'/fwhm)^2$, and plate height, $H = L/N$, were calculated.

Table 2.1. List of test compounds, subset assignments, and vapor pressures, p_v.

subset	# [a]	compound	p_v (kPa) [b]
high	1	trichloroethylene	6.25
	2	toluene	3.78
	3	2-hexanone	1.46
medium	4	n-octane	1.88
	5	ethylbenzene	1.27
	6	3-heptanone	0.187
low	7	n-nonane	0.59
	8	1,2,4-TMB	0.27
	9	n-decane	0.191
general	1	trichloroethylene	6.25
	4	n-octane	1.88
	9	n-decane	0.191

[a] refers to peak assignment in Figure 2.8. [b] at 25 °C

Table 2.1 lists the test compounds along with their corresponding vapor pressures, p_v. They have been grouped into four subsets based roughly on p_v ranges for the purposes of testing (described further below). The fourth subset in Table 2.1 consists of one member from each of the first three other categories, so as to span the range of p_v values of the entire set of compounds – this is referred to as the "general" subset. Values of k ($= t_R'/t_M$) for each compound were determined individually at each of five temperatures between 30 and 100 °C. Autosampler syringe injections of 0.1 µL liquid samples (~10 mg/mL in CS_2) were performed with a 20:1 split at an inlet pressure of 13.5 PSI using He as carrier gas. The same conditions were used for subsequent experiments.

For subsequent comparisons of zone vs. global heating, compounds were tested in the subsets shown in Table 2.1 under both isothermal and temperature-ramped conditions. The

three segment RTDs were calibrated in the GC oven. A custom LabVIEW program run from a desktop computer was used to heat each segment independently by use of a proportional-integral-derivative (PID) feedback loop between the voltage applied to each heater and the set-point temperature or temperature ramp. Pulse-width-modulated (PWM) voltages were applied to the heaters through solid-state relays at 4 Hz. Isothermal separations were performed in 10 °C increments from 50 to 100 °C. Temperature programmed separations were performed from a baseline temperature of 30 °C in 10 °C/min increments from 10 to 60 °C/min to a final temperature of 100 °C.

2.5.3.3. Band trajectory modeling. For BTM (via Eq. 1), values of log *k* were plotted against *1/T* and linear regression models fitted to the data were used to obtain *k* values at intermediate temperatures. ($r^2 > 0.998$ in all cases). Values of *P* were calculated as the ratio of p_i/p_o where p_o was atmospheric pressure and p_i was the sum of p_o and the applied pressure at the GC injection port (13.5 PSI, displayed on workstation readout). Values of η for the He carrier gas were obtained from the literature.

The μcolumn was divided into 2.5-mm intervals (Δx in Eq. 1). For accurate results it was necessary to account for the 4-cm long PDMS-coated capillary sections epoxied into the inlet and outlet of the chip, and the 23- and 33.5-cm long sections of deactivated interconnecting capillary extensions used, all of which were 250 μm i.d.. Note that the PDMS-coated-Si μcolumn was assumed to have an i.d., equivalent to a circular channel with an i.d. of 206 μm.

2.5.3.4. Energy Consumption Simulations. In order to estimate the energy savings for all the different heating scenarios, the model represented by Figure 2.7 was translated to a multiple-input/multiple-output (MIMO) dynamic system, with heating power values as inputs and segment temperatures as outputs, and simulated in a PID feedback loop using Matlab (version 8.5, MathWorks, Inc., Natick, MA). The scheme of the MIMO model used is given in ref. Z3. The temperature set-point profile directing each feedback loop was constructed on the basis of the time windows obtained for each case from the BTM analysis. The transfer function matrix of the system, containing the ratios of all the combinations θ_i and P_i, was obtained in Matlab by applying frequency-domain analysis to the μcolumn thermal model via a Laplace transform.

The transfer functions were evaluated using the thermal parameters C_i, R_i, and R_c, which were estimated experimentally. Each feedback loop was also provided with a saturation block to properly account for the limit of the power imposed by the supporting system; the PEMM system uses a 24-V power supply, which gives a maximum of 5 W for μcolumn heating and limits the ramp rate to ~200 °C/min. For switching the segment heaters from the off state to the desired temperature, faster heating rates for shorter time periods were found to consume less energy than slower rates for longer periods. This heating rate was standardized to 200 °C/min for all simulations and experiments related to energy consumption estimation. Furthermore, for this study, we placed a conservative limit of 100 °C on the maximum μcolumn temperature, such that the maximum θ_i would be 70 °C, since 30 °C is the baseline temperature. Under this constraint, separations were complete in < 161 s in all cases.

2.5.3.5. Power Measurements and Thermal Parameter Estimates. To demonstrate the zone heating programming and validate the thermal model for the energy estimations, discrete measurements of power were performed for isothermal and linear temperature-ramp separations. A 16-bit DAQ card (USB-6218 OEM, National Instruments, Austin, TX) was used to record the PWM voltage applied to each segment heater at a sampling rate of 250 Hz. The supplied current was measured from the voltage drop across a 1 Ω series resistor. The instantaneous power, P_i, was obtained by taking the product of the voltage and current waveforms. The energy consumption of a given separation experiment was calculated by integrating P_i over the total separation time (via Eq. 3 or 5).

To obtain the thermal parameters of the μcolumn, first C_i and R_i were estimated by placing all three segment heaters in controlled feedback loops and heating them at the same linear ramp rate, M = 10 °C/min, while temperature was simultaneously monitored. When the three temperatures are equal, θ_c/R_c approaches zero and C_i and R_i could be evaluated from the intercept and slope, respectively, of the linear portion of the power-time profile via Eq. 2 when P_{ci} = 0.

To estimate the inter-segment thermal resistance, R_c (Fig. 2.7), the μcolumn was placed in the GC oven at 30 °C and 1.2 W of power was applied only to the segment 2 heater. After several seconds, all segments came to steady-state temperatures, θ_s. Under these conditions the capacity term in Eq. 2 goes to zero and R_c could be evaluated from P_2, θ_s, θ_c and R_2, using Eq. 4, accounting for the (2×) crosstalk losses to both flanking segments.

Results and Discussion

2.5.3.6. Initial Characterization. From the measured power profiles of segments 1-3 (ref. Z3), the following values of heat capacity and thermal resistance were determined: $C_1 = C_3$ = 0.85 J/°C, C_2 = 0.68 J/°C, $R_1 = R_3$ = 42 °C/W and R_2 = 72 °C/W. The slightly higher thermal capacities for segments 1 and 3 (*vis a vis* segment 2) can be ascribed to their having three open sides. The lower thermal resistances for segments 1 and 3 can also be explained by the presence of an extra open side, and to the added thermal losses via epoxy connections to the substrate and capillaries. Steady-state heating measurements gave a value of R_c = 30 °C/W. Measured thermal crosstalk among segments was about 56 % between adjacent segments, and 32% between the opposite side segments (e.g. for a 30 ºC temperature difference above ambient in segment 1, segment 2 increased 16.8 ºC and segment 3 increased ~9.6 ºC).

From the n-octane data used to construct the Golay plot characterizing the efficiency of the PDMS-coated μcolumn, k values ranged from ~4 to 6 and the minimum plate height, H_{min} = 0.026 cm, was obtained at the optimal velocity, $\bar{u}_{opt}$ = 11 cm/sec, which corresponds to a volumetric flow rate of 0.24 mL/min of N_2. The maximum plate count, N_{max}, was estimated to be 23,000 plates, or 3,800 plates/m. This value is somewhat lower than N_{max} values we have reported previously, and, in fact, subsequent μcolumns coated in a similar fashion yielded N_{max} = 4,100 plates/m.

For reference, the energy required for a typical analytical cycle with the PEMM prototype was determined experimentally using global μcolumn heating. A 60-sec air sample was collected at 5 mL/min, followed by thermal desorption of the μPCF at 225 °C for 40 s. Then, a temperature programmed separation was performed, which entailed holding the μcolumn at 30 °C for 35 sec followed by a linear ramp at 40 °C/min to 110 °C and a 5-sec hold at that temperature. A re-set period of 3 min was then allowed for cool-down and purging of the inlet. Both the μPCF and the μcolumn returned to the baseline temperature of 30 °C within the 3-min cool-down period. The total cycle was 5.5 min and required 2,710 J, including all thermal, pneumatic, and electronic components and functions. Of this total, 475 J (18%) was required for (global) μcolumn heating. If the energy required for electronic components were excluded, then

the μcolumn would account for 37% of the total energy (i.e., 475/1283 J), amply justifying efforts to reduce its contribution.

2.5.3.7. BTM vs. Experimental Retention Times. The accuracy of the BTM was evaluated by comparing predicted and experimental t_R values for the test compounds under a range of isothermal (i.e., 50 to 100 °C) and temperature ramped (i.e., 10 to 60 °C/min) conditions. Complete results are tabulated in ref. Z3. Representative results at 60 °C (isothermal) and at 40 °C/min (programmed) are presented in Figures 2.8a and b, respectively. As shown, the errors were quite small, ranging from -0.31 to +2.1 s in Figure 2.8a and from -0.57 to +2.4 s in Figure 2.8b. In both cases, the errors increased as t_R increased (i.e., as the volatility of the compounds decreased). Among all tests run under isothermal conditions, absolute errors were < 1.4 s for the six most volatile compounds and < 3.3 s for the three less volatile compounds, with the exception of n-decane at the lowest temperature (50 °C) which had an error of -6.1 s. Since the magnitudes of the errors increased with t_R value, the fractional errors were small and the model performed adequately well for all practical purposes.

Among all tests run under temperature ramped conditions, absolute errors were generally higher than for isothermal tests but showed similar trends with compound volatility (i.e., t_R value) and, again, the model performed adequately well for the purposes of guiding segmented heater scheduling. The observed tendency toward negative errors can be ascribed to wall adsorption on interconnecting capillaries, to temperatures being slightly lower than indicated by the RTDs due to small vertical thermal gradients for isothermal cases, and additionally to lags in actual heating rates due to the thermal mass of the μcolumn for temperature ramped cases.

2.5.3.8. Separations with Global vs. Zone Heating. Isothermal and temperature programmed separations of each ternary subset mixture in Table 2.1 were performed with zone and global heating. The zone heating schedule was based on BTM. Figures 2.9a and b present representative results for the “general” subset and show that the values of t_R were nearly identical, regardless of the heating method. The complete set of t_R values obtained for all subsets are presented in ref. Z3 and confirm the close agreement in t_R values in all cases.

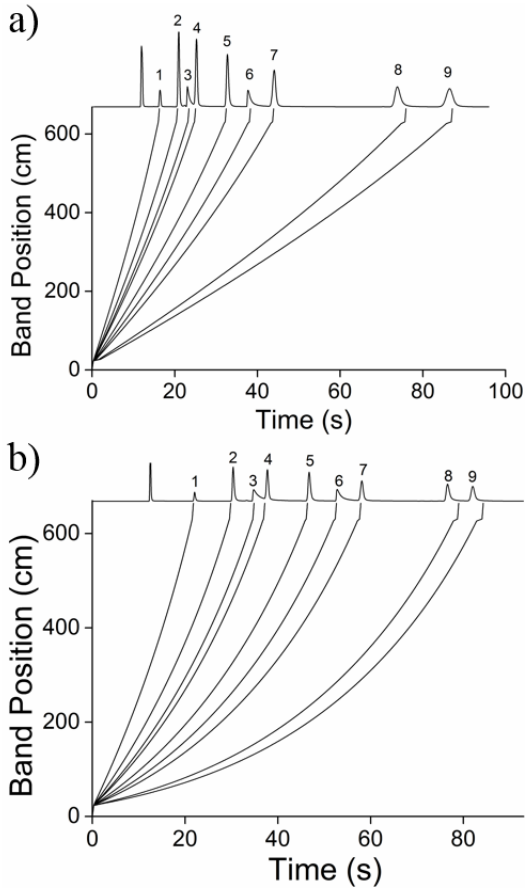

Figure 2.8. Experimental chromatograms of the nine test compounds under a) isothermal (60 ºC) and b) temperature ramped (40 ºC/min starting at 30 ºC) conditions. Experimental traces are shown across the top of each panel and the BTM-predicted trajectories are shown beneath. GC conditions: ~0.05 µg injection for each compound; 13.5 PSI He inlet pressure; 6-m long PDMS-coated µcolumn; FID. Note: solvent peak (CS_2) appears before peak 1. Identities of peaks 1-9 are given in Table 2.1.

2.5.3.9. Temporal Profiles of Temperature and Power. Figures 2.10 a and b show experimental temperature and power profiles, respectively, for global and zone heating of the μcolumn for an isothermal separation at 60 °C, suitable, say, for the low-volatility subset in Table 2.1 (note: the global temperature profile is not actually shown because it would have obscured the details of the zone heating profiles, but it would correspond to an initial rise along the solid line shown in the plot in Figure 2.10 a and then a constant temperature for the remainder of the run. Figure 2.10 c and d show the corresponding profiles for a linear temperature ramped separation from 30 to 83 °C at 40 °C/min (in this case, the global temperature profile corresponded to a linear increase to ~95 s for all segments). The PWM power profiles represent 1-s averages (i.e., they were not smoothed significantly). For the zone-heated isothermal case, the segment 1 heater was turned on a t = 0 and brought up to 60 °C within 9 s (i.e., at 200 °C/min). The turn-on times of the segment 2 and 3 heaters, 20 and 34 s, respectively, were determined from BTM estimates of the residence times of n-nonane (i.e., the earliest eluting component of the mixture) in segments 1 and 2, after adding the offset required for pre heating the first segment and subtracting the time required to bring the current segment to 60°C (~6 s for both segment 2 and 3). The corresponding turn-off times for segments 1 and 2 were determined from BTM estimates of the residence times of n-decane (the last-eluting component) in segments 1 and 2 and were set at 42 and 70 s, respectively. As shown, control was quite good, as the set point temperature was reached in all cases within +/- 1 ºC and a slight overshoot was only evident for segment 1. Note that the initial gradual rise in temperature for segments 2 and 3 was due to thermal cross talk from segment 1 over the first ~20 s and from segments 1 and 2 over the first 38 s, respectively.

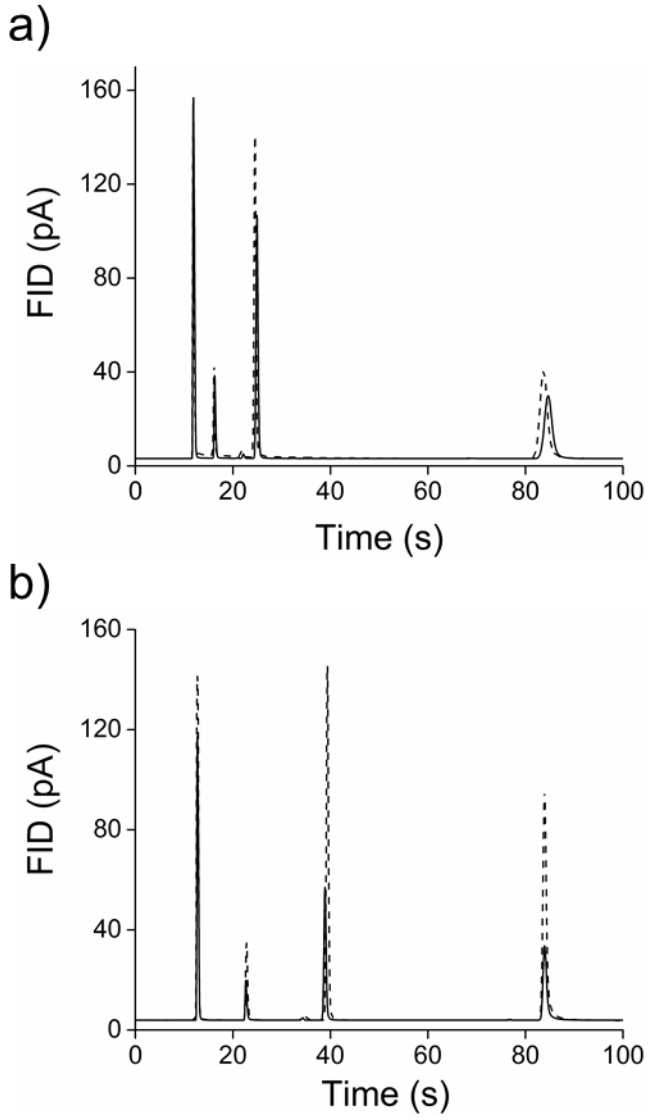

Figure 2.9. Superimposed a) isothermal (60 °C) and b) temperature ramped (40 °C/min) chromatograms of the "general" subset of compounds (Table1) with global (solid lines) and zone (dashed lines) heating. The first peak in each trace is solvent (CS_2). In order to see the similarities in t_R values for zone vs. global heating when the traces were superimposed, slightly different injection volumes were used. Zone heating schedule was determined via BTM.

The power profile for the global heating case (Figure 2.10b) showed an initial rapid increase followed by a slower increase to its maximum within 9 s, consistent with PWM control. Having reached the set-point temperature of 60 °C, the power then dropped to a steady-state value of ~ 2W, which maintained the μcolumn at 60 °C over the 100-s run. For the corresponding zone heating power profile, there were peaks in power dissipation at the three points in time corresponding to the initial heating of the successive segments followed by a biphasic decline to the levels required to maintain the 60 °C steady-state temperature.

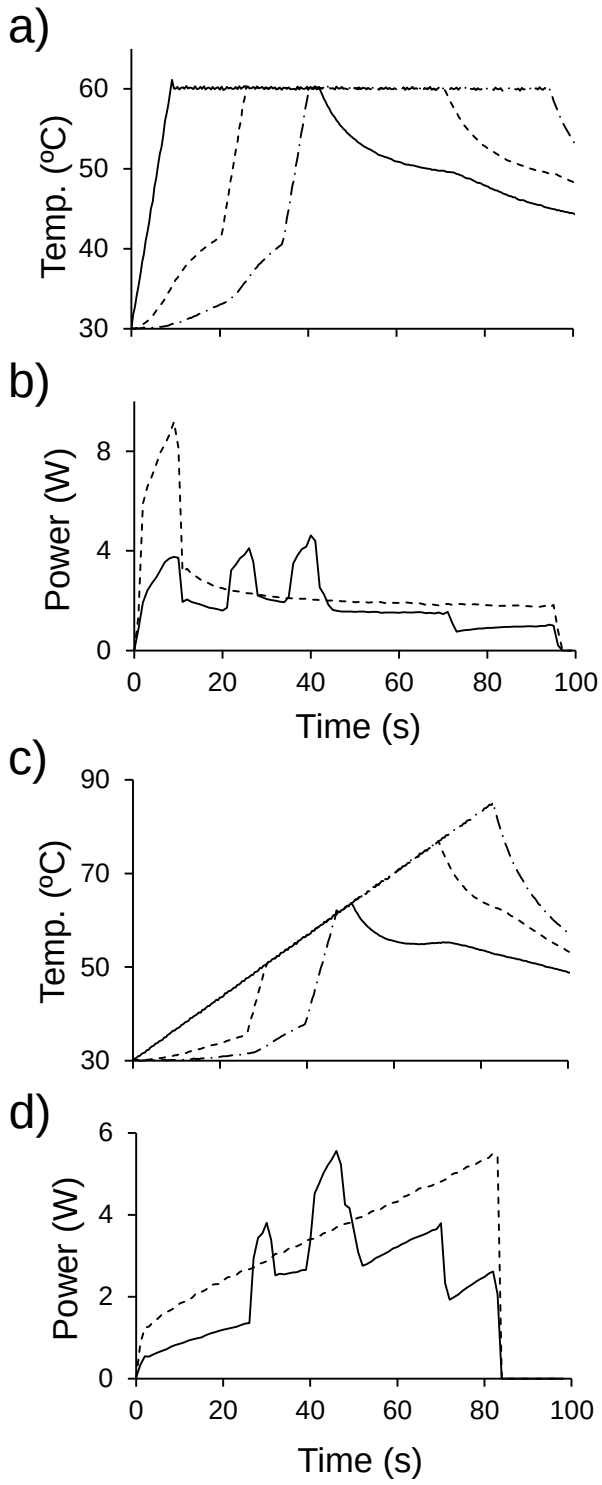

Figure 2.10. Measured a) and c) temperature profiles and b) and d) power profiles of the zone-heated µcolumn for an isothermal separation at 60 ℃[a) and b)], and a temperature-ramped separation at 40 ℃/min [c) and d)]. Shown are the temperatures of segment 1 (solid line), 2 (dashed line) and 3 (dot dashed line) of the zone heated µcolumn. Applied instantaneous total power is shown for zone (solid line) and global heating (dashed line). Profiles correspond to conditions suitable for the low volatility subset.

As expected, the peak power required to heat each separate segment was much lower than that required for global heating. After the second power peak, both segments 1 and 2 had to be maintained at 60 °C, so the steady-state power level increased slightly. Since the turn-off time for segment 1 coincided with the turn-on time for segment 3 (Fig. 2.10a), the third power peak was attenuated. About 1.5 W was required to maintain segments 2 and 3 at steady-state until t = 71 s, when the segment-2 heater was turned off and the power was decreased to the value needed to maintain segment 3 at steady state.

After the segment-3 heater was turned off, the temperature decreased at a rather low rate (Fig. 2.10a), in part, due to the lack of active cooling within the GC oven. (note: in the PEMM, active cooling is provided by fans that bring all three segment down to baseline temperature within 3 min). It is apparent by visual inspection that the integrated area under the power-time profile for zone heating was less than that for global heating. Indeed, for this run, the value of E_R was 0.26.

Fig. 2.10c shows the corresponding temperature profiles for BTM-guided zone heating of the temperature-ramped separation. The profile for the global heating case would follow the line formed by the combination of zone-heated profiles. Segment 1 was heated from the outset at the designated rate of 40 °C/min. Heat transfer to segments 2 and 3 was, again, evident by the gradual increase in their temperatures prior to their heaters being turned on at 26 and 40 s, respectively. Turn-off times corresponded to the elution of n-decane through each segment.

The power profiles followed the expected patterns, where an initial rapid step was required to overcome the thermal capacitance (first term of Eq. 2) and then a linear increase was required to overcome the heat loss to the environment and adjacent segments while continuously increasing the μcolumn or segment temperature at the specified rate. As with the isothermal cases, the power required early in the run was lower for zone heating, and was primarily driven by C_i and R_i of segment 1 (R_c notwithstanding). The peaks corresponded to the turn-on times of segments 2 and 3, and the latter peak was higher because segment 3 needed to be brought to a higher temperature to keep pace with the ramp. The successive decreases in power at 48 and 70 s corresponded to the turn-off times of segments 1 and 2, respectively. Once again, apparent by visual inspection, the energy for zone heating was less than that for global heating (i.e., $E_Z < E_G$). In this case, the value of E_R was 0.27.

2.5.3.10. Energy per Analysis. Fig. 2.11 plots the simulated values of energy versus analysis time (t_a) for three different isothermal (Fig. 2.11a) and temperature ramped (Fig. 2.11b) separations. Each data point along a given curve is designated by a symbol corresponding to the subset to which it belongs (see Fig. 2.11 caption). Furthermore, the x-coordinate for each data point corresponds to the time required for elution of the least-volatile component of the given subset mixture, as determined by BTM. For a given temperature condition there are three curves shown, one for global heating (filled symbols, solid curve) and two for zone heating. Of the latter, one (open symbols, dashed curve) entailed all three segment heaters being turned on at the outset, followed by segment 1 and 2 heaters being turned off in sequence as the least volatile compound eluted through them. We refer to this below as the "early-off" scenario. The other zone heating scenario (open symbols, dotted curve) entailed each segment heater being turned on and then turned off on a schedule dictated by the residence times of the eluting compounds within that segment. We refer to this as the "late-on/early-off" scenario.

As expected from Eqs. 3 and 5, and as observed in Figs. 2.11a and 2.11b, the time dependence of the energy consumption is linear for the isothermal separations and quadratic for the temperature ramped separations. The y-intercept of each curve in Fig. 2.11a corresponds to the $C_i\theta_s$ term from Eq. 3, which increases with increasing set-point temperature and contributes equally to the energy for all heating scenarios at a given set point. As a result, its fractional contribution to the total energy varies directly with the volatility of the subset. For

example, at 50 ºC, it is ~60% of the total energy for the high volatility subset (triangles) but only ~25% of the total energy for the low-volatility subset (squares). Hence, the energy *saved* by use of zone heating will vary inversely with the volatility of the subset (i.e., high < medium < low) for isothermal separations. This is not the case for temperature ramped separations (Fig. 2.11b) because the capacitance term contributes continuously to the energy consumed throughout the separation.

The higher the set-point temperature (Fig. 2.11a) or ramp rate (Fig. 2.11b), the greater the energy consumed for the separation, in spite of the shorter total elution times (i.e., smaller value of t_a). But the *dependence* on set-point temperature or ramp rate varies with subset volatility in the order low < medium < high, which is apparent by looking at the same symbol across different temperatures or ramp rates, regardless of whether global or zone heating is used. For example, in Fig. 2.11b, the ratio of energies consumed at 100 °C/min and 10 °C/min for the zone-heated separation of the high-volatility subset (open triangles) is ~103 J/19 J or about ~5 fold, whereas for the low-volatility subset (open squares) it is 255 J/135 J, or only ~2 fold. In all cases, however, the energy consumed with zone heating is less than that with global heating.

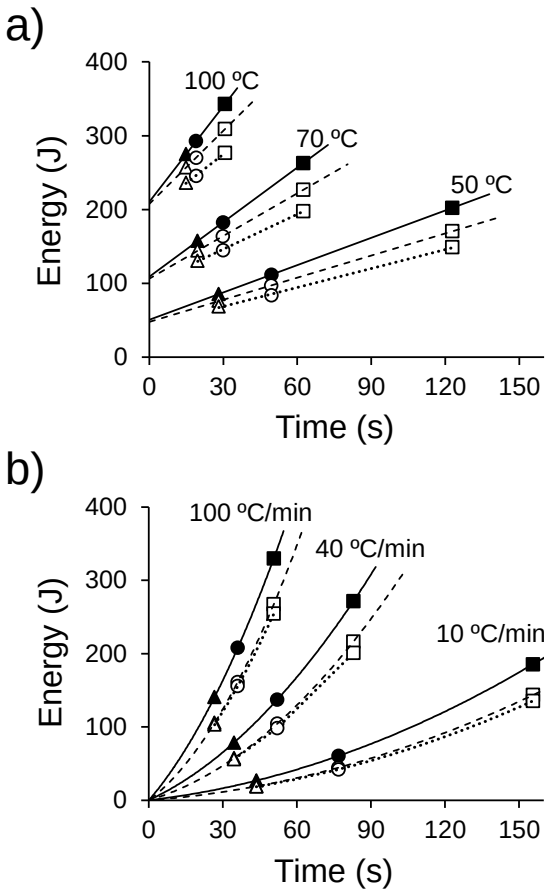

Figure 2.11. Simulated energy consumption vs. analysis time for the separation of each subset mixture under different a) isothermal and b) temperature ramped separation conditions. The analysis time was defined by the latest eluting compound in each subset: 2-hexanone (high volatility, triangles), 3-heptanone (medium volatility, circles), and n-decane (low volatility, squares). Filled symbols and solid lines are for global heating cases; unfilled symbols and dashed lines are for zone heating cases with only early turn-off of segments 1 and 2; and unfilled symbols and dotted lines are for zone heating cases with both early turn-off of segments 1 and 2, and late turn-on of segments 2 and 3.

The extent of energy savings from zone heating bears closer examination. As shown in Figs. 2.11a and b, and highlighted further with the example in Fig. 2.12 a and b, the specific zone-heating scenario employed affects the energy saved to a greater degree for isothermal separations than for temperature ramped separations. For all isothermal set-point temperatures, the energy reduction for the "early-off" zone-heating scenario is about 55% of that for the "late-on/early-off" scenario. This is true for all analyte subsets, and is shown clearly in Fig. 2.12 a, for the specific example of the low-volatility subset. In contrast, for the temperature-ramped separations, regardless of the ramp rate, the energy reduction for the "early off" zone-heating scenario is about 82% of that for the "late-on/early-off" scenario. That is, the reduction in energy for zone (vs. global) heating is predominated by turning off the heaters for segments 1 and 2 as soon as they are no longer contributing to the separation. This, in turn, indicates that the residence times of the latest eluting component of a mixture (i.e. typically that with the lowest p_v value) in the first two segments of the μcolumn dictate the energy reduction achievable with zone heating in a temperature ramped separation.

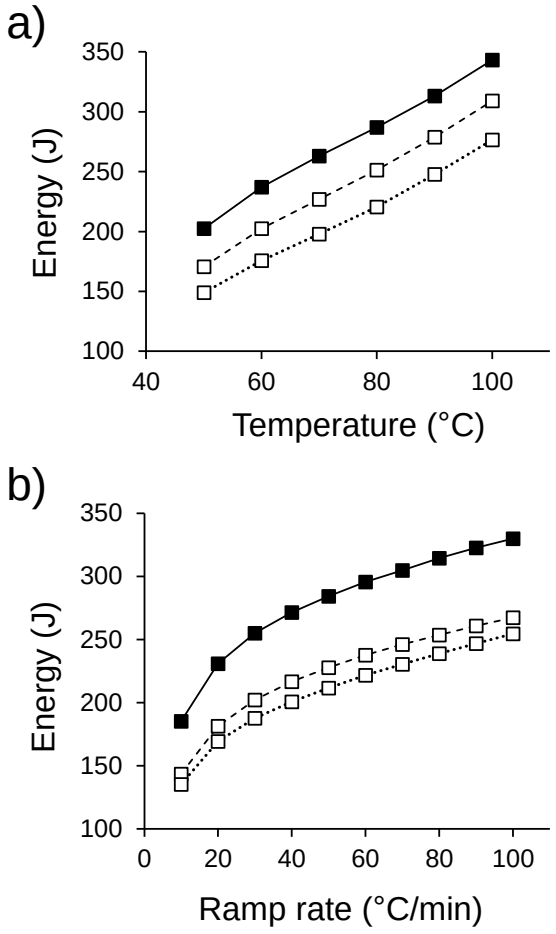

Figure 2.12. Simulated energy consumption for the low volatility subset under a) isothermal conditions and b) temperature ramped conditions at different temperatures and ramp rates, respectively. Filled squares and solid lines are for global heating; unfilled squares and dashed lines are for zone heating with only early turn-off of segments 1 and 2; open squares with dotted lines are for zone heating with both early turn-off of segments 1 and 2, and late turn-on of segments 2 and 3. The heating times were based on BTM derived retention time values.

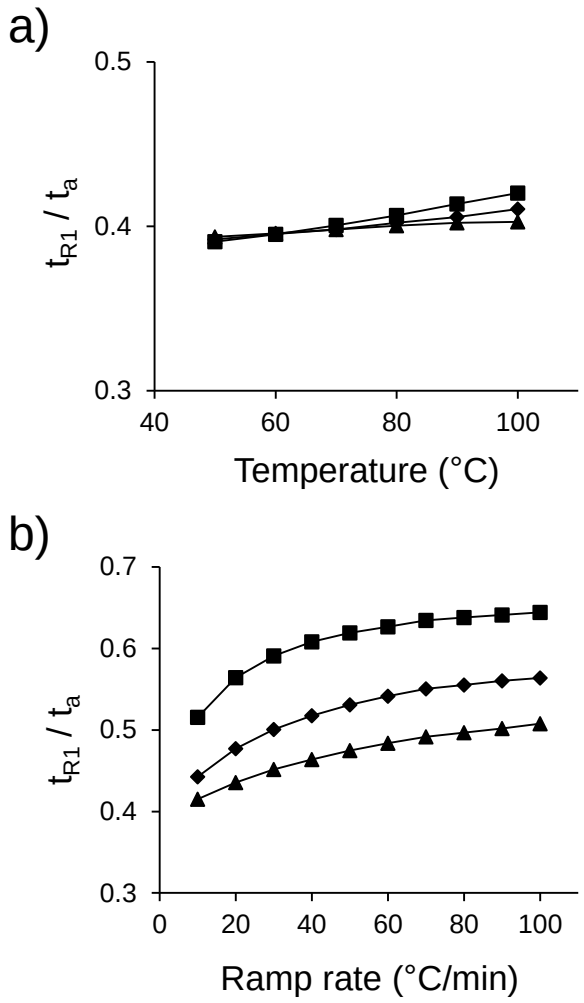

Figure 2.13. Simulated fraction of time spent by a compound in the first µcolumn segment as a function of a) isothermal temperature and b) ramp rate. This variable is a measure of the curvature of the band trajectory. Triangles: 2-hexanone; diamonds: 3-heptanone; and squares: n-decane.

To probe this matter further, Figure 2.13 presents the ratio of the residence (or retention) time in segment 1, t_{R1}, to the total analysis time (t_a) under isothermal and temperature-ramped conditions for the least volatile component of each subset mixture. For isothermal conditions (Figure 2.13a), the ratio was about 0.4 and there was very little difference among the subsets or across the set-point temperatures. This is a reflection of the linearity of the band trajectories (see Fig. 2.8a). In contrast, for the temperature-ramped conditions the t_{R1}/t_a ratio increased monotonically with ramp rate and also increased with the p_v values of the three analytes. These trends arise from the curvature of the band trajectories under temperature-ramped conditions (Fig. 2.8b), and from the different degrees of curvature that arise as a function of both the ramp rate and analyte volatility.

Since the relative amount of time spent in segment 1 (and, thus, segment 2) differed markedly, so, too, did the impact of the specific zone-heating scenario. In all cases, the time spent in a given segment was in the order segment 1 > segment 2 > segment 3. Furthermore, since the lower volatility compounds spent relatively (and absolutely) more time in segment 1 than the high volatility compounds, the energy reduction was smaller for the low volatility subset. That is, since the segment 1 heater could be turned off earlier in the separation of the higher

volatility subsets, it spent relatively more time off than it did in the separation of the low volatility subset. Also, across all subsets, the energy reduction decreased with increasing ramp rate, for the same reason.

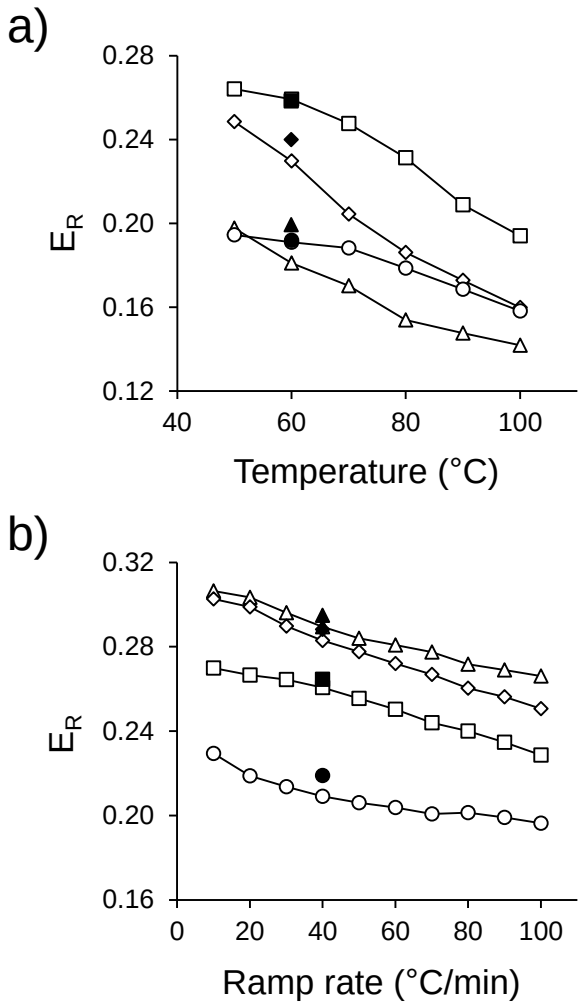

Figure 2.14. Fractional energy reduction, E_R, due to zone (vs. global) heating of the µcolumn for a) isothermal and b) temperature ramped separations of different compound subsets: high volatility (triangles), medium volatility (diamonds), low volatility (squares), and general (circles). Unfilled symbols represent simulated data and filled symbols represent experimental data.

Figure 2.14 a and b compare values of energy reduction, E_R, for isothermal and temperature-ramped separations, respectively, of all four subset mixtures. Experimental ER values (filled symbols) differed from modeled ER values (unfilled symbols) by -0.1 to 1.8% for isothermal conditions and by -0.1 to 1.2% for temperature ramped conditions, i.e., they were generally slightly higher than the modeled values. For isothermal separations, the energy saved by use of zone heating (i.e., with the "late-on/early-off" scenario) decreased as the temperature increased and as the volatility of the mixture components increased, consistent with the data in Fig. 2.11 a. That is, the mixture requiring the longest time for separation yielded the most savings, with the largest E_R value in this data set estimated to be ~26%, at the lowest temperature of 50 °C for the lowest volatility subset.

Figure 2.14 a also shows that the energy reductions for the general subset fell between those of the high and medium subsets and had less of a temperature dependence. This is because of the wider range of volatility spanned by this subset and the corresponding demands for longer segment heating times. For the temperature ramped cases in Figure 2.14b, the reductions in energy with zone heating were greater than those for isothermal cases. In these cases, however, high and medium volatility subsets yielded greater energy reductions than did the low volatility and general subsets, which is expected from the BTM curvature differences seen in Figure 2.13 b.

The range of E_R values among all conditions and subsets in Figure 2.14 is 14 to 31%. For a given subset a larger range of values was spanned for isothermal separations across the different temperatures than for temperature ramped separations across the ramp rates examined. In all cases, the price paid for more rapid elution times was smaller energy savings, with the amount depending on the mixture components and time of analysis. Regardless of the specific value of E_R, the range of energy savings was significant.

2.5.3.11. Conclusions About Segmented, Zone-Heated Microcolumn. From the preliminary results reported here, we conclude that zone heating of this novel segmented µcolumn can afford significant energy savings without sacrificing chromatographic resolution or analysis time relative to global heating of the entire chip. The energy saved is a function of the structure of the device and materials of construction, the heating profile employed in the separation, and the absolute and relative vapor pressures of the analytes in the mixture being separated. For the limited data set generated here the fractional reduction in energy due to zone heating ranged from 14-31%. Since µcolumn heating can account for > 35% of the energy consumed by the fluidic components of a wearable µGC, such as the PEMM prototype we have developed, a net reduction of ~5-10% in the energy per analysis could be realized (electronics notwithstanding), with a corresponding increase in battery life.

The measures taken here to thermally isolate the segments still allowed thermal cross talk of 56% between adjacent segments. Furthermore, the substrate and cover plate used were rather thick (i.e., 500 and 200 µm, respectively). Additional efforts to reduce the mass of the device and to improve thermal isolation (i.e., to increase R_c) would lead to improvements in energy savings. The substrate thickness is currently constrained by the need for edge-wise connections to capillaries having outer dimensions > 300 µm. The use of Si as the substrate offers advantages of well-established machining methods such as DRIE. Its thermal conductivity reduces thermal gradients and thermal response times, but also increases cross talk. On balance, Si would seem to be a suitable substrate. Although we have found Pyrex wafers to become fragile below a thickness of 200 µm, post-bond polishing might be used to reduce the thickness by a substantial fraction with less risk of fracture.

Integral to this concept is the use of BTM and the associated need for temperature dependent *k* values of all analytes, which increases the overhead associated with implementing this technique. However, since the temperature dependence of retention factors, particularly with PDMS stationary phases, is predictable, it should be possible to collect a minimum of reference data points (e.g., at, say, two temperatures) and to then interpolate or extrapolate *k* values with sufficient accuracy to implement BTM and, thus, to schedule the zone heating required for separation of even moderately complex vapor mixtures.

In follow-on work, we plan to explore the extent to which zone heating might enhance peak capacity while simultaneously minimizing analysis time. The capability for rapidly and precisely ramping the segment temperatures should facilitate such efforts. Since we have installed these µcolumns in the PEMM prototypes we are currently testing, any enhancements we might discover could be readily put into practice in a field-ready, wearable PEMM 2 unit.

2.6 Phase 3/Aim 3

2.6.1. Introduction to Phase 3/Aim 3

Phase 3 addressed **Aim 3,** to construct 3 PEMM-2 prototypes with embedded microcontrollers that are suitable for field deployment and operate continuously for 8 hrs on battery power. On the basis of results from Phases 1 and 2, the components and configurations of the PEMM 2 prototypes were determined and the operating parameters and conditions established (i.e., sampling, stabilization, injection/separation/detection), as well as required flow rates, heating rates, max. temperatures, durations of heating events, and microcolumn temperature programs. The nature and quantities of adsorbent materials, stationary phase thicknesses, and MPN sensor interfaces were also determined. Simultaneous determination of mixtures of 10-15 VOCs in a complex background of interfering VOCs, which was an original part of Aim 3 was shifted to Aim 4 and completed as part of the performance characterization of the PEMM 2 prototype. In the wake of our switch from 3DS to VGC partners, we took on some of the tasks originally proposed to be addressed by the commercial partner, to avoid further delays in the project.

Figure 3.1 shows a conceptual rendering of the Gen-2 prototype as conceived of as of July, 2014. Since then, the design has evolved and the diagrams in Figure 3.2 are more accurate renderings of the final form factor and arrangement of key components of the instrument.

2.6.2. PEMM 2 Electronic Subsystems

Table 3.1 provides the initial set of power budget specifications for the PEMM-2 prototype. A significant reduction in the power consumption of PEMM 2 (relative to PEMM 1) was achieved by using a microcontroller for the functions of data acquisition, control of system components and communication tasks, thus replacing the DAQ cards that are used for the PEMM 1 prototype. A very conservative energy consumption of 5.6 kJ was estimated considering specifications of commercial available devices that meet minimum requirements for this application.

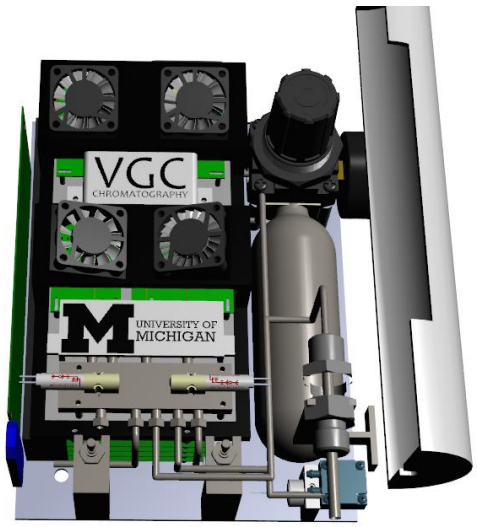

Figure 3.1. Artist's rendering of the Gen-2 PEMM prototype as of July, 2014.

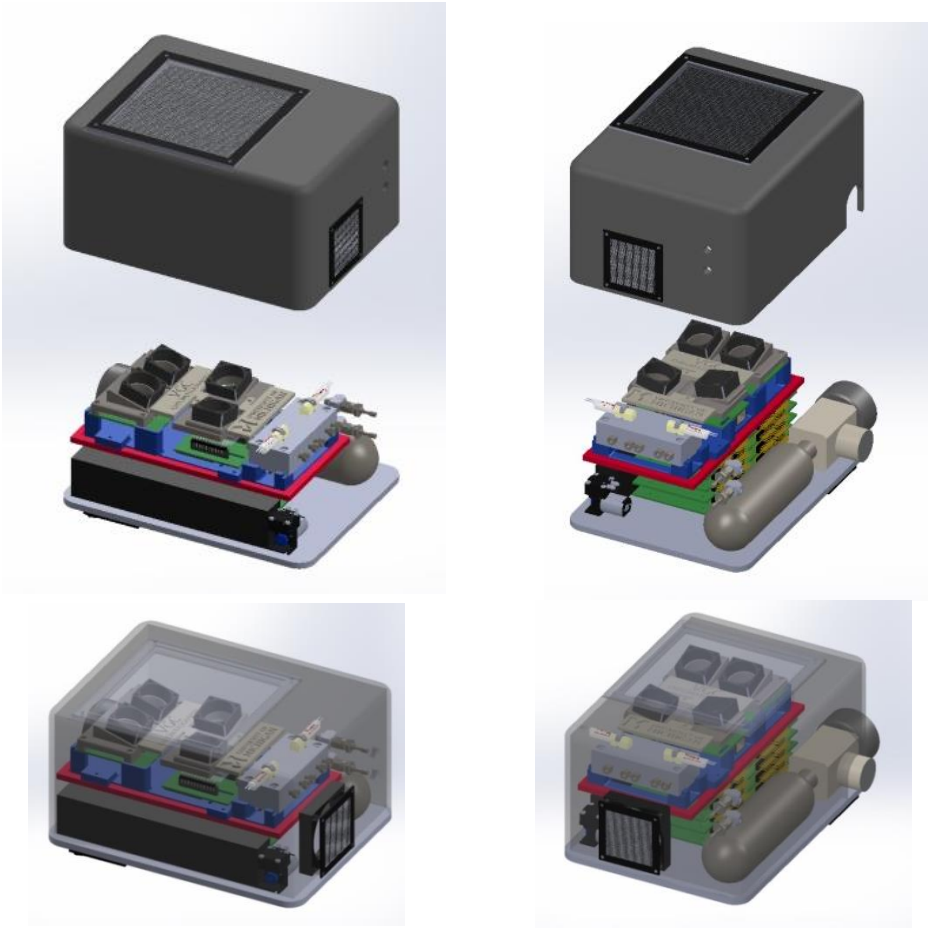

Figure 3.2. Renderings of the final form factor and component layouts of the Gen-2 PEMM prototype assembled by VGC.

Simulation data of new micro-sampler heater designs showed that a heating profile of 25-285 °C in 0.8 sec is achievable, requiring only one third of energy compared to PEMM 1. Similarly, other important improvements in power consumption were realized by using the new microcolumn design that which show better heating efficiency, requiring less than 3 W for heating to 180°C.

For battery requirements estimation, 8 hrs of continuous operation of the instrument was targeted, with 8.6 minutes for each analytical cycle (Table 3.1). The average power dissipation is 10.9 W and the battery capacity is 87 W-h. The latter is very close to our target of 80 W-hr. These projections were very encouraging. Considering the Gen-2 power requirements an ultra-high energy Lithium-Ion battery was proposed, with 14.8V working voltage, 82.88W-h nominal capacity and 7A peak current. According to estimated peak power, a 2.8A peak current will be drawn at this operation voltage.

Table 3.1. Preliminary power budget for the PEMM 2 prototype.

PEMM GEN 2 – Power Consumption						Time (min)	3		Time (min)	0.3		Time (min)	5		Time (min)	0.3	
						SAMPLING			STABILIZATION			ANALYSIS			RECOVERY		
	Load	Voltage (V)	Current (mA)	Power Supply Efficiency	Power (W)	Time (min)	Energy (W-min)	Avrg. Power (W)	Time (min)	Energy (W-min)	Avrg. Power (W)	Time (min)	Energy (W-min)	Avrg. Power (W)	Time (min)	Energy (W-min)	Avrg. Power (W)
Electronics	Enclosure fan	5	130	0.71	0.9	3	2.8	0.9	0.3	0.3	0.9	5	4.6	0.9	0.3	0.3	0.9
	Microcontroller	5	200	0.71	1.4	3	4.2	1.4	0.3	0.4	1.4	5	7.1	1.4	0.3	0.4	1.4
	Wireless Module	5	50	0.71	0.4	3	1.1	0.4	0.3	0.1	0.4	5	1.8	0.4	0.3	0.1	0.4
	Manifold board	6	20	0.85	0.1	3	0.4	0.1	0.3	0.0	0.1	5	0.7	0.1	0.3	0.0	0.1
	MEMS board (actuators)	21	15	1.00	0.32	3	0.9	0.3	0.3	0.1	0.3	5	1.6	0.3	0.3	0.1	0.3
	MEMS board (CR amplfiers)	+/- 12	10	0.86	0.28	3	0.8	0.3	0.3	0.1	0.3	5	1.4	0.3	0.3	0.1	0.3
Flow	Pump	6	80	0.85	0.6	3	1.7	0.6	0.3	0.2	0.6	5	2.8	0.6	0.3	0.2	0.6
	5 x Latching valves	5	650	0.71	4.59	0.01	0.0	0.0	0.01	0.0	0.2	0.01	0.0	0.0	0.01	0.0	0.2
u-components	uSampler ramp	10	2000	0.97	20.6							0.008	0.2	0.0			
	uSampler hold	3	640	0.44	4.3							0.33	1.4	0.3			
	uColumn 1	21	80	0.56	3.0							5	15.1	3.0			
	uColumn 2	21	80	0.56	3.0							5	15.1	3.0			
	CR sensors + RTD	3	0.03	1.00	0.00	3	0.0	0.0	0.30	0.0	0.0	5	0.0	0.0	0.30	0.0	0.0
	CR sensors heater	6	300	0.85	2.12	1.5	3.2	1.1	0.15	0.3	1.1	2.5	5.3	1.1	0.15	0.3	1.1
	Interconnection heaters	6	600	0.85	4.24	1.5	6.4	2.1	0.15	0.6	2.1	2.5	10.6	2.1	0.15	0.6	2.1
					Total		**21.5**	**7.2**		**2.2**	**7.3**		**67.7**	**13.5**		**2.2**	**7.3**

2.6.2.1. Microcontroller Programming and Implementation. Figure 3.3 shows the electronic control system architecture, consisting of 3 macro components: the PIC, the ARM, and the Raspberry Pi (RP). The PIC32MX320 (PIC32) consists of an 80 MHz MIPS32 M4K CPU, along with 128KB of onboard flash, and 16KB of RAM. The PIC32 is inexpensive, small, and low power. A previous VGC project with high time accuracy was completed using the PIC32, which included communication with the RP. The PIC32 system includes 4 channels of high-accuracy digital outputs that function in a similar manner to the high-accuracy ADC architecture.

The STM32F303 microcontroller (ARM) contains an ARM Cortex-m4 CPU, which is one of the most powerful cores available in a microcontroller. With 4 onboard 12-bit ADCs, which can be multiplexed up to 39 input channels, 13 timers for PWM usage, 48Kb SRAM, and multiple SPI and UART, the ARM is ideal for moderate resolution, high speed data acquisition and feedback loops. Currently it handles all digital output scheduling (including a trigger signal for the PIC32 to begin data acquisition) and temperature feedback on 8 zones (4-segment linear ramping on all zones).

The RP is a COTS minicomputer used as an access point to the microcontrollers driving the PEMM 2. The RP (12 cm x 8 cm x 2.5 cm) features secure, standard software and easily interfaces over Wi-Fi and 3G networks. VGC has found customer acceptance of the RP to be positive. The PEMM 2 can be operated autonomously without the RP; however, data retrieval and setpoint adjustments must be made using the RP, either directly or by remote terminal. The RP can be disconnected during PEMM 2 operation or it can remain tethered to the PEMM 2 during daily use to allow the hosted website/UI access to real-time updates for industrial hygiene personnel.

The ARM board, driven by an STM32F303 microcontroller, controls all heating/cooling, temperature programs, and digital outputs for valve actuation. The PIC32 board, governed by a PIC32MX320 microcontroller, is responsible for the high precision data acquisition in the system. With cycle-accurate timing, the PIC board can collect 8 analog voltages with 24 bit precision and hardware clocked timing. The µCR array detector output channels are connected to a dedicated CR amplifier board, the output of which then connects to the PIC board's ADCs. The CR amplifier board contains the precision Wheatstone bridges, amplifier circuitry, and baseline measurement and correction circuitry.

The RP provides a high-level method of access to the microcontrollers, through an advanced user interface and method creation system. Once a method has been entered into the RP's interface, it is transferred into the configurations for the PIC and ARM. Upon starting the method, the ARM begins the temperature and digi-out program, and indicates the PIC to begin data collection whenever specified. This system allows for the creation of initial conditions before beginning data collection. These components are supported by a relay board, which contains solid state relays for heater and fan control, the H-Bridges needed to drive the valves on the manifold, and switching regulators for the microcontroller power supplies.

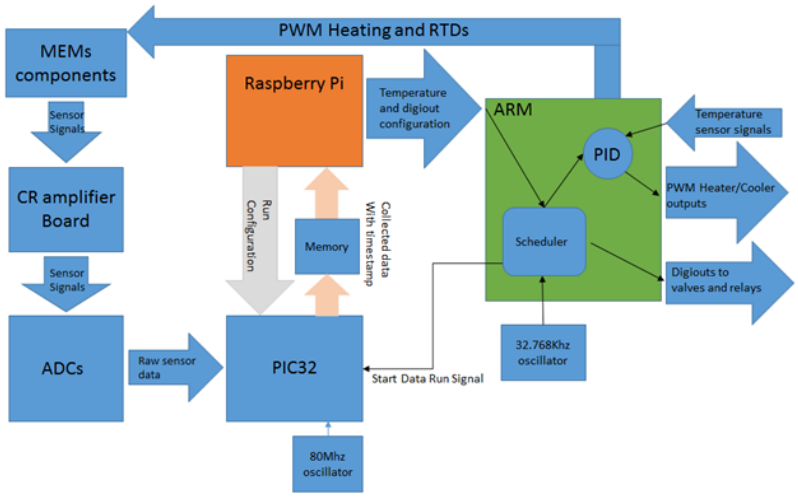

Figure 3.3. System architecture: the (embedded) PIC, the (embedded) ARM, and (remote) Raspberry Pi.

The key task for the ARM is event/temperature scheduling and temperature feedback logic (proportional-integral-derivative control, PID), which is summarized in Figure 3.4. The instrument scheduling routine (ISR) begins by collecting the data from the ADCs. The scheduler is updated with the current timestamp within the method, and the target for each temperature channel is sent to the PID calculation function, along with the current value of each channel. The scheduler also updates the digital output channels. The result from the PID calculation is a duty cycle percentage, which is then passed to the PWM function, in order to adjust the heater output and maintain the temperature. The serial output code is then executed, which contains all relevant data for this particular execution of the ISR, such as the current temperatures of each channel. The ISR then ends, and execution idles until the next interrupt.

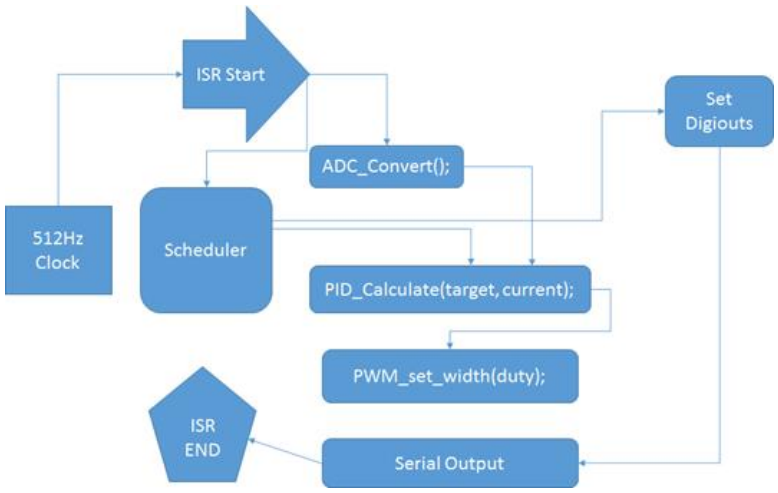

Figure 3.4. ISR functional routine and relational architecture.

The circuit board for sensor signal amplification/conditioning was redesigned for battery operation. Some components were replaced with low power components. Specifically, the low-noise high frequency operational amplifiers used in the old SPIRON prototype were replaced with lower power amplifiers, since high frequency capability is not necessary. For the actuation of system components, interface electronics to the microcontroller were redesigned with lower power components. New features include the control of the µPCF, heating of the µCR array, and the actuation of valves and pump. Additionally, the careful selection of operation voltages and replacement of voltage regulators with switching DC/DC converters with higher efficiency reduced power demands further. The interfacing and power electronics were integrated to the microcontroller and debugged using the new microfabricated components and fluidic system. Parameters of the interface were optimized. During development and subsequent mock field testing, a menu-driven, user-adjustable, graphic-user-interface was made available for operating the PEMM 2 prototype and acquiring data to permit facile adjustment of operating parameters.

A solid state flash memory was initially integrated into the microcontroller board to store more than 8 hr of collected sensor data at full resolution (~8Mb). For the wireless capability, the microcontroller has built-in circuitry to facilitate this function. But, we later added an RF transceiver module (3×4cm, 0.5 W avg. power) to the chip set that communicates with the microcontroller through a serial parallel interface and permits the transfer of the data to the RP. Remote instrument-status checking was thus incorporated. Note that many of the details of the approaches described have been iteratively modified to align better with the PIC microcontroller, ARM, and RP components being implemented by VGC.

The PEMM 2 prototype uses a low power pump (0.5W), low voltage fan (~0.75W) for cooling the interior of the instrument housing, and low power electronics. Among the improvements in the Manifold Board design, we replaced ICs and voltage regulators with surface-mount versions to reduce layout space requirements. Voltage regulators currently use aluminum heat sinks for power dissipation. Since voltage regulation drops will be relatively small (~2.5V max) we can use horizontally mounted devices soldered to copper pads on the board for heat dissipation. The lower current of manifold components also allow us to choose more space efficient relays with lower current capacity, between 1A avg and 3A peak, sufficient for all applied loads.

Since controlling circuits for latching valves only operate for very short times, components were upgraded to reduce standby power consumption. CMOS technology

monostable multivibrators have been chosen for generation of latching valve control pulses. Each IC consumes less than 80μA continuous current and can generate either a positive or negative polarization pulse for driving one latching valve circuit through an H-bridge. The selected H-bridge allows us to drive two latching valves and demands < 2.3mA during operation and 1μA in standby mode. Also, two low-power quad buffers/drivers were added to interface to the DAQ board and allow default off-state of control signals. The total current requirement of the manifold board is estimated at < 20mA.

Regarding new electronic components for the MEMS components, micropower amplifiers with similar electrical characteristics to their PEMM-1 prototype counterparts have been identified, estimating a significant reduction in the board power consumption (~0.3W max). These devices are also able to operate with a single power supply, which will allow to half the required power and save on an extra voltage conversion that is required for conventional dual power supplied designs.

The user interface communicates with the RP and features all essential control settings for a run. The embedded PIC and ARM can operate the system alone for multiple 8-hour shifts; however, the RP is required for changing settings and retrieving data. The option of integrating the RP into the PEMM 2 may be pursued in future iterations. When connected, the RP can connect over a Wi-Fi or 3G/4G adapter to allow the remote user to view data and adjust system parameters. This is achieved by hosting a secure website and synchronizing data from both microcontrollers in near-real time. Via this user interface as hosted by the RP, real time data is plotted in the graph window where standard zoom/pan adjustments can be made. Configuration parameters are adjusted in dynamic menus similar to standard GC control software platforms Key functions include:

- Real-time data display, where chromatographic data is displayed during a run. A user-defined delay can be set to reduce burden on the RP, typically 10-20 sec is used.
- Temperature and digital output configuration tabs. Each tab can be labeled according to the user's preference, a dynamic pull-down menu system is used to set the target value and time value of temperature programmed channels and the state and time value for digital output channels (valves, pump).
- Dynamic set points for temperature program and digital output values.
- Start button, depends on configuration, system will start immediately or after a set delay.
- Data collection configuration where users configure sampling rate, start/end times, number of CR channels, etc.

The revised PEMM 2 systems use an onboard ADC to measure the DAC supply voltage, which is measured and recorded to a log file whenever the DACs or ADC are accessed. This supply voltage also supplies the bias for the μCR array. All DAC settings are adjusted through the graphical interface using the "dacAdjust" subroutine. The dacAdjust program can be run from any directory on the RP. The onboard DACs are used for adjusting the baseline subtraction voltage of the differential amplifier circuit. Figure 3.4 shows the amplifier circuit.

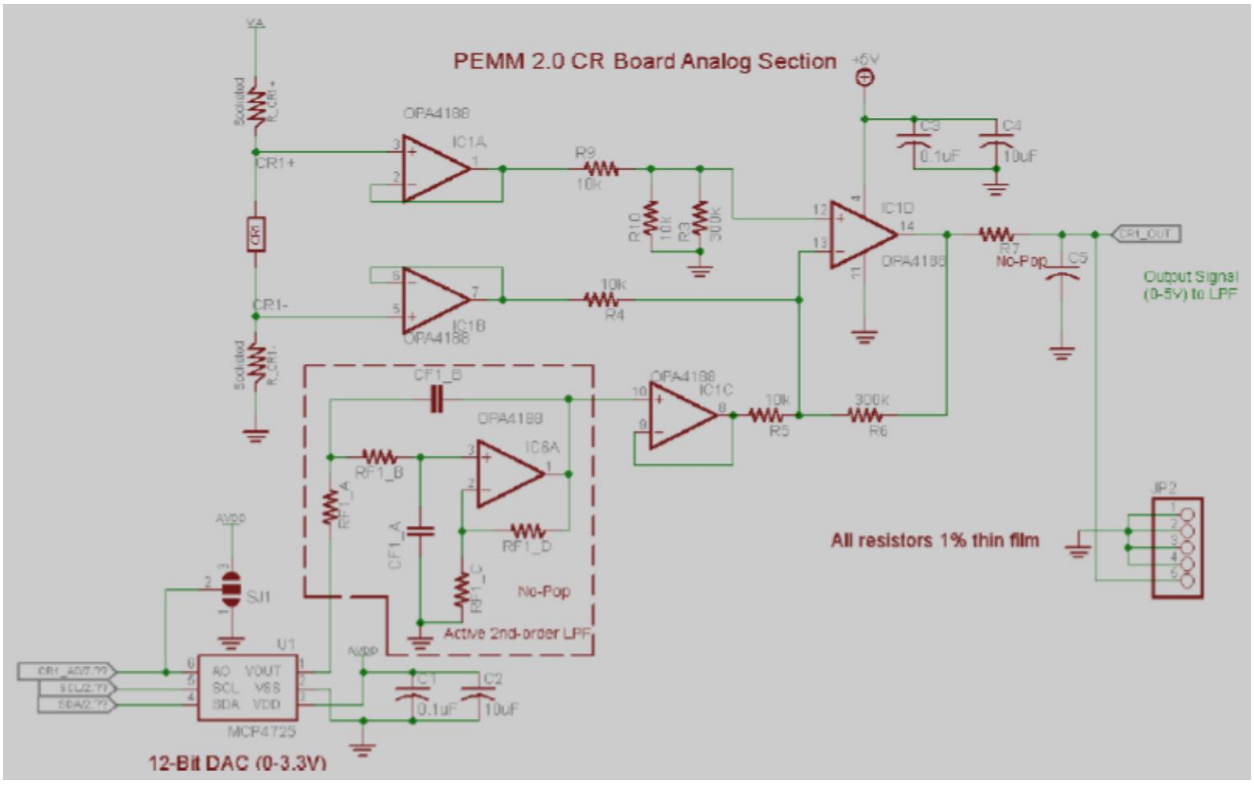

Figure 3.5. Amplifier circuit diagram for µCRs.

The amplifier circuit consists of a digital-to-analog-converter (DAC), an optional low-pass filter, voltage followers, and a final subtraction and amplification stage. The DACs operate internally as voltage dividers, so the output is always directly proportional to the supply voltage. Both the DAC supply voltage and the CR bias voltage ("VA" in Figure 3.4) are supplied by a separate CR2032 coin cell battery. The DAC circuitry typically consumes no more than 2 uA of current from the coin cell. This gives an approximate battery life of 110 hours. The CR and balance resistor current draw is typically less than 10 uA total, and has little effect on the coin cell life. To maximize coin cell battery life, the coin cell should be removed when the system is not in use because current will constantly be driven through each of the selected CR channels at all times when the coin cell and balance resistors are populated.

The revised PEMM 2 units have been retrofitted with an onboard 4-channel ADC to measure the coin cell voltage, as well as the supply rail voltages for the logic and heater subsystems. These measurements are all recorded automatically whenever the system is booted, DAC baselines are adjusted, and run(s) are performed.

The various other electronics discussed above require 3.3 V, 5 V, and ± 6 V. The 3.3 V and 5 V are supplied by high efficiency switching step-down regulators in order to minimize power loss. These are then filtered and supplied to the digital electronics. The ± 6 V rail is obtained directly from the battery pack. This rail need only be low noise, tolerance is not critical, and any voltage between ± 5 V and ± 12 V is acceptable for normal operation.

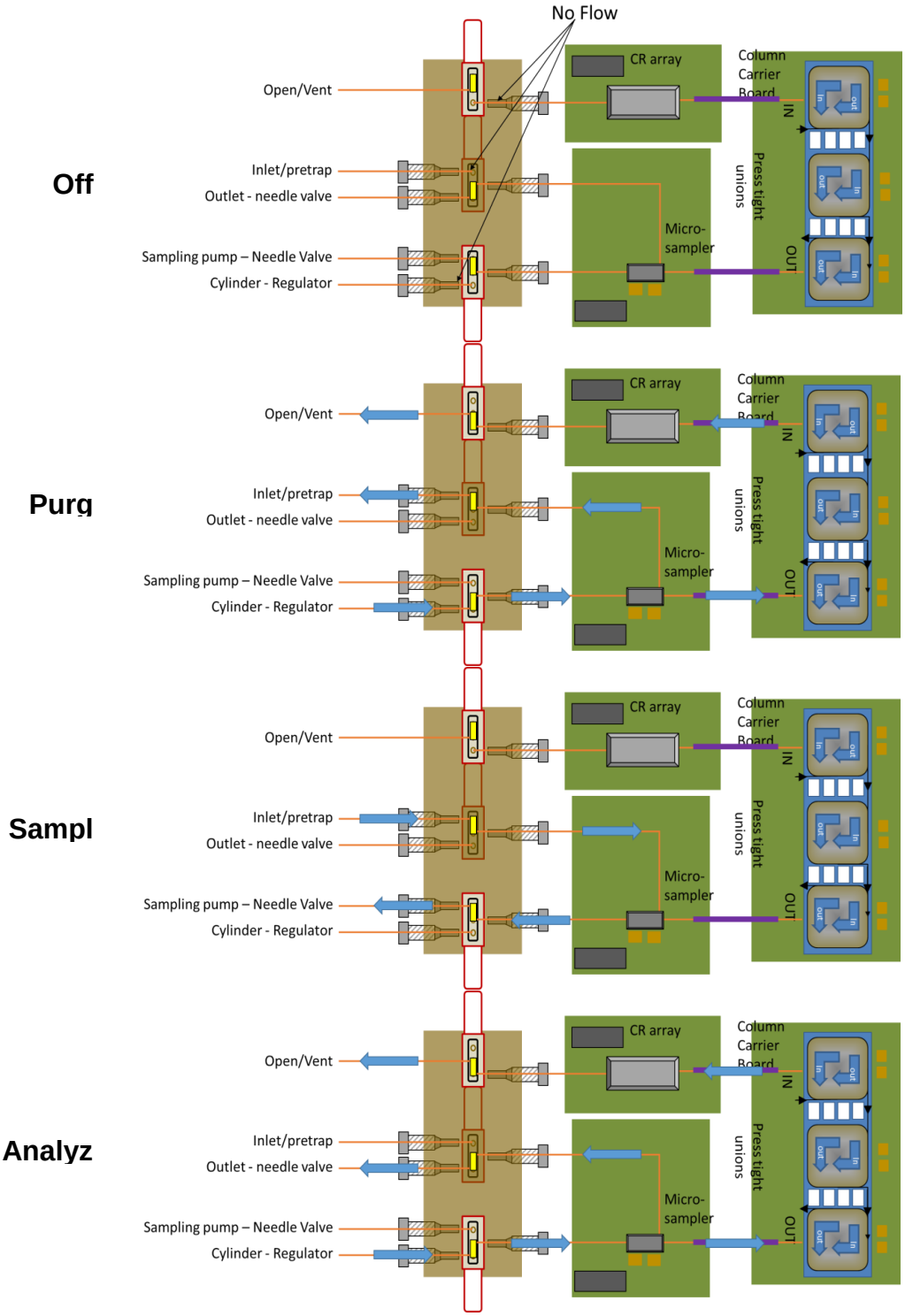

Figure 3.6. Block diagram schematic of PEMM operation including flow path through manifold. Blue arrows are used to show the direction of flow. See text for further description of each operation mode.

2.6.3 PEMM 2 Fluidic Subsystems

The fluidic pathways and components are shown in Figure 3.6. Face-sealing 3-way latching valves from the Lee Company have been used with good success by the UM team for several years. These small, low-power valves were an ideal choice for this project. To save space and weight, the manifold used in previous systems in conjunction with as many as 5 valves was simplified to the block schematic shown here using only 3 valves and limiting operation modes to the bare minimum needed for worker exposure monitoring. It was also made of aluminum.

Three latching solenoid valves (3-way fluidic design) are mounted on top/bottom of a manifold with entrance/exit holes machined in the sides (with side/top ports intersecting at right angles in the center of the manifold). They connect a common flow path to two different ports (one at a time) based on the polarity of the driving signal. The latching configuration holds the valve position after being set by a short dc voltage pulse (5 V, 200 ms). The valves can operate with positive or negative flow. The internals of the solid switching system contain active surfaces and significant dead volume, so should not be used between chromatographic components (i.e. the analytical flow path) without degradation of chromatographic performance. They can; however, be placed in the sampling flow path (as shown by UM in many previous efforts) without significantly affecting performance; this is due to the long exposure and low VOC concentrations typical of this process. Zero dead volume (ZDV) fittings, machined by Valco (Houston, TX), were added to the side ports of the manifold.

Four operating modes are proposed. In the “Off” mode, the solenoid valves are latched to stop flow in/out of the system and prevent carrier gas from being used. This is the default state of the system. “Purge-1” mode is used to flush all flow paths in the system; flow is pushed through the sampler/injector (μPCF), microcolumn, and sensor array while simultaneously venting through the inlet/pretrap. If desired, all chromatographic components can be heated to thermally desorb any contamination that may have collected on ad/absorbent materials, however, this was not included in the power budget. “Sample” mode connects the manifold to the sampling pump, reversing flow through the inlet and sampler, drawing sample into the system and capturing target VOCs in the sampler. After the defined sampling time, the system must be temporarily switched back to “Purge-2” mode to remove un-sampled VOCs from the analytical flow path and back flush the connection lines between the inlet and sampler. Finally “Analyze” mode can be triggered, reconnecting carrier gas to the manifold and directing sampler flow into the column. After a brief delay to establish flow through the column and sensor array, the uPCF can be heated, thermally desorbing the injection pulse of VOCs into the column. After the chromatographic analysis, the system can switch directly into “Sampling” mode for an additional analysis or switched to “Off” mode to wait.

Detailed drawings were generated for all mechanical assemblies and sub-assemblies. We used a removable substrate (“plate”) that carries the primary fluidic components and associated protective/cooling accessories. VGC proposed this as a necessary component to the system to enable reliable manufacturing, simplify assembly, aid in diagnostics, and facilitate field repairs. The active fluidic components, (μcolumn, μPCF, CR array, capillary interconnects, and valve manifold) can be carefully mounted to the carrier substrate in a clean, well-light assembly area. This removable carrier substrate (“plate”), manufactured with extrusion-based 3D printing technology, features a range of mechanical assistance to aid in assembling the microfluidic system. Device-specific carrier PCBs are keyed into place and slide along vias to facilitate connection to tapered glass press-tight unions and are eventually held in place with socket cap screws (hex keys are the safest fastener for this work).

The carrier substrate reversibly connects to a quick-attach socket (also manufactured with extrusion-based 3D printing technology) that is permanently mounted in the PEMM 2 enclosure. The carrier substrate (fully populated) is inserted into the socket at an angle, sliding

under the lip and seating into place. Socket cap screws are used to fasten the carrier substrate.

The microfluidic components are mounted to carrier printed circuit boards (PCB) designed by the UM team for facile handling and to simplify electrical connections. Wirebonds connect the components to the PCB while standard electrical connections are used to connect each PCB into the PEMM wiring harness. Further, dedicated electrical components, such as temperature sensors and voltage regulators, are placed on the carrier PCBs in some cases. The CRs plug into standard header sockets, while the PEMM wiring harness connects with a high-density slim-profile socket plug. Slots are manufactured into the PCB to allow sliding of the array/carrier PCB when making the fluidic connection to the tapered glass union between the μcolumn and CR array. A similar approach is used for the μPCF. Slots are used for the same purpose as discussed for the CR array. A standard header socket connector is used to connect to the wiring harness. The μcolumn PCB is mounted first into the carrier substrate so does not require slotted holes. Three sets of standard header pins are used to connect to the PEMM wiring harness.

Cooling fans are necessary for quick cycling of the microsystem. They are mounted on protective bridges above each microfluidic component. Since the μPCF and CR array are adjacent to one another, a single bridge with two fans addresses both components. The fans are mounted at an angle to isolate cooling flows (the μPCF may require cooling while the chromatographic analysis is still underway). The bridge mounts over the center mounting boss of the carrier substrate with a fitted socket to aid in assembly, the mounting boss doubles as an air dam to further isolate fan flow. Protective shields (wings) are mounted to the fan bridge to protect the capillary connections on either side of these components. A keyed foot and socket cap screw secure each wing to the fan bridge. The wing/bridge can be installed/removed as a single part or individually. The wings, with their prominent location amongst the microfluidic components, serve as ideal locations for branding with the logos of these two fine teams collaborating on this project.

The first version of the manifold was manufactured from stainless steel; conventional milling was used for all vertical holes and electrical discharge machining (EDM) used for the initial side-holes. The part was sent to Valco for the nine ZDV fitting details on the sides. Follow-up versions were made from aluminum (to reduce weight). Anodized coatings were tested for chemical inertness.

A fan bridge to protect/cool the μcolumns is similar to the fan bridge for the μPCF/CRs, except it sits directly on the carrier PCB and is fastened with the same socket cap screws as the carrier PCB. Tabbed edges on the carrier substrate aid in alignment when attaching the bridge and PCB to the carrier substrate.

The outer enclosure design was finalized for the first generation PEMM 2s and then was modified for the second generation instruments. Nuanced features of the mechanical design were continuously tweaked as both VGC and UM gained experience working with the carrier substrate and each microfluidic component. A commercially available fan filter was mounted to the top of the enclosure to filter air as it is drawn into the cooling fans mounted on the fan bridges.

Figure 3.7 shows photographic images of the partially assembled PEMM 2, the fully assembled PEMM 2 on the belt of one of the research team members, and on a balance showing its weight of 2.06 kg. Figure 3.8 shows the fully assembled PEMM 2 with and without its top cover in place. The majority of user/convenience features were realized after 3D printing earlier parts of the prototypes. Approximately 20 3D printing/mechanical refinement cycles were completed.

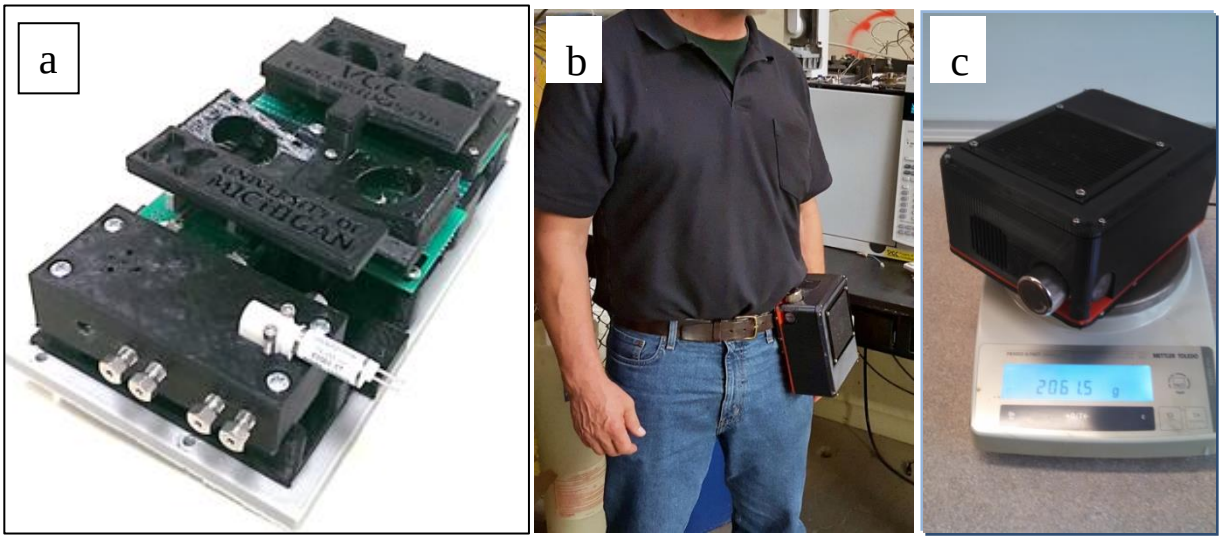

Figure 3.7 a) partially assembled PEMM 2; b) fully assembled PEMM 2 on the belt of one of the research team members; c) PEMM 2 on an electronic balance showing weight of 2.06 kg.

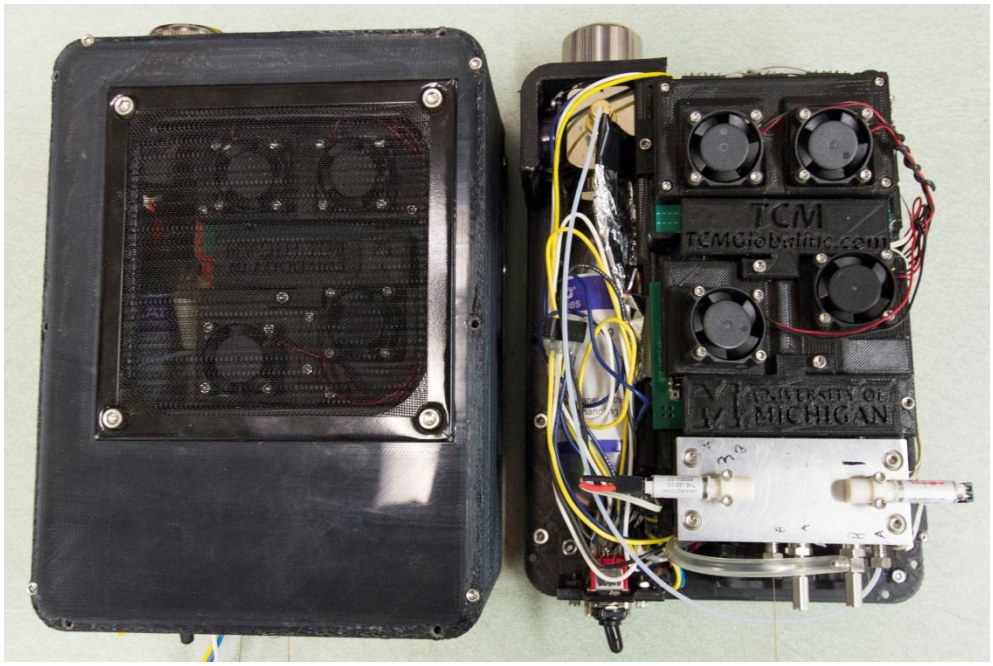

Figure 3.8. Fully assembled PEMM 2 prototype with and without top cover in place.

2.7 Phase 4/Aim 4

2.7.1. Introduction to Phase 1/Aim 1

Phase 4 addressed **Aim 4**, which was originally proposed to entail testing the PEMM 2 prototype(s) under a series of controlled mock-field testing scenarios, while being worn by volunteers, that would involve exposure to sets of mixtures that to allow the limits of resolution/performance to be defined, and use of the PEMM 2 as a personal monitor evaluated. Sets of VOC contaminants would be selected to be representative of exposures in actual workplaces. Measurements would be compared to those from standard reference methods over several weeks. As discussed in Section 2.6, some of the baseline performance testing originally proposed to be completed as part of Phase 3 were shifted to Phase 4, since it made sense to generate such data just prior to mock-field testing. Although several mock field tests were performed, fewer were run than were proposed, but testing is on-going.

The key performance criteria are follows: retention time stability, sensor-array response (and response pattern) stability, selectivity via chromatographic resolution and sensor-array response pattern differentiation, linear dynamic range, and limits of detection/recognition.

Specific benchmark values for the key criteria are as follows:

1) The retention times of all targeted VOCs should vary by < 5% (maximum range) under all operating conditions on the basis replicate analyses run on any particular day and on the basis of replicate analyses run over a 5 day period.
2) The response stability should be such that variations for all sensors in the array should be < 5% (max) on the basis of 5 replicate analyses run at a specific concentration > 5×LOD of each target on a single day.
3) In order to maintain accurate vapor recognition capabilities, a stable array response pattern is important. Thus, not only should individual sensor response remain stable, but the relative response variation among the array of sensors should also be maintained at <5% (max) so that the response pattern for each target VOC is stable enough for reliable vapor recognition/discrimination. The allowable variation in response pattern will be a function of the similarity of patterns of other VOCs from which each target must be differentiated.
4) In conjunction with the preceding analyses, the stability of the chromatographic resolution among VOCs in any mixture should be assessed. Of course, if retention times and response magnitudes are stable, the resolution, R, should also be stable. Variations should be << 5%.
5) The rejection of low volatility and high-volatility interferences should be checked with test atmospheres with representative (e.g., low-ppm) concentrations of VOCs from each volatility range.
6) µGC response linearity should be achieved over the critical concentration range of interest, such as 0.1×TLV to 5×TLV, for each target VOC. In keeping with response stability specifications, the goal is to maintain slope sensitivity for each sensor/VOC pair within 10% of that initial value. Some drift in slope sensitivities could be tolerated if all sensors drift in the same direction, such that response patterns are not significantly affected, because this could be addressed by periodic checks and the application of correction factors.
7) Assuming 100% capture and transfer efficiency by the microsampler (i.e., µPCF) the LOD achieved will be dependent upon the volume of air sampled, level of chemiresistor detector background noise, and the chemiresistor sensitivity to each target. Parameters will be optimized for LOD goals of 0.1×TLV at a maximum. Each sensor will yield an LOD. If complete chromatographic resolution is obtained, then the LOD can be based on a single sensor. If 'recognition' by virtue of the array response patterns is needed, then at least two sensors (ideally four) in the array must have detectable responses at the LOD.

8) In regard to RH and T compensation, very little water vapor is retained on the μPCF adsorbents and transferred downstream. Since RH may vary from 5-90%, this is the range over which tests of scrubber should be performed. Shifts in baseline temperature may affect adsorption capacities and also may shift retention times of early-eluting vapors. Since operation of the prototypes indoors is expected, the ambient temperature range should not deviate too far from 15-35 °C. Since the sensor array should be thermostatted, there should be little effect on its performance from shifts in ambient temperature.

In the rest of this section of the report, we provide descriptions of the methods used to assess the performance of one of the PEMM 2 prototypes. For coherence, we have included details about the component devices and some of the operating conditions, despite some of these details having presented in previous sections of the report. Following descriptions of the methods, we describe results of tests of a moderately complex mixture of 9 VOCs that were performed to confirm response linearity, limits of detection (LOD), retention time stability, peak-height and peak-area (i.e., sensitivity) stability over time periods ranging from hours to one week. We then focus on a more complex mixture analysis of 21 VOCs and on the use of response patterns in conjunction with retention time windows to facilitate vapor recognition and discrimination. Then results of mock-field tests are described.

Figure 4.1 shows a block diagram of the fluidic/analytical components of the PEMM-2 (Figure 1a) as well as photographs of the core microsystem components, comprising the separation microcolumn (μSC, Figure 1b), μPCF (Figure 1c), and micro-chemiresistor array (μCR, Figure 1d). More detailed diagrams of the flow paths for each different step (mode) of the sampling and analytical sequence of the PEMM 2 are given in the preceding section of the report (Figure 3.6).

2.7.2. Materials and Methods

2.7.2.1. Materials. The chemicals, benzene (BEN), trichloroethylene (TCE), n-heptane (C_7), 4-methyl-2-pentanone (MIBK), toluene (TOL), 2-hexanone (MBK), butyl acetate (BAC), ethylbenzene (ETB), m-xylene (XYL), 3-heptanone (EBK), n-nonane (C_9), α-pinene (PIN), cumene (CUM), n-propylbenzene (PPB), trimethylbenzene (TMB), n-decane (C_{10}), d-limonene (LIM), nitrobenzene (NBZ), n-undecane (C_{11}), trichlorobenzene.(TCB), and n-dodecane (C_{12}) were purchased from Sigma-Aldrich/Fluka (Milwaulkee, WI) or Acros/Fisher (Pittsburgh, PA) in >95% (most >99%) and used as received. The graphitized carbon adsorbents Carbopack X (C-X, 240 m^2/g), Carbopack B (C-B, 100 m^2/g) (Supelco, Bellefonte, PA) were sieved (212-250 μm) prior to loading into the μPCF. PDMS (OV-1) was purchased (Ohio Valley Specialty Co., Marietta, OH). MPNs (3.5-5 nm Au core diameter) derived from the following thiols were used as μCR interface films: n-octanethiol (C8), isooctyl-3-mercaptopropionate (EOE), methyl-6-mercaptohexanoate (HME) and 1-mercapto-(triethylene glycol) methyl ether (TEG). TEG was purchased (Nanoprobes, Yaphank, NY). Other MPNs were synthesized in-house. Pressurized He gas canisters (95 mL, 4.0 cm o.d. × 13 cm length, 2500 psi) and regulator were obtained from Leland (South Plainfield, NJ).

2.7.2.2. µPCF Description. The features of the µPCF chip (Figure 4.1c) were formed by deep reactive ion etching (DRIE) of Si. It has two ~4.7 µL cavities separated by a row of 150 µm o.d. pillars spaced by 150 um to segregate the two adsorbent materials. Similar rows of pillars at the inlet and outlet ports are used to retain the adsorbent materials within each cavity. Sidewall ports allowed for adsorbent loading (2.0 mg C-B, 2.3 mg C-X) by mild suction. A 120-µm thick anodically bonded Pyrex plate seals the cavities/channels. Fluidic ports accommodate 250 µm i.d. fused silica capillaries affixed with a flexible, high-temperature silicone adhesive (Duraseal 1531, Cotronics, Brooklyn, N.Y.). The fluidic inlet channel has a tee junction to permit vapor-sample loading through one branch and back-flushed injection through the other. A Ti/Pt resistive heater and resistance temperature detector (RTD) were patterned onto the backside. Finite-element modeling guided the heater design to minimize thermal gradients and power dissipation. The device was inverted, mounted on a custom printed circuit board (PCB) using epoxy (Hysol 1C, Rocky Hill, CT), and wire-bonded to the PCB bonding pads for electrical connections.

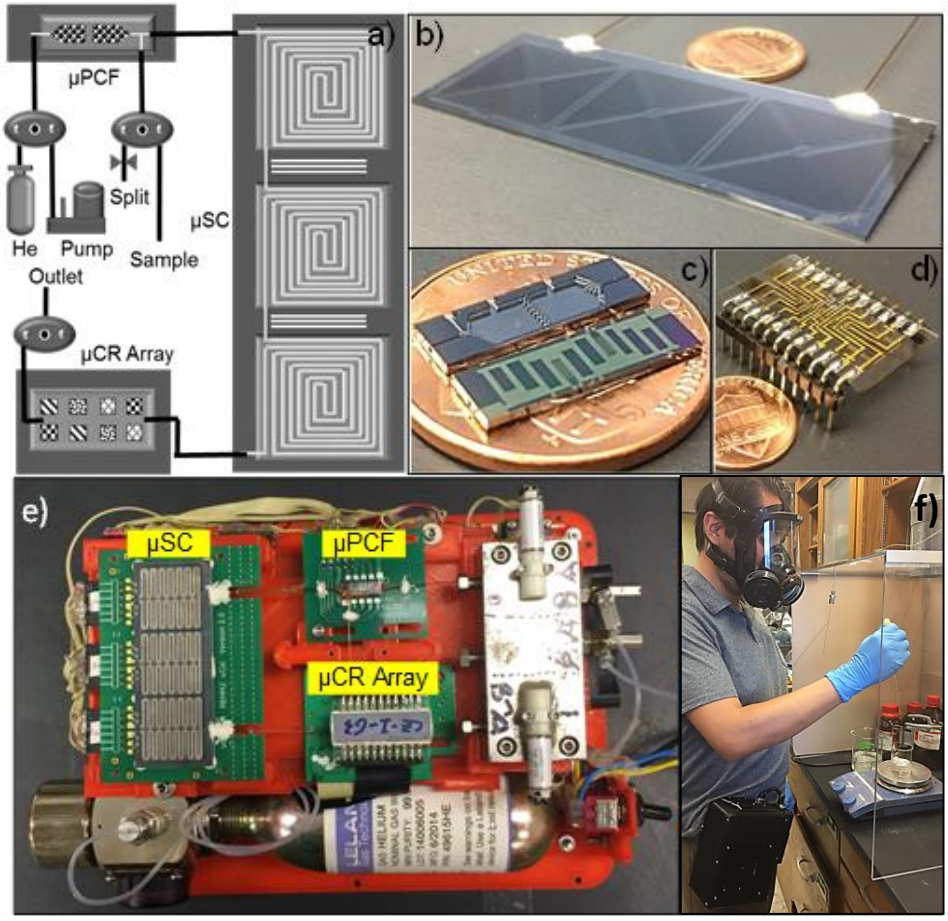

Figure 4.1. a) PEMM-2 fluidic layout diagram; b) micro separation column (µSC); c) micro preconcentrator/focuser (µPCF); d) micro chemiresistor array (µCR) array; e) fully assembled PEMM-2 with lid removed and f) belt-mounted PEMM-2 during mock field tests.

2.7.2.3. µSC Description. The separation microcolumn (µSC) column comprises a channel 6-m long on a single 7.1 × 2.7 × 0.075 cm Si chip which is divided into three 2-m long spiral segments. The DRIE-Si µcolumn (Figure 4.1b) channel has a 250 × 140 µm cross section with a Pyrex cap and 0.2 µm of wall-coated and cross-linked polydimethylsiloxane (PDMS) stationary phase. The chip has through-wafer DRIE slots between each segment and around the periphery of the chip for thermal isolation. The 3 independent backside Pt/Ti meander-line heaters were designed to minimize gradients and power dissipation. Interconnecting capillaries were epoxied into inlet/outlet expansion ports. The µcolumn was inverted and mounted on a custom PCB with Hysol, with wire bonds made to the heaters and RTDs.

2.7.2.4. µCR Array Description. The µCR array chip (Figure 4.1d) has 10 sets of Au/Cr (300/30nm) interdigital electrodes (IDEs) in a single row, with a central Au/Cr RTD, on a Pyrex substrate. Each µCR contains 27 pairs of electrodes, 5 µm wide, with 4 µm gaps, 210 µm overlap. A meander-line Pt/Ti heater was patterned on the backside. The Si lid has a 150 (d) × 350 µm (w) DRIE channel down the center (above the sensors). MPNs were drop-cast from solution to create (non-uniform) multilayer films with baseline resistances of 0.1 to 10 MΩ. Only 4 sensors were used per analysis. The lid was affixed to the substrate with double-sided tape (VHB, 3M, St. Paul, MN) and then Hysol. Interconnecting capillaries were epoxied into the fluidic ports. The lidded array was mounted on a custom PCB for electrical connections.

2.7.2.5. µSC Efficiency Testing. The separation efficiency of the column was determined at 30 ºC (GC oven) using n-octane as the probe. The headspace of a septum-seal vial contains methane and 2 drops of n-octane was injected by autosampler with the gas-tight syringe. The retention time (t_R) of n-octane was calculated as the difference of the elution times of the n-octane and methane. t_R and full width at half-maxima (fwhm) of eluting peaks were measured as a function of average N_2 carrier gas velocity where u was calculated as L/t_M, where L is the column length and t_M is methane elution time. The plate number, $N = 5.545(t_R/fwhm)^2$ and plate height, H = L/N, were calculated and the latter used to generate a Golay plot to determine the minimum plate height, H_{min}, and maximum plate count, N_{max}, at the optimal velocity.

2.7.2.6. System Integration and Prototype Assembly: Four printed circuit boards (PCBs) are stacked under the core micro-fabricated components, and contained the electronics necessary to run the system autonomously from a customized set of conditions programmed before the beginning of a run. The main hardware components included circuitry for the acquisition and control of the integrated resistance temperature detectors (RTD) and heaters, circuitry for data acquisition of the µCR array signals, and an embedded microcontroller system to provide feedback temperature control, system automation, and configurable operation. A PCB with the PIC32 micro-controller was used for the heating and cooling controls, device digital actuation, event scheduling, and user control execution. A PCB with the ARM micro-controller was specifically dedicated to the data acquisition of the µCR array signals, featuring highly accurate time stamping to provide ultra-low peak integration error during post-processing. A µCR amplifier PCB provided amplification, filtering and digital controlled baseline correction for the µCRs. A relay PCB contained solid state switches for heater, fans, pump and valves control, and provided power supply regulation.

Above these PCBs, the 3-D printed carrier substrate supports the key microfluidic components and a machined stainless-steel block serves as the primary flow manifold. It has surface ports and threaded holes machined to accept each of the three gasket sealed, 3-way latching solenoid valves (Model LHLA1221111H, Lee Co., Westbrook, CT, USA). The capillaries emanating from the µPCF and µCR array were connected to the appropriate ports on the manifold using zero-dead-volume fittings, and to the uSC with press-tight connectors (Supelco,

Bellefonte, PA). Above the microsystem components, fans were installed for cooling. A diaphragm mini-pump (NMP-09M, KNF Micro AG, Reiden, Switzerland) mounted beneath the manifold was used to collect the air samples. Two miniature needle valves (Beswick) were mounted between the inlet and outlet ports, respectively, on the manifold for manual adjustment of the sampling flow rate and injection split-flow ratio. Mounted on the floor of the enclosure, a pressurized helium canister (95 mL, purity >99.5%; 2500 PSI, Leland, South Plainfield, NJ, USA) and an adjustable regulator (50047, NR24, Leland, South Plainfield, NJ, USA) provided carrier gas flow. A set of battery packs were wired to the to the unit to provide power for the sustained operation of the instrument.

2.7.2.7. System Control, Data Acquisition and Processing: A Raspberry Pi (RP) mini-computer module (Raspberry Pi Foundation, Cambridge, UK) with wireless capability and independent (on-board) battery was mounted to the side of the PEMM 2 with Velcro to store the acquired data, and to serve as an interface between the embedded microcontroller and a remote laptop computer connected to the same local network. A custom web graphical user interface (GUI) was developed to allow access to the data from the laptop, providing user friendly controls and real time monitoring of the µCR array raw data.

Prior to any set of experiments, the operating parameters of the instrument, including, RTD calibration factors, temperature programs of the µPCF and µSC, total cycle duration, and timing of the modes of operation within a run were uploaded to the PEMM-2 system memory. An Excel worksheet macro was used to generate and embed this information into a machine readable configuration file, which then was used to reprogram the microcontroller via USB link.

To compensate for the large differences in baseline resistances of the µCRs, improve the signal-to-noise ratio (S/N), and maximize the dynamic range of the data acquisition system, a set of socketed reference resistors were installed to closely match the resistances of the µCRs. Finer tuning and periodic adjustments of eventual drifts were addressed by executing a subroutine residing in the micro-controller and controlling a set of digital to analog converters (DAC), which allowed cancelling of the resulting voltage offsets. Subroutine calls to the micro-controller were performed from the remote computer through a command-line interface, accessed via the RP. This interface also allowed manual actuation of components during system preparation, instructions on when to start a run, whether single or multiple runs were desired, and whether to store temperature data in the mini-computer for further analysis.

Raw chromatogram traces were stored as comma-separated values (CSV) files in the laptop. The measured voltage change (ΔV) for a given peak on a given sensor was converted to the corresponding resistance change (ΔR) then normalized by the baseline resistance (R_b). The converted chromatograms were then analyzed using OriginPro (Ver. 9.1, OriginLab, Northampton, MA). Calibration curve regression models and response patterns were generated in Excel. Monte Carlo simulations for chemometric vapor recognition analyses were implemented in visual basic via custom programs and principal comment analyses (PCA) were conducted in R (Ver. 3.4.0).

2.7.2.8. Test Sample Preparation. Test atmosphere of the VOCs were generated in 10-L Flex-foil® gas sample bags (Supelco Inc, Bellefonte, PA) by injecting the appropriate volume of each liquid and diluting with 8 L of N_2 metered into the bag with a dry gas meter. The concentration was confirmed by reference to calibration standards prepared from mixtures prepared in CS_2 over a range of injected masses that bracketed the range expected during instrument calibrations and analyzed by GC-FID using a 6-m OV-1 capillary column (7890B, Agilent Technol., Santa Clara, CA).

2.7.2.9. Mock Field Test Set-up. Mock field tests were conducted in a custom-made Plexiglass test chamber (61w × 60h × 43d cm) that sat on the benchtop. It was equipped with a ceiling mounted radial exhaust fan that vented to a nearby lab hood, the speed of which was controlled with a Variac. In addition a, small axial table fan was placed inside the chamber and used to mix the internal atmosphere for some experiments. A beaker that held the liquid VOC test mixtures was placed on a hotplate-stirrer, and heated/mixed as needed to generate vapors in the desired range during mock-field testing. A bench-scale GC with FID (7890B, Agilent) was used as reference instrument for PEMM-2 measurements. During a test, air samples were drawn through the 250 µL GC sampling loop by a small diaphragm pump via a small Teflon tube, while samples were collected with the PEMM-2 through a short fused-silica capillary. Both samples were collected in close proximity near the breathing zone of the researcher.

A number of different approaches were taken to generating vapors within the chamber for mock-field testing. Several trials were run over the course a few months. For the mock field testing results reported below, neat liquid TCE, MIBK, BAC XYL and C_{10} were mixed with a volume ratio of 2:3:4:5:10 into a 250 mL of beaker to account for the different vapor pressures. To induce vapor concentration fluctuations, different activities were performed by the researcher wearing the PEMM 2 every few minutes. Such activities included solvent transfer from one beaker to another via pipet; heating the beaker; adjusting the rates of both fans. These activities were undertaken separately or simultaneously to generate increased/decreased vapor concentrations.

Results and Discussion

2.7.2.10. µSC Efficiency. The Golay plot of HETP vs. linear velocity for the USC used in PEMM 2 (prior to installation) 27,000, or 4,500 plates/m for the 6-m column length. This is slightly better than was obtained with the µSC used for experiments related to zone-heated separations described in Section 2.5 In this report.

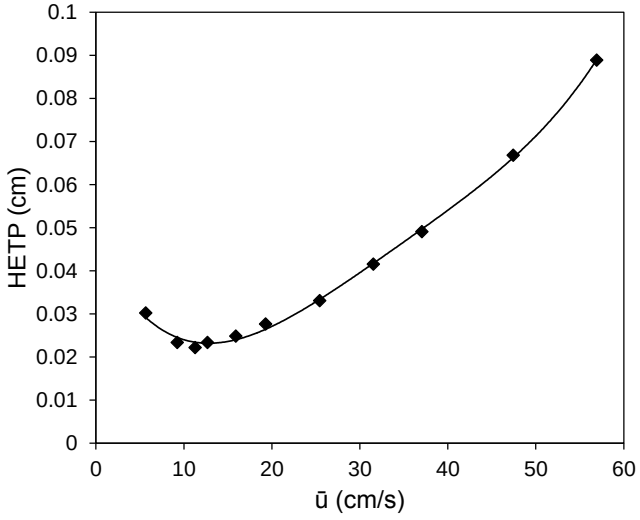

Figure 4.2. Golay plot generated using n-octane vapor as the probe at a column temperature of 30 °C (GC oven) and N_2 as carrier gas. H_{min} = 0.022 cm at average linear velocity of 11.3 cm/s. For the column length, L=6 m, this corresponds to a plate number, N_{max}=27,000 plates (i.e., 4,500 plates/m).

2.7.2.11. PEMM 2 Calibration and LODs. Numerous exploratory tests of instrument performance were conducted to confirm stable operation prior to conducting calibrations. For the latter, the 9 VOCs listed in Table 4.1 were selected because they span a wide range of vapor pressures and TLV values, they represent several different functional group classes, and a simple temperature program could be established to permit baseline separation of the peaks in a reasonably short time period (i.e., ~120 sec). Separation conditions were first established and the resulting chromatograms for each of the 4 MPN-coated sensors in µCR array are shown in Figure 4.3 (GC conditions are presented in the caption of Figure 4.3). As shown, good separation and good peak shapes were obtained in 120 sec, with some tailing evident in traces for the EOE and TEG sensors.

Table 4.1. List of 9 VOCs with corresponding vapor pressures (p_v), TLV-TWA values, and LODs with the PEMM-2 prototype.

Peak[a]	Compound	p_v[b] (kPa)	TLV[c] (ppm)	LOD (ppb)[d] C8	EOE	HME	TEG
1	BEN	12.6	0.5/2.5	149	139	595	551
2	C_7	6.13	400/500	175	109	174	298
3	TOL	3.78	20/--	111	104	455	428
4	MBK	1.55	5/10	89.1	59.8	57.8	170
5	BAC	1.53	50/150	65.0	48.6	90.3	225
6	XYL	1.01	100/150	92.4	77.9	326	327
7	EBK	0.533	50/75	104	50.4	57.7	216
8	PPB	0.456	--[e]	50.7	68.1	87.9	99.6
9	TMB	0.270	25/--	32.9	42.9	62.5	65.9

[a] Peak assignments are for the chromatograms in Figure 4.3 (acronyms for VOCs are defined in the text); [b] at 25 °C; [c] 8-hr TLV-TWA is listed first; if a TLV-STEL is assigned to a compound, then it is listed second; [d] Lowest detectable air concentration derived from mass-based LOD assuming a 5-mL air sample volume; Acronyms for the VOCs and MPNs are defined in the text; [e] No assigned TLV value.

Test atmospheres were prepared in 3 different Flexfoil bags containing the 9 VOCs at concentrations of 0.1×, 0.5×, and 2× TLV-TWA. By collecting samples of 5 mL and 10 mL (at 5mL/min), it was possible to span a 40-fold concentration range for each VOC. Duplicate samples were collected through a capillary connecting the test atmosphere to the PEMM-2 inlet (no pretrap was used for these tests) and analyzed.

The measured voltage changes were converted to normalized resistance changes, and peak area ($\Delta R/R_b \times s$) or peak height ($\Delta R/R_b$) was plotted versus injected mass (assuming 100% transfer efficiency). Linear regression with a forced-zero y intercept yield sensitivity values from the slopes of the lines. Calibration curves for peak area (A) and peak maxima (H_m) were linear with $R^2 > 0.99$ in all cases. Calibration curves for the 9 VOCs are presented in Figure 4.4.

Response patterns for each compound were generated by first normalizing the sensitivities (slope of the peak area vs. inj. mass) by dividing all sensitivities by the largest sensitivity for a given vapor. The relative sensitivity values were then plotted as a bar chart for each vapor. These are presented in Figure 4.5. Although patterns could be analyzed, we have elected to illustrate the value of pattern recognition for the more complex 21-VOC mixture analysis presented further below.

Limits of detection (LODs) were estimated from the slopes of the regression models (peak maxima vs. injected mass) of each sensor from the expression, 3σ/slope, where σ is the RMS baseline noise level from each sensor (values of σ, in units of $(\Delta R/R_b) \times 10^6$, were as follows: 42 (C8), 65(EOE), 125 (HME), and 70 (TEG*).* These mass-based LODs ranged from 1.2 ng (e.g., for TMB with the C8 sensor, among others) to 9.5 ng (for BEN with the HME sensor). In terms of air concentrations, the LODs are presented in Table 4.1 for all vapor-sensor pairs, assuming a 5-mL air sample. As shown, LODs ranged from 33 ppb for TMB with the C8 sensor to 600 ppb for BEN with the HME sensor. The LODs for a given VOC generally differ by < 4-fold among the sensors in the array.

Note that all compounds could be detected and recognized at < 0.1×TLV concentration levels (assuming a 5 mL of sample injection) with the exceptions of BEN with HME and TEG, for which the LODs were somewhat higher than 0.1×TLV. This is due to the low TLV for benzene and to its high vapor pressure and low polarity, both of which reduce the degree of partitioning into these polar MPN films. If the sample volume were increased to 10 mL, then the LOD would be < 0.1×TLV-TWA for all vapor-sensor pairs.

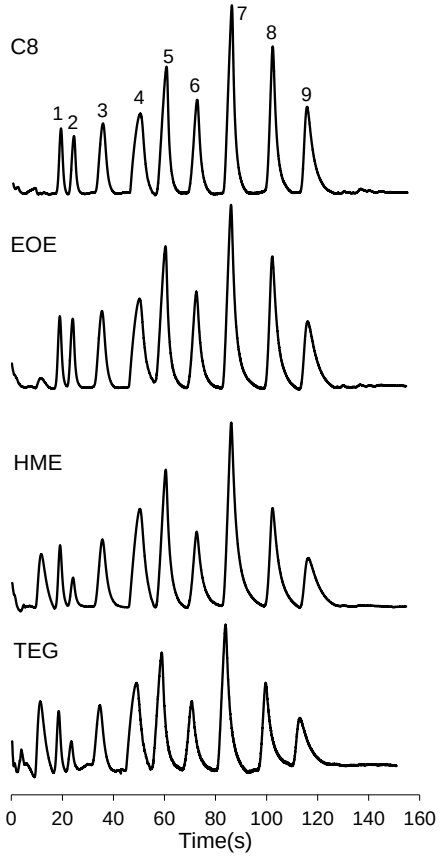

Figure 4.3. a) 9-VOC mixture chromatograms (voltage readings) from PEMM-2; Peak assignments: 0, water; 1, BEN; 2, C7; 3, TOL; 4, MBK; 5, BAC; 6, XYL; 7, EBK; 8, PPB; 9, TMB. Conditions: ~100 ppm of each vapor in the test atmosphere, 2.5 mL sample collected in 30 sec, splitless injection, 2 mL/min He carrier gas flow rate; Column temp program: 30 °C for 35 s, then 40 °C/min to 105 °C; sensor temperature: 30 °C.

2.7.2.12. PEMM-2 Medium-Term Response Stability. To characterize the stability of PEMM-2 responses, the relative standard deviation (RSD) of the peak areas, A, peak heights, H_m, and retention times, t_R, of the 9 VOCs were calculated from PEMM 2 responses collected from the same (bag) test-atmosphere and averaged over different time periods. For reference, a single analysis was performed with a reference bench-scale GC-FID (sample loop injection). Results are presented in Table 4.2 for the EOE sensor (other sensors gave comparable results, except for OPH which gave slightly more variability). First, six consecutive replicates were collected automatically, with each sampling and analytical cycle lasting 5 min. This is referred to as the 0.5 hr case in Table 4.2 To assess "intra-day" stability, a set of triplicate measurements was collected automatically early on one day and then another set of triplicate measurements was collected 8 hr later. The "inter-day" stability was assessed via the RSD of daily average values collected over 5 consecutive days.

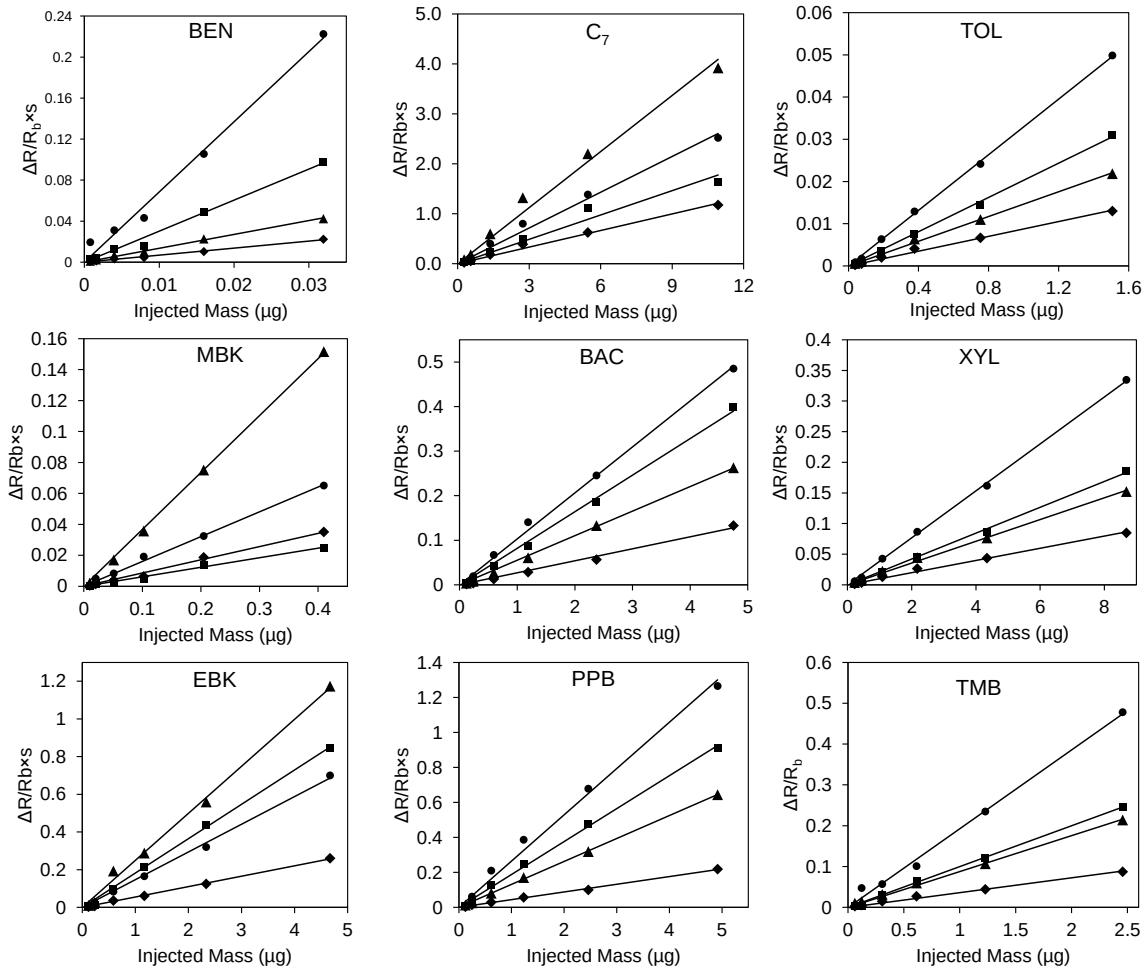

Figure 4.4. PEMM 2 calibration curves for 9 VOCs. Peak area is plotted as a function of injected mass for each sensor in the µCR array. The range of masses corresponds to a conc. Range of of 0.1 - 4×TLV, assuming a sample volume of 5 or 10 mL. Column temp. program: 30 °C for 35 s, then 40 °C/min to 105 °C; sensor temp.: 30 °C. Legend: EOE, circles; HME, triangles; C8, squares; TEG, diamonds.

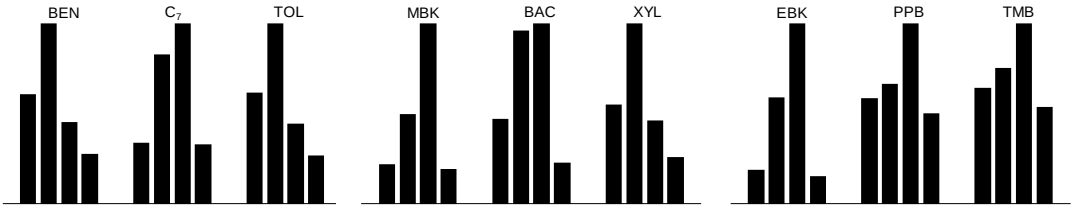

Figure 4.5. Normalized response patterns for 9 VOCs derived from the slopes of the calibration curves of peak area vs. injected mass. The response pattern is in the order (from right to left) of C8, EOE, HME and TEG for each vapor.

As shown, the short-term stability was quite high as reflected in the RSD values for all three measured parameters over 30 min: all were <2.5% and most < 2.0%. Intraday stability was also very high, with RSD values for all three parameters ≤ 5.0% in all cases and <2.0% in most cases. The interday stability was lower for all three parameters, with RSD values as high as 7.7% for peak area and 5-6% for peak height and retention time. Figure 4.6 shows that peak areas over the 5-day period did not show any significant systematic drift over time.

Notably, the reference GC-FID responses show comparable variability in peak area and peak height suggesting the variation may be attributable to small changes in ambient temperature or pressure in the laboratory causing changes in the absolute concentrations of the VOCs in the bag. Such environmental variations would also have a greater effect on retention times in the PEMM 2 than in the GC-FID because the latter had more precise control over oven temperature whereas the starting temperature of the former might be affected by ambient temperature fluctuations. Regardless, these results demonstrate that the PEMM 2 responses are sufficiently stable to provide reliable measurements.

Table 4.2. Stability of peak areas, peak heights, and retention times over different time periods. Data for the EOE sensor are shown.[a]

Relative Standard Deviation (RSD, %)												
VOC	PEMM-2 (EOE sensor)									GC-FID		
	0.5 hr (n=6)			intraday (n=6)			interday (n=5)[1]			interday (n=5)[2]		
	A	H_m	t_R	A	H_m	t_R	A	H_m	t_R	A	H_m	t_R
BEN	1.6	1.7	1.5	1.1-2.7	2.1-3.8	0.32-2.1	4.7	2.3	3.2	2.6	1.5	0.14
C7	2.1	2.4	0.73	1.8-2.6	2.0-3.2	0.26-1.4	5.4	3.5	1.3	3.2	1.3	0.17
TOL	2.0	1.4	0.59	1.1-1.9	2.5-4.0	0.23-1.5	7.7	2.8	4.9	3.2	0.81	0.17
MBK	1.0	1.2	0.47	0.58-1.9	3.0-5.0	0.23-1.2	4.1	4.5	5.9	6.1	2.4	0.10
BAC	1.2	1.7	0.59	0.71-1.8	2.1-5.0	0.15-0.91	3.1	5.0	5.0	7.6	2.6	0.13
XYL	1.0	1.3	0.71	0.59-1.7	1.4-3.7	0.23-0.52	4.9	4.0	5.1	4.7	2.9	0.22
EBK	1.4	0.68	0.77	0.15-0.88	0.76-3.1	0.031-0.33	3.0	4.5	4.5	4.8	2.3	0.75
PPB	0.80	0.96	0.84	0.44-1.6	0.77-1.8	0.064-0.31	2.7	5.6	4.8	8.3	4.0	0.19
TMB	1.2	2.4	0.95	0.33-1.8	0.97-1.4	0.12-0.31	2.8	5.3	5.8	6.3	2.8	0.24

[a] A = peak area, H_m = peak height (maximum), t_R = retention time; [b] based on 5 daily average values collected over 5 consecutive days; [c] based on a single daily analysis on each of 5 consecutive days (250 µL sample loop injection). All samples collected from the same (bag) test atmosphere.

2.7.2.13. 21-VOC Determination: Retention Time and Response Patterns. The next set of experiments focused on the analysis of a more complex 21-VOC mixture. A new µCR array was installed with the TEG-coated sensor replaced with an OPH-coated sensor. The influence of split-flow injection was explored and then the utility of combining a retention-time window approach to parsing the chromatogram with pattern recognition analysis of sensor array responses to achieve effective vapor recognition.

Figure 4.7 shows the set of chromatograms obtained from the 4 sensors in the µCR array after optimizing the separation conditions for the set of 21 VOCs. The vapor pressure range spanned by the analytes is from ~13 kPa (benzene) down to 0.03 kPA (n-dodecane), a 430-fold range. Among the analytes are VOCs representing 8 different functional group classes that include compounds found as air contaminants in many occupational settings. The test atmosphere was prepared by injecting liquid samples into a 10-L Flexfoil bag and diluting with 8 L of N2. Although not independently verified, the volumes of each liquid analyte injected would correspond to an airborne concentration of ~100 ppm assuming complete evaporation, with the exceptions of nitrobenzene (~50 ppm) and trichlorobenzene (~10 ppm). Retention times were checked during preliminary tests with subsets of compounds.

With the capillary pre-trap installed at the inlet of the PEMM 2 unit, a 1-min sample was collected at 5 mL/min, the µPCF was backflushed with He and heated to 225 °C in < 1 sec and maintained at that temperature for 40 sec. The flow rate through the µPCF was 9 mL/min and a 2:1 injection split was used (manually set with needle valve) so that the flow rate through the µSC was 3 mL/min. The temperature program used for the separation is given in the caption of Figure 4.7. The separation required about 150 sec for elution of all analytes.

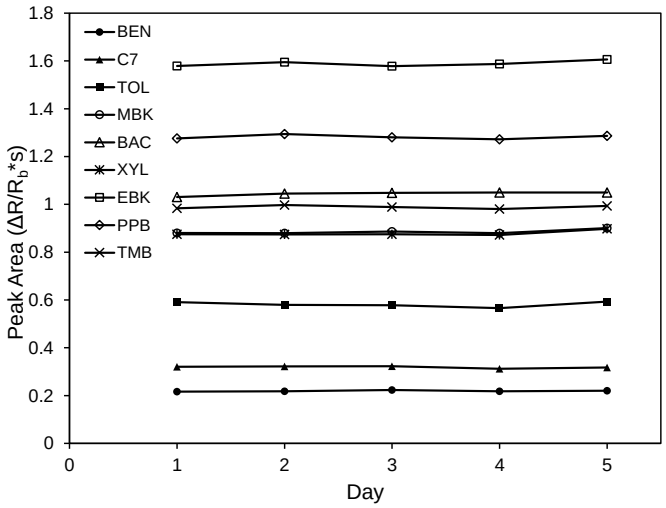

Figure 4.6. Stability of PEMM-2 responses to the components of a 9-VOC mixture as reflected in the daily avg peak area over 5 consecutive days (EOE sensor data shown). VOC acronyms are defined in the text.

Several features of the chromatograms are noteworthy. First, the peak shapes for 3 of the 4 sensors are quite good, the exception being the OPH sensor, which shows significant tailing that degrades the quality of the separation. This sensor coating was found later to have suffered from agglomeration of some of the MPNs, which slowed the response to vapor sorption/desorption. This notwithstanding, the overall separation quality is quite good, with near-baseline separation achieved for most analytes. Exceptions include the binary full or partial co-elutions for compounds 2&3, 4&5, and 8&9. Although broader peaks are expected for later

eluting compounds, it is clear that the rates of sorption/desorption in the sensor coatings contribute to the widening of the peaks for the later eluting compounds. As discussed below, the response patterns from the array can be used to help resolve the binary co-elutions.

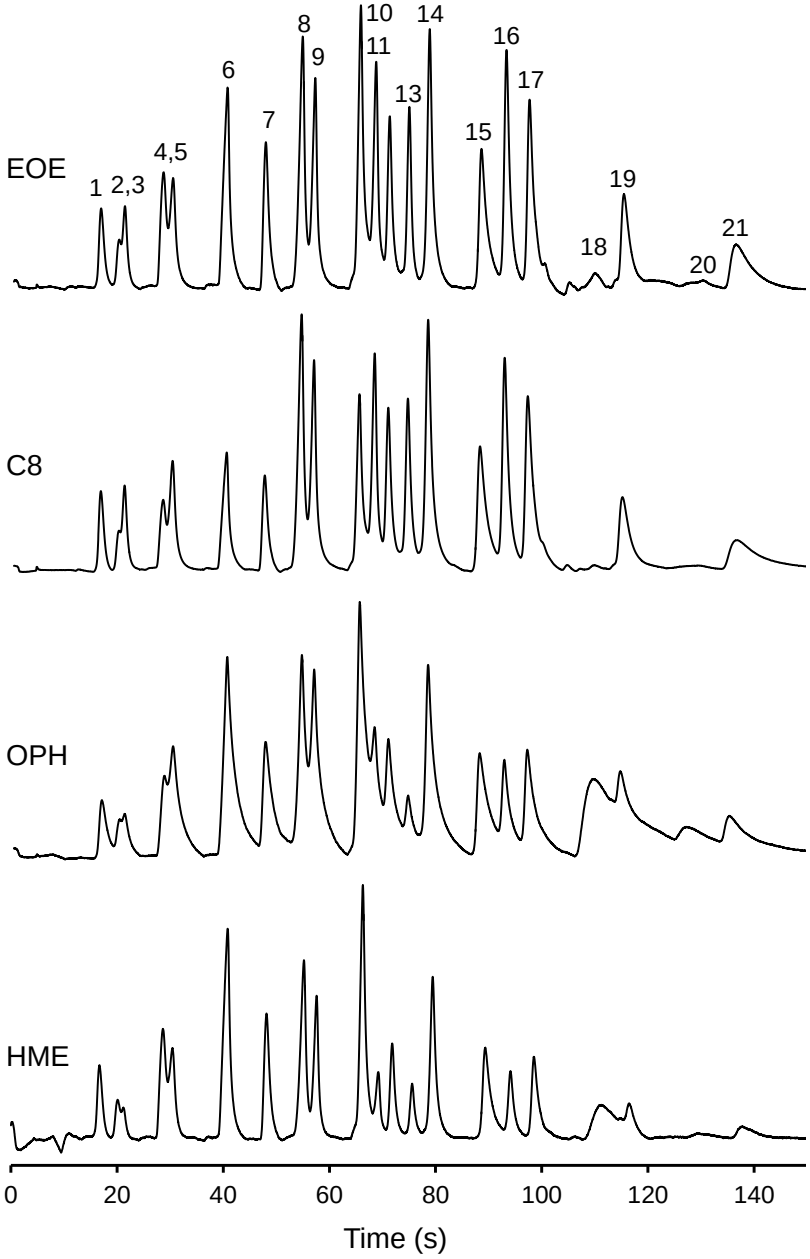

Figure 4.7. 21-VOC chromatograms from all 4 μCR-array sensors in PEMM-2 (baseline corrected). Conditions: ~100 ppm of each VOC (except nitrobenzene, ~50 ppm; trichlorobenzene, ~10 ppm) in bag; 5 mL/min sampling for 1 min; 2:1 split injection; μPCF, 225 °C for 40 s; μcolumn temperature program: 30 °C for 50 s, then 50 °C/min to 125 °C, and hold at 125 °C for another 16 s; 3 ml/min on column He flow; compounds, 1, benzene (BEN); 2, trichloroethylene (TCE); 3, n-heptane (C7); 4, 4-methyl-2-pentanone (MIBK); 5, toluene (TOL); 6, 2-hexanone (MBK); 7, butyl acetate (BAC); 8, ethylbenzene (ETB); 9, m-xylene (m-XYL); 10, 3-heptanone (3HEP); 11, n-nonane (C_9); 12, α-pinene (PIN); 13, cumene (CUM); 14, propylbenz. (PPB); 15, trimethylbenz. (TMB); 16, n-decane (C_{10}); 17, d-limonene (LIM); 18, nitrobenzene (NBZ); 19, n-undecane (C_{11}), 20, trichlorobenz.(TCB); 21, n-dodecane (C_{12}).

The decision to employ a 2:1 injection split was based on the improvement in resolution achieved, albeit at the expense of sensitivity (the split results in 2/3 of the sample mass being vented, see Section 2.4.5). Figure 4.8 compares the chromatograms obtained with and without the 2:1 split, using the EOE sensor output. Figure 4.8a shows the trace with 2:1 split injection and Figure 4.8b shows the trace with splitless injection. The split injection did not change the retention times of any compounds, but the full width at half maximum (*fwhm*) values decreased by 6-40%. The effect is much more prominent for the early eluting compounds. For example the *fwhm* of BEN (cmpd 1) decreases by 40% (from 1.7 sec to 1.0 sec) and that for MBK (cmpd 6) decreases by 20% (i.e., from 2.0 sec to 1.6 sec) with the split. Additional peak narrowing is observed but to progressively less of an extent out to PPB (cmpd 14, 6%) beyond which there is little or no impact.

Accordingly, the resolution of adjacent peaks is enhanced among peaks in the first part of the chromatogram but not in the latter part. So, the resolution ($R_S = \Delta t_R/w$, where w is average peak width at the base) of ethylbenzene (cmpd 8) and m-xylene (cmpd 9) increased 63%, from 0.8 to 1.3, with the split, but that for trimethylbenzene (cmpd 15) and n-decane (cmpd 16) remained at 2.1 despite the split. This is consistent with the fact that compounds with vapor pressures below ~ 0.5 kPa will benefit from on-column focusing regardless of the injection bandwidth, such that there is no benefit from a sharper injection. In contrast, the more volatile compounds do not get focused and are much more dependent on the injection bandwidth for ultimate resolution.

For fully or partially co-eluting peak pairs, it is possible to use the response patterns from the array to resolve both the identities of the compounds in the pair as well as their relative contributions to the composite peak area. To illustrate this, we chose three co-eluting pairs of peaks and applied principal component analysis (PCA) to the response patterns. For PCA, the responses from all 4 sensors to a compound are combined (vector sum) to create point a 4-dimensional space. Each compound can be represented in this way and the uniqueness of the response pattern is reflected by the Euclidean distance between the point for one compound and that of another. By projecting the locations of these points onto a plane that retains that distance, a so-called score plot can be produced. This can also be called a PCA plot because the two axes in such plots correspond to the projections of the first and second principal components from 4 dimensions onto 2 dimensions.

Figure 4.9 shows PCA plots for the four co-eluting pairs in Figure 4.8: TCE&C7, MIBK&TOL, ETB&XYL, and EBK&C9. For all of these compounds, R_s was <1.5. The oval region for each compound corresponds to the 95% confidence interval (CI) around the calibrated pattern as obtained from Monte Carlo (MC) simulations (see below). Also included is the region corresponding to the 95% CI of the 1:1 mixture of the two members of each pair (dashed lines). The scales on all four plots are the same such that the distances among the different regions are all comparable and reflect the uniqueness of the response patterns. As shown, for 3 of the 4 pairs, the pattern for one member could be readily resolved from that of the other member and from that of the mixture (i.e., 95% CI regions do not overlap). Thus, the compounds in these pairs could be identified and differentiated even if their peaks fully overlapped. The exceptional pair is that of ethylbenzene and m-xylene. That these cannot be resolved is expected because they are isomers and their partitioning behavior will be nearly identical for all sensors. Thus, only a composite measure of their exposure could be obtained.

Turning now to the chromatograms for the entire 21-VOC mixture, we first tried a naïve approach, which entailed performing a PCA on the entire data set without regard for chromatographic separations. In order to simulate response variability, we performed Monte Carlo simulations of the responses assuming each sensor's response could vary randomly by 5%. For each simulation an error-enhanced response pattern is obtained. By performing such simulations iteratively (i.e., n=500) a distribution of patterns is obtained from which a 95% CI can be derived and plotted. Figure 4.10a shows the results of performing such analysis for all

21 compounds. As shown, although the patterns from some compounds can be delineated, most cannot, and for the purpose of identifying all of the components of this mixture, this approach is not particularly useful.

A more effective approach, and the only feasible approach, is to divide the chromatogram into retention time windows containing fewer compounds and then doing vapor recognition on each subset individually, in sequence. The number of windows and the number of compounds in a given window is somewhat arbitrary. For illustration purposes, we chose to divide the chromatogram into 5 windows as indicated by the dashed lines in Figure 4.8. The MC-PCA analysis was conducted from the window 1 to window 5, individually.

Results are shown in Figure 4.10b-f. For the first window, which contains cmpds 1-5 (BEN, C7, TCE, MICBK, TOL) the pattern resolution is excellent, indicating that the identities of the compounds could be confirmed as long as all peaks are resolved. Certain binary co-elutions could be tolerated, as shown for the case of BEN&C7, but additional testing would be needed to assess which other co-eluting pair patterns could be resolved. In general, ternary co-elutions cannot be resolved with sensor array response data. What these data imply is that pattern recognition could be used to assign the identities of the compounds corresponding to all peaks in this window.

For the second window (Figure 4.10c), which contains cmpds 5-8, we see that MBK and BAC are sufficiently resolved from each other and both are resolved from ETB and XYL well enough for effective capor recognition. Per above, ETB and XYL are not resolved and could not be differentiated. For the third window (Figure 4.10d), which contains cmpds 9-12, all are well resolved. This is also true of the fourth window (Figure 4.10e), which contains cmpds 13-16. For the last wondow (Figure 4.10e), which contains cmpds 17-21, not surprisingly, undecane and dodecane are not resolved. Luckily, adjacent members of homologous series such as these are always well resolved chromatographically and the lower homologue always elutes first.

These results are very encouraging and illustrate the power of combining retention times with sensor-array response patterns for determining the members of complex mixtures of VOCs analyzed in this manner.

2.7.2.14. Mock Field Tests. Numerous preliminary trials were conducted to assess the performance of the PEMM 2 in a mock field testing scenario with different simple VOC mixtures. For all mock field test experiments, all manipulations of solvents were performed inside the make-shift chamber so that vapors could be exhausted before entering the general lab environment. The subject wore a properly fit-tested full-facepiece air-purifying respirator. The subject also wore the PEMM 2 on their belt and there was a short section of capillary extending from the inlet up to just below the breathing zone and several inches away from the body so it was capturing air samples from within the chamber perimeter (see Figure 4.1f). Prior to testing, the PEMM 2 was recalibrated by sampling a bag test atmosphere that was checked by GC-FID.

For the test results presented below, PEMM 2 sampled at 5 mL/min for 1 min, paused for a few seconds after valve switching to establish a steady flow of He gas through the system, the µPCF was heated to inject the mixture and 2 min was allowed for separation and detection, then 2 min was allowed for cool-down with backflushing of the pre-trap. The next cycle began automatically.

For the test results presented below, mixtures of 5 VOCs (TCE, MIBK, BAC, XYL, and C10) were prepared in a beaker in a volumetric ratio of 2:3:4:5:10, respectively, in consideration of the vapor pressures of the compounds as well as their relative sensitivities with the PEMM 2 sensor array. The chromatograms shown in Figure 4.11a were collected at t=50 min into the 60-min run. The larger peak for C10 reflects its higher concentration, resulting from a larger volume of C10 being added to the mixture (in spite of its lower vapor pressure). The inlet capillaries for the PEMM-2 and reference GC-FID were placed in close proximity (within 2 cm). Samples were continuously drawn through the PEMM-2 pre-trap and µPCF for 1 min and then

analyzed by the PEMM 2 unit over the next 4 min (including cool-down). During the 1-min sampling interval, 2 samples of just a few seconds duration (separated by ~30 sec) were drawn through the 250 µL of sample loop of the GC-FID and then injected and analyzed rapidly.

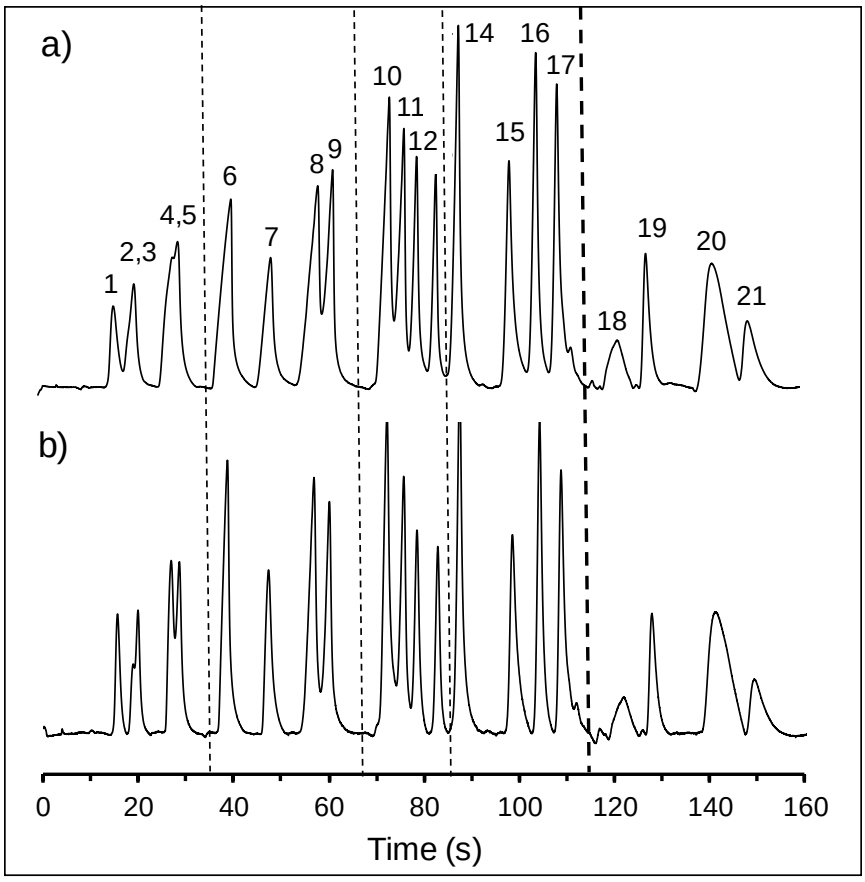

Figure 4.8. 21-VOC chromatograms from the EOE sensor in PEMM-2 with a) splitless and b) 2:1 split injection. Conditions: ~100 ppm of each VOC in bag; 5 mL/min sampling for 1 min; µPCF: 225 °C for 40 s; µcolumn temperature program: 30 °C for 50 s, then 50 °C/min to 110 °C, and hold at 110 °C for another 16 s. 3 ml/min µcolumn He flow rate maintained for both cases. Compound, 1, benzene (BEN); 2, trichloroethylene (TCE); 3, n-heptane (C7); 4, 4-methyl-2-pentanone (MIBK); 5, toluene (TOL); 6, 2-hexanone (MBK); 7, butyl acetate (BAC); 8, ethylbenzene (ETB); 9, m-xylene (XYL); 10, 3-heptanone (EBK); 11, n-nonane (C9); 12, α-pinene (PIN); 13, cumene (CUM); 14, propylbenzene (PPB); 15, trimethylbenz. (TMB); 16, n-decane (C10); 17, d-limonene (LIM); 18, nitrobenzene (NBZ); 19, n-undecane (C11), 20, trichlorobenzene.(TCB); 21, n-dodecane (C12)

Figures 4.11b-f show the concentrations derived from data collected by GC-FID (dash lines) and PEMM 2 (solid lines) over the course a 60-min period. The individual wearing the PEMM 2 engaged in several activities over this period in an attempt to vary the concentrations of the VOCs. These are described briefly in the caption of Figure 4.11. Each data point from the PEMM 2 is the average concentration determined from the 4 sensors, and the error bars are the standard deviations around each average. Each data point from the GC-FID is the average from the two samples collected and analyzed during the corresponding PEMM-2 sampling period, and the error bars are the standard deviation of those measurements.

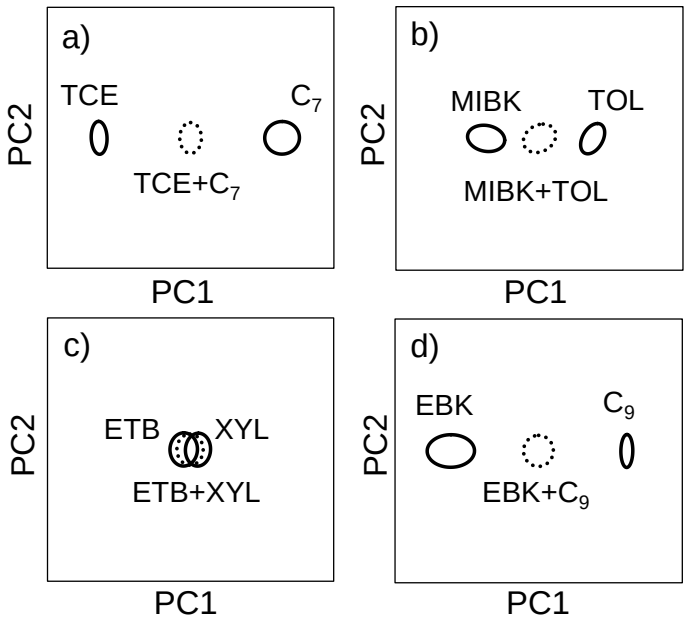

Figure 4.9. Principal component plots derived from μCR array response patterns for four pairs of fully or partially co-eluting compounds in Figure 4.7. Regions correspond to the 95% CI around the calibrated (library) pattern for each vapor. Dashed line regions correspond to the patterns for the 1:1 mixtures.

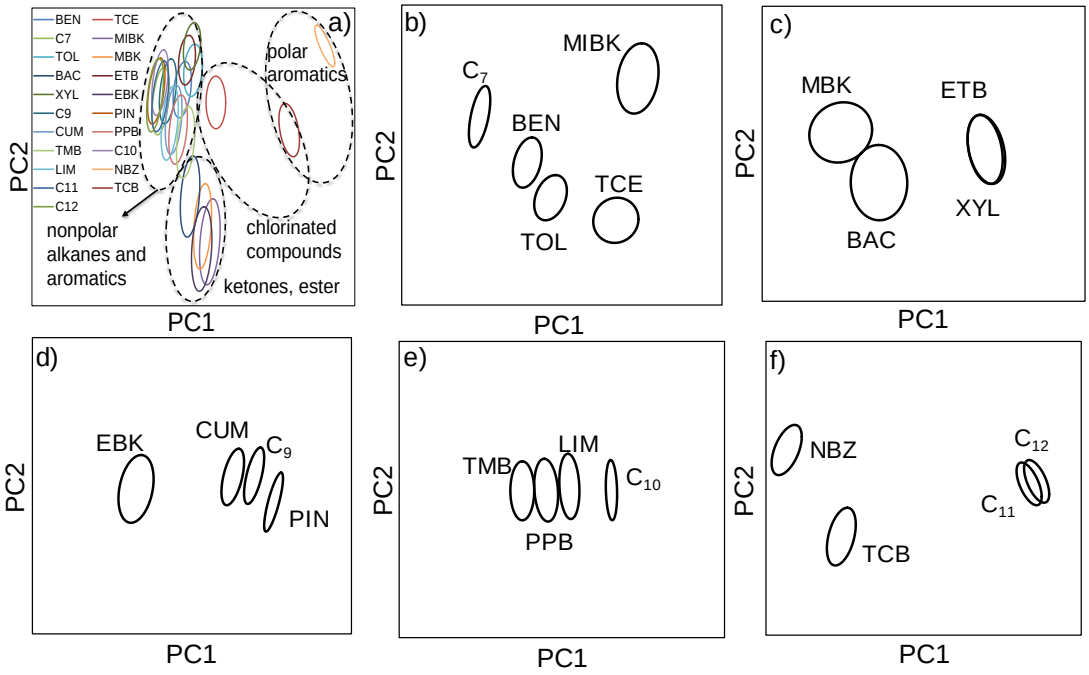

Figure 4.10. Principal component plots for retention-time windows divided by the dashed lines in Figure 4.8. a) PCA plot for 21 VOCs analyzed collectively; PCA plots of b) window 1 for cmpds 1-5; c) window-2 for cmpds 6-9; d) window-3 for cmpds 10-13; d) window-4 for cmpds 14-17; e) window-5 for cmpds 18-21. Regions assigned to each vapor represent the 95% CI around its pattern.

As shown, the concentration-time profiles of all VOCs except C10 were correlated. All VOC concentrations were low during the first 20 min period and then climbed to a local maximum at 30 min, which coincides with the activity of transferring some of the solvent mixture from the first beaker to a second one which was pre-heated on a hotplate. Concentrations then decreased and reached a local minimum at 40 min after removing the second beaker from the hotplate. They then rose again and reached a maximum at about 55 min as another transfer to a heated beaker took place. All but C10 then decreased again over the last 5 min period. We suspect that the C10, whose concentrations were much higher than those of the other vapors for most of the test, was not swept as readily from the breathing zone as the other vapors at the end of the test, hence its concentration continuing to rise. The ranges of concentrations spanned during the test were from 9-fold to 40-fold among the 5 VOCs.

In general, the PEMM 2 and GC-FID concentrations agreed quite closely, as shown in Figures 4.10b-f. Spatial and temporal variability can explain most of the differences observed, but the consistently higher values from the PEMM 2 for MIBK suggests a calibration error. The variability in GC-FID measurements indicated by the error bars reflects a fairly high degree of short-term fluctuations in air concentrations, which is less apparent in the C10 data due to its higher concentrations and the scale of the plot in Figure 4.11f. Variation in the concentrations measurements among the sensors in PEMM 2 for any given measurement was generally low, but reached as high 13% (RSD). We have not yet checked the impact such variability has on vapor recognition via the array response patterns, but such analyses are planned. Overall, these results indicate the PEMM 2 performed quite well for this short-term test.

2.7.2.15. Power Budget. The power required to run the PEMM 2 can be broken down into that required for the component parts. Table 4.3 presents a power budget for a typical operating cycle involving 1 min sampling, 2.5 min analysis (40-s desorption), and 3.5 min for cooling and reset. As shown the average power dissipation is only 6.1 W and the energy per cycle is only 2.2 kJ and the largest energy is consumed by the electronics. This suggests that a battery with a capacity of 49 W-hrs should permit operation for at least 8 hrs. Although testing to date has not extended beyond 1 hr, longer-term testing is planned in on-going efforts.

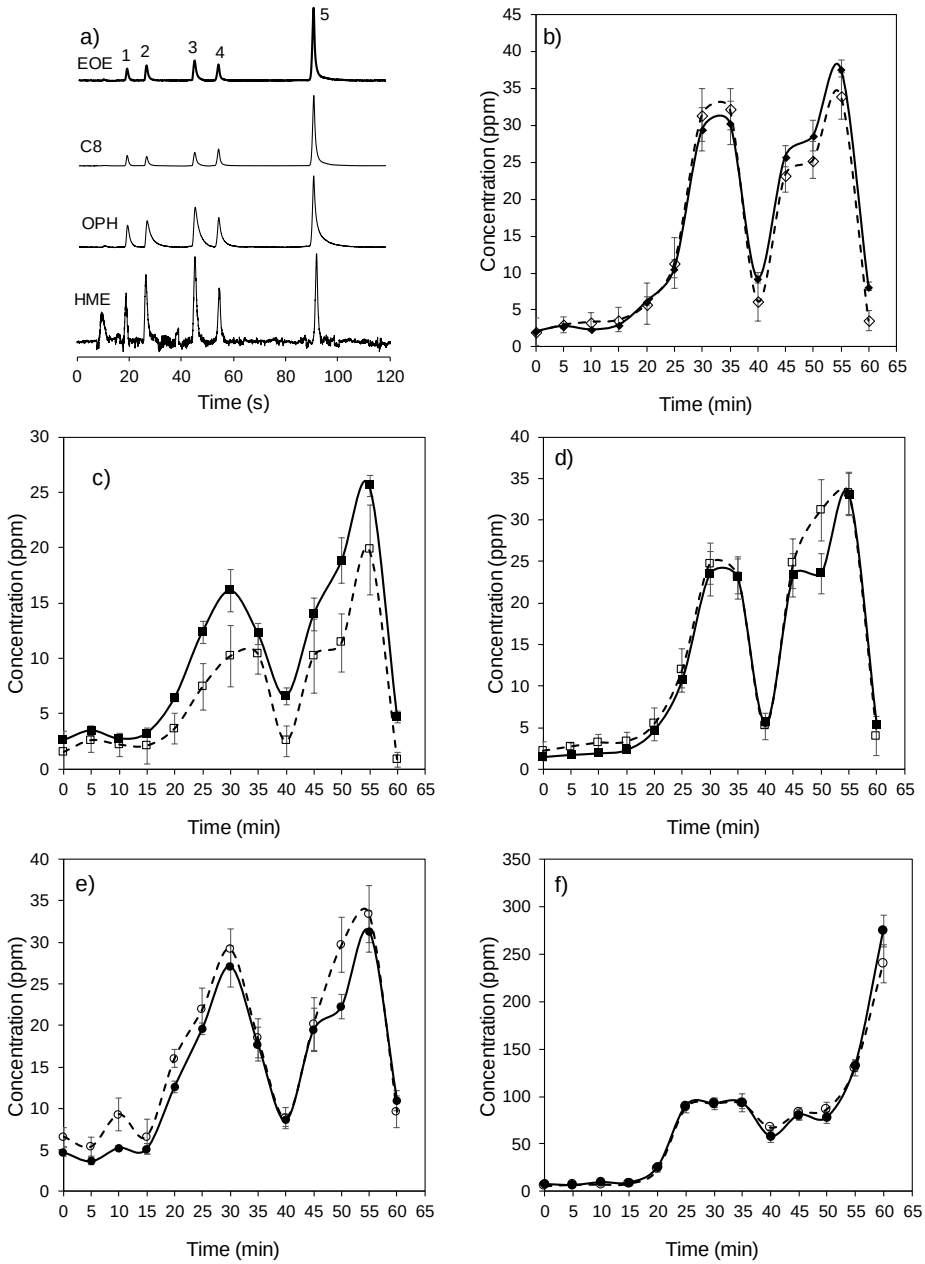

Figure 4.11. a) PEMM-2 mock field test chromatogram of 1,TCE; 2, MIBK; 3, BAC; 4, XYL; and 5, C_{10} collected at t= 50 min, and 60-min mock field testing results of PEMM 2 (solid line) and GC-FID (dash line) for b) TCE; c) MIBK; d) BAC; e) XYL; f) C10. Activities: 0-10 min, no activities; 10-20 min, solvent transfer (pipet) from one beaker to another at room temperature; 20-30 min, solvent transfer from beaker to pre-heated second beaker on hot plate set to 80°C; 30-40 min, repeat room temperature solvent transfer rom one beaker to another; 40-55 min, repeat solvent transfer from cool beaker to pre-heated beaker; 55-60 min: no activities.

Table 4.3. Power/Energy budget for PEMM 2 for a typical operating cycle.

	Voltage (V)	Current (A)	Power (W)	Quantity	Time (s)	Energy (J)	Avg. Power (W)
µPCF	16	0.126	2.01	1	40	80.4	0.22
µColumn	24	0.124	2.97	1	160	475	1.32
Pump	6	0.05	0.3	1	60	18	0.05
Latching valves	5	0.65	3.25	3	0.04	0.39	0.00
Cooling	12	0.05	0.6	3	210	378	1.05
Electronics	12	0.29	3.5	1	360	1260	3.50
					Total	**2212**	**6.14**

2.7.2.16. Concluding Remarks About the PEMM 2 Performance. The results of this study have demonstrated that the PEMM-2 prototype µGC is capable of direct, autonomous, multi-VOC personal (worker) exposure measurements at concentrations in the ppb-ppm range, bracketing the respective TLV-TWA or TLV-STEL values for numerous VOCs encountered in the workplace. The speed, reliability, sensitivity, dynamic ranges, low operating power, and vapor recognition capability define PEMM-2 collectively exceed the performance of other instrumentation currently available for industrial hygiene applications. On-going work is focused on testing more complex mixtures under mock-filed testing conditions and demonstrating that the instrument can operate unattended for 8hrs. .

Acknowledgments

The principal investigator wishes to express his heartfelt appreciation to the following individuals for their contributions to the success of this project. Without their hard work and ingenuity, none of this would have been possible. Mr. Junqi Wang and Mr. Nicolas Nuñovero worked on both the PEMM 1 and PEMM 2 prototypes, as well as on the segmented, aone-heated microcolumns. Dr. Jonathan Bryant-Genevier worked on PEMM 1 and the µPCF, and he, Dr. Sun Kyu Kim, and Dr. Kee Scholten worked on the application of multivariate curve resolution to sensor-array data. Prof. Katsuo Kurabayashi, Dr. Rob Nidetz, and Sanketh Buggaveet worked on thermal modeling and fabrication of microcolumns and µPCF devices. Dr. Willie Steinecker and Mr. Seth Peterson led the effort at VGC Chromatography (now TCM Global) to assemble and package the PEMM 2 prototypes and devise and implement the microcontrollers incorporated into the prototypes, and they were assisted by Mr. Bryan Brookover. Dr. Kee Scholten designed the µchemisresistor arrays, and both he and Mr. Changhua Zhan fabricated them. Mr. Bruce Kraay worked on developing and characterizing the pre-trap. Dr. Zhijin Lin worked on the band-trajectory modeling and testing of the segmented, zone-heated microcolumns. Dr. Lexuan Zhong helped with PEMM 2 calibrations and testing. Dr. Will Collin provided technical assistance with various critical aspects of prototype development. Dr. Chengyi Zhang and Dr. Lindsay Amos synthesized many of the nanoparticles. All microdevices were constructed in the Lurie Nanofabrication Facility at the University of Michigan. The principal investigator and colleagues are solely responsible for the content of this report.

References

1. H. Checkoway, Epidemiologic evaluation of exposure-effect relationships, in *Exposure Assessment for Epidemiology and Hazard Control,* edited by S. M. Rappaport and T. J. Smith, Lewis Publishers, Chelsea, MI, 1991, pp. 207-218.
2. S. M. Rappaport and L. L. Kupper, *Quantitative Exposure Assessment*, Rappaport and Kupper, Berkeley, CA, 2008.
3. ACGIH, *Documentation of the Threshold Limit Values and Biological Exposure Indices*, 7th Edition, ACGIH, Cincinnati, 2001 (with annual supplements).
4. S. O. Hansson, *Setting the Limit: Occupational Health Standards and the Limits of Science*, Oxford University Press, New York, 1999.
5. J. S. Ignatio, W. H. Bullock, Eds., *A Strategy for Assessing and Managing Occupational Exposures*, 3rd Ed., AIHA Press, Fairfield, VA, 2006.
6. S. A. Roach and S. M. Rappaport, "But they aren't thresholds - a critical analysis of the documentation of the threshold limit values", Am J. Ind. Med., 17, 727-753 (1990).
7. G. D. Nielsen, L. Hansen, P. Wolkoff, Chemical and biological evaluation of building material emissions. II. Approaches for setting indoor air standards or guidelines for chemicals, Indoor Air, 1997, 7, 17-32.
8. C.P. Wild. The exposome: from concept to utility. Internat. J. of Epid. 41 (2012), 24-32.
9. S.M. Rappaport. Implications of the exposome for exposure science. J. Expos. Sci. Environ. Epid. 21 (2011), 5-9.
10. E.A.C. Hubal. Biologically relevant exposure science for 21st century toxicity testing. Tox. Sci., 111 (2009), 226-232.

11. NIOSH website: http://www.cdc.gov/niosh/nora/councils/default.html (accessed June, 2012).
12. NIOSH website: http://www.cdc.gov/niosh/programs/expa/goals.html (accessed June, 2012).
13. ACGIH, *Threshold Limit Values & Biological Exposure Indices for 2012,* ACGIH, Cincinnati, OH, 2012.
14. NIOSH, *Pocket Guide to Chemical Hazards*, NIOSH, Cincinnati, OH, 2005/2007 (http://www.cdc.gov/niosh/npg/) accessed May, 2012).
15. Inficon Hapsite website: http://www.inficonchemicalidentificationsystems.com, accessed Jan., 2012.
16. Gasmet Technologies website: http://www.gasmet.fi/products accessed January, 2012.
17. J. L. Perkins, *Modern Industrial Hygiene - Vol. 1. Recognition and Evaluation of Chemical Agents*, 2nd Edition, ACGIH, Cincinnati, OH, 2008, Ch. 21.
18. C-J. Lu, W.H. Steinecker, W-C. Tian, M.C. Oborny, J.M. Nichols, M. Agah, J.A. Potkay, H.K.L. Chan, J. Driscoll, R.D. Sacks, K.D. Wise, S. W. Pang, E.T. Zellers, First-generation hybrid MEMS gas chromatograph, *Lab on a Chip*, 5, (2005) 1123-1131.
19. E.T. Zellers, S. Reidy, R.A. Veeneman, R. Gordenker, W.H. Steinecker, G.R. Lambertus, H. Kim, J.A. Potkay, M.P. Rowe, Q. Zhong, C. Avery, H. K. L. Chan, R. D. Sacks, K. Najafi, K.D. Wise, An integrated micro-analytical system for complex vapor mixtures, *Proc. Transducers '07,* Lyon, France, June 10-14, 2007, pp. 1491-1496.
20. H. Kim, W.H. Steinecker, S.M. Reidy, G.R. Lambertus, A. Astle, K. Najafi, E.T. Zellers, L.P. Bernal, P. Washabaugh, K.D. Wise, A micropump-driven high-speed MEMS gas chromatography system, *Proc. Transducers '07*, Lyon, France, June 10-14, 2007.
21. P.R. Lewis, R.P. Manginell, D.R. Adkins, R.J. Kottenstette, D.R. Wheeler, S.S. Sokolowski, D.E. Trudell, J.E. Bymes, M. Okandan, J.M. Bauer, R.G. Manley, G.C. Frye-Mason, Recent advancements in the gas-phase μchem Lab, *IEEE Sensors J*., 6, (2006) 784-795.
22. A. Keil, H. Hernandez-Soto, R.J. Noll, M. Fico, L. Gao, Z. Ouyang, and R.G. Cooks, Monitoring of toxic compounds in air using a hand held rectilinear ion trap mass spectrometer, *Anal. Chem.*, 80, (2008) 734-741.
23. E. Wapelhorts, J-P. Hauschild, J. Muller, Complex MEMS: a fully integrated TOF micro mass spectrometer, *Sens. Actuators. A*, 138, (2007) 22-27.
24. C. Charlton, F. de Melas, A. Inberg, N. Croitoru, B. Mizaikoff, Hollow-waveguide gas sensing with room-temperature quantum cascade lasers, *IEE Proc. Optoelect*., 150, (2003) 306-309.
25. S. Zampolli, I. Elmi, J. Sturmann, S. Nicoletti, L. Dori, G.C. Cardinali, Selectivity enhancement of metal oxide gas sensors using a micromachined gas chromatographic columns, *Sens. Actuators B*, 105, (2005) 400-406.
26. F. Lee, G. Zhou, H. Yu, F. S. Chau, A MEMS-based resonant-scanning lamellar grating Fourier transformer micro-spectrometer with laser reference system, Sensors and Actuators A: Physical, 149, (2009), 221-228.
27. R.A. Miller, E.G. Nazarov, G.A. Eiceman, A. T. King, A MEMS radio-frequency ion-mobility spectrometer for chemical vapor detection, *Sens. Actuators. A,* 91, (2001) 301-312.
28. J. Moxom, P.T. A. Reilly, W.B. Whitten, J.M. Ramsey, Analysis of VOCs in air with a micro ion trap mass analyzer, *Anal. Chem.,*75, (2003) 3739-3743.
29. A. de Mello, On-chip chromatography: the last twenty years, *Lab on a Chip,* 2, (2002) 48N-54N.
30. F. Tsow, E. Forzani, et al, 2009. A wearable and wireless sensor system for real-time monitoring of toxic environmental volatile organic compounds. IEEE Sens. J. 9 (2009), 1734-1740.

31. R.A. Iglesias, F. Tsow, R. Wang, E.S. Forzani, and N. Tao. Hybrid separation and detection device for analysis of benzene, toluene, ethylbenzene, and xylenes in complex samples. Anal. Chem. 81 (2009), 8930-8935.
32. I. Negi, F. Tsow, K. Tanwar, L. Zhang, R.A. Iglesias, C. Chen, A. Rai, E.S. Forzani, and N. Tao. Novel monitor paradigm for real-time exposure assessment. J. Exp. Sci. Environ. Epid. 21 (2011), 419-426.
33. C. Chen, K.D. Campbell, I. Negri, R.A. Iglesias, P. Owens, N. Tao, F. Tsow, and E.S. Forzani. A new sensor for the assessment of personal exposure to volatile organic compounds. Atmos. Environ. 54 (2012), 679-687.
34. *Special Issue, Chemical Reviews*, 100, (2000).
35. *Special Issue, Chemical Reviews*, 108, (2008).
36. J. Park, W. A. Groves, and E. T. Zellers*," Vapor recognition with small arrays of polymer-coated microsensors -- a comprehensive analysis " *Anal. Chem*. 71, (1999), 3877-3886.
37. M.D. Hsieh, E.T. Zellers, Limits of recognition for simple vapor mixtures determined with a microsensor array, *Anal. Chem.,* 76, (2004) 1885-1895.
38. C. Jin, P. Kurzawski, A. Hierlemann, E.T. Zellers, Evaluation of multitransducer arrays for the determination of organic vapor mixtures, *Anal. Chem.,* 80, (2008) 227-236.
39. C. Jin and E. T. Zellers , "Limits of Recognition for Binary and Ternary Vapor Mixtures Determined with Multi-Transducer Arrays" *Anal. Chem*., 80, (2008),7283-7293.
40. P. Kurzawski, C. Hegleitner, A. Hierlemann, "Detection and Discrimination Capabilities of a Multitransducer Single-Chip Gas Sensor System", 78, (2006) 6910-6920.
41. R. Potyrailo, W. Morris, Multianalyte Chemical Identification and Quantitation Using a Single Radio Frequency Identification Sensor, *Anal. Chem*, 79, (2007), 45-51.
1. 42. S.C. Terry, H. Jermann, J. Angel, A gas chromatograph air analyzer fabricated on a silicon wafer, *IEEE Trans. Electron Dev., 26,* (1979) 1880-1887.
43. S.K. Kim, H. Chang, E.T. Zellers, Prototype micro gas chromatograph for breath biomarkers of respiratory disease, *Proc. Transducers '09*, Denver, CO, June 21-25, 2009, pp. 128-131.
44. G. Serrano, H. Chang, E. T. Zellers, A micro gas chromatograph for high-speed determinations of explosive vapors, *Proc. Transducers '09*, Denver, CO, USA, June 21-25, 2009, pp. 1654-1657.
45. S. K. Kim, H. Chang, E. T. Zellers*, Microfabricated gas chromatograph for the selective determination of trichloroethylene vapor at sub-parts-per-billion concentrations in complex mixtures," *Analytical Chemistry*, 2011, 83, 7198-7206.
46. S. K. Kim, D. R. Burris, H. Chang, J. Bryant-Genevier, and E. T. Zellers*, "Microfabricated Gas Chromatograph for On-Site Determinations of Trichloroethylene in Indoor Air Arising from Vapor Intrusion, Part I: Field Evaluation," Environmental Science and Technology, 46, 6065-6072,2012
47. S. K. Kim, D. R. Burris, J. Bryant-Genevier, K. A. Gorder, E. M. Dettenmaier, and E. T. Zellers*, "Microfabricated Gas Chromatograph for On-Site Determinations of TCE in Indoor Air Arising from Vapor Intrusion Part II: Spatial/Temporal Monitoring, Environmental Science and Technology, 46, 6073-6080,2012.
48. SEER Technology, http://www.seertechnology.com/astech.php accessed June, 2012
49. Torion Technologies, http://www.torion.com/products, accessed June, 2012
50. Center for Wireless Integrated Microsystems website: http://www.wimserc.org
51. Q. Zhong, W. Steinecker, E. T. Zellers, "Characterization of a High-Performance Portable GC with a Chemiresistor Array Detector," *Analyst*, 134, 283-293, 2009.
52. W. H. Steinecker, S. K. Kim, F. I. Bohrer, L. Farina, C. Kurdak, E. T. Zellers, "Electron-Beam Patterned Monolayer-Protected Gold Nanoparticle Interface Layers on a Chemiresistor Vapor Sensor Array," *IEEE Sensors J.*, 11(2), (2011), 469-480.

53. E. Covington, F. I. Bohrer, C. Xu, E. T. Zellers, and C. Kurdak, “Densely Integrated Array of Chemiresistor Vapor Sensors with Electron-Beam Patterned Monolayer-Protected Gold Nanoparticle Interface Films,” *Lab On A Chip*, (2010), 10, 3058-3060
54. C. Jin and E. T. Zellers, “Chemometric Analysis of Gas Chromatographic Peaks Measured with a Microsensor Array: Methodology and Performance Assessment,” *Sensors and Actuators B – Chemical*, 139, (2009), 548-556.
55. C. J. Lu, W. C. Tian, W. H. Steinecker, A. Guyon, M. Agah, M. C. Oborny, R. D. Sacks, K. D. Wise, S. W. Pang, and E. T. Zellers, *Proc. of the 7th International Conference on Miniaturized Systems for Chemistry and Life Sciences, μTAS ’03,* Squaw Valley, CA, 2003, pp. 411-415.
56. E. T. Zellers, W. H. Steinecker, G. R. Lambertus, M. Agah, C. J. Lu, H. K. L Chan, J. A. Potkay, M. C. Oborny, J. M. Nichols, A. Astle, H. S. Kim, M. P. Rowe, J. Kim, L. W. DaSilva, J. Zheng, J. J. Whiting, R. D. Sacks, S. W. Pang, M. Kaviany, P. L. Bergstrom, A. J. Matzger, Ç. Kurdak, L. P. Bernal, K. Najafi, and K. D. Wise, *Proc. Solid-State Sensors, Actuators, and Microsystems Workshop*; Hilton Head, SC, 2004, pp. 61-66.
57. G.R. Lambertus, C.S. Fix, S.M. Reidy, R. Miller, D. Wheeler, E. Nazarov, R.D. Sacks, Silicon microfabricated column with microfabricated differential mobility spectrometer for GC analysis of volatile organic compounds, *Anal. Chem*., 77, (2005) 7563-7571.
58. W.C. Tian, H. K. L. Chan, C. -J. Lu, S. W. Pang, and E. T. Zellers, “Microfabricated Multi-stage Preconcentrator-Focuser for A Micro Gas Chromatograph”, *Journal of Microelectromechanical Systems*, 14, (2005) 498-507.
59. M. Agah, J. A. Potkay, G. R. Lambertus, R. D. Sacks, K. D. Wise, High performance temperature-programmed microfabricated gas chromatography columns, *IEEE J. Microelectromech. Syst.*, 14 (5), (2005) 1039-1050.
60. S. Reidy, G. Lambertus, J. Reece, R. Sacks, High-performance, static-coated column silicon microfabricated columns for gas chromatography, *Anal. Chem*., 78, (2006) 2623-2630.
61. J.A. Potkay, G.R. Lambertus, R.D. Sacks, K.D. Wise, A low power pressure and temperature-programmable micro gas chromatography column, *J. Microelectromech. Syst*., 16, (2007) 1071-1079.
62. S.-J. Kim, S. M. Reidy, B. P. Block, K. D. Wise, E. T. Zellers, and K. Kurabayashi, “Microfabricated Thermal Modulator for Comprehensive Two-Dimensional Micro Gas Chromatography: Design, Thermal Modeling, and Preliminary Testing,” *Lab On A Chip*, 10, (2010),1647 – 1654.; b) S. J. Kim, G. Serrano, K. D. Wise, K. Kurabayashi, E. T. Zellers, Evaluation of a microfabricated thermal modulator for comprehensive two-dimensional gas chromatography,” *Analytical Chemistry*, *83*,5556–5562, 2011.
63. J. H. Seo, S. K Kim, E. T. Zellers, and K. Kurabayashi, “Microfabricated integrated sampler-injector (MISI) for micro gas chromatography,” Proc. MEMS Conference, Cancun, Mexico, January, 2011, pp. 825-828.
64. A.D. Radadia, R.I. Masel, M.A. Shannon, J.P. Jerrell, and K.R. Cadwallader, Micromachined GC columns for fast separation of organophosphonate and organosulfur compounds, *Anal. Chem*., 80, (2008) 4087- 4094.
65. M.A. Aareian-Jahromi, M. Ashraf-Khorassani, L. Taylor, M. Agah, "Design, Modeling, and Fabrication of MEMS-Based Multicapillary Gas Chromatographic Columns", JMEMS., 18, 28-37, 2009
66. S. Ali, M. Ashraf-Khorassani, L. Taylor, M. Agah, "MEMS-based semi-packed gas chromatography columns", Sens. & Actuators B., 141, 309-315, 2009
67. S. Zampolli, I. Elmi, F. Mancarella, P. Betti, E. Dalcanale, G. C. Cardinali and M. Severi, “Real-time monitoring of sub-ppb concentrations of aromatic volatiles with a MEMS-enabled miniaturized gas-chromatograph”, Sens. Actuator, B., 141, (2009), 322-328.

68. M. Li, E.B. Meyer, H.X. Tang, S.J. Aldridge, H.C. McCaig, J.J. Whiting, R.J. Simonson, N. Lewis, M. Roukes, “Nanoelectromechanical Resonator Arrays for Ultrafast, Gas-Phase Chromatographic Chemical Analysis”, *Nano Letters*, 10, (2010) 3899-3903.
69. C2V website: http://www.c2v.nl/ accessed May, 2012
70. SLS Micro Technology website: http://www.sls-micro-technology.de/ accessed May, 2012
71. Siemens MicroSAM website: http://www.automation.siemens.com/w1/process-analytics-for-standard-process-applications-6693.htm, accessed May, 2012
72. Defiant Technologies website: http://www.defiant-tech.com/ (accessed May, 2012)

Publications and Presentations

Journal Articles

1. Wang J, Bryant-Genevier J, Nuñovero N, Zhang C, Kraay B, Zhan C, Scholten K, Nidetz R, Buggaveeti S, Zellers ET: [2018] Compact Prototype Microfabricated Gas Chromatographic Analyzer for VOC Mixtures at Typical Workplace Concentrations. Microsystems and Nanoengineering 4: 17101.
2. Lin Z, Nuñovero N, Wang J, Nidetz R, Buggaveeti S, Kurabayashi K, Zellers ET: [2018] A Zone-Heated Gas Chromatographic Microcolumn: Energy Efficiency. Sensors and Actuators B: Chemical 254: 561–572.
3. Bryant-Genevier J, Zellers ET: [2015] Toward a Microfabricated Preconcentrator-Focuser for a Wearable Micro-scale Gas Chromatograph. Journal of Chromatography A 422: 299-309.
4. Bryant-Genevier J, Scholten K, Kim SK, Zellers ET [2014] Multivariate Curve Resolution of Co-eluting Vapors from a Gas Chromatograph with Microsensor Array Detector. Sensors and Actuators B: Chemical 202: 167-176.

Proceedings Papers

2. Wang J, Nuñovero N, Zhan C, Nidetz R, Steinecker WH, Peterson SJ, Brookover BM, Zellers ET: [2017] Microscale Gas Chromatography with Microsensor Array Detection: Challenges and Prospects. Proc of Eurosensors 2017, Paris, France, 633-636, September 3-6.
3. Wang J, Lin Z, Nuñovero N, Nidetz R, Buggaveeti S, Kurabayashi K, Steinecker WH, Zellers ET: [2016] A Wearable MEMS Gas Chromatograph for Multi-Vapor Determinations. Procedia Engineering (Proc of Eurosensors 2016), Budapest, Hungary, 1398-1401, September 4-7.

Dissertations

1. Bryant-Genevier J: [2016] Development of Micro-scale Gas Chromatographic Systems and Chemometric Algorithms for Near-real-time Personal Monitoring of Exposures to Volatile Organic Compounds in the Workplace, Ph.D. Dissertation, University of Michigan.
2. Wang, J: [2018 (expected)] Development of Micro Gas Chromatographic Systems (µGC) for Airborne and Aqueous Volatile Organic Compound (VOC) Determinations, Ph.D. Dissertation, University of Michigan.

Invited Presentations

1. E. T. Zellers, J. Wang, N. Nuñovero , C. Zhan, R. Nidetz, W. H. Steinecker, S. J. Peterson, B. M. Brookover, “Microscale Gas Chromatography with Microsensor Array Detection: Challenges and Prospects,” **Invited Plenary Presentation**, *Eurosensors 2017*, Paris, France, September 3th-6th, 2017.
2. E.T. Zellers, J. Wang, N. Nunovero, Z. Lin, J. Bryant, C. Zhan, W. Collin, K. Scholten, R. Nidetz, S. Buggaveeti, K. Kurabayashi, W. Steinecker, “Multi-Vapor Determinations with a Belt-Mountable Microscale Gas Chromatograph (µGC) (Application to Worker Exposure Assessment),” **Invited Presentation,** *Symposium on Integrated Micro-Scale Chemical Analyzers, Pittcon ‘17*, Chicago, IL, March 5th-9th, 2017.

3. E. T. Zellers, J. Wang, J. Bryant-Genevier, N. Nuñovero, W. Collin, Z. Lin, "Wearable Microsystem for Continuous, Quantitative Measurements of Multi-VOC Exposures," **Invited Presentation**, *Roundtable on Wearable Sensors in Occupational Safety and Health Practice, Am. Indust. Hyg. Confer. and Expos.*, Baltimore MD, May 22-26, 2016.
4. Ted Zellers, Jon Bryant-Genevier, Nico Nunovero, Junqi Wang, Will Collin, Kee Scholten, Sun Kim, C. Zhang, R. Nidetz, S. Buggaveeti, K. Kurbayashi, "Toward a Personal Exposure Monitoring Microsystem (PEMM) for Multi-VOC Mixtures (a Wearable Microfabricated Gas Chromatograph: µGC)" , **Invited Presentation**, Michigan Industrial Hygiene Society, Mini Conference, Troy, MI, October 7th, 2015.

Contributed Presentations

- J. Bryant-Genevier, N. Nunovero, and E. T. Zellers. Toward a wearable micro-scale gas chromatograph for quantitative analysis of VOC mixtures. ***I****nvited*, EPA Air Sensors 2014, Raleigh, NC, June 9th-10th, 2014.
- J. Bryant-Genevier, S.K. Kim, E.T. Zellers. Chemometrics for µGC; deconvoluting micro sensor array responses, *poster presentation*, Pittcon'14, Chicago, IL, March 2-6, 2014.
- J. Bryant-Genevier, S. K. Kim, and E. T. Zellers. Quantitative Analysis of Multi-VOC Mixtures by Micro-Scale Gas Chromatography (µGC), *poster presentation*, EPA Air Sensors 2013, Raleigh, NC, March 19th-20th, 2013.
- J. Wang, N. Nunovero, R. Nidetz, W. Steinecker, E.T. Zellers, A Belt-Mounted Micro Gas Chromatograph Prototype for Autonomous Determinations of VOC Mixtures, *oral presentation*, Pittcon'18, , Orlando, FL, Feb 27th- March 1st, 2018.
- J. Wang, N. Nunovero, W. Steinecker, E. T. Zellers, A Wearable Microfabricated Gas Chromatography for Trace-Level Volatile Organic Compound Determinations*, poster presentation*, WIMS IAB Meeting, Ann Arbor, MI, Sep. 28th- 30th, 2017.
- J. Wang, N. Nuñovero, Z. Lin, Z, R. Nidetz, S. Buggaveeti, K. Kurabayashi, W. H. Steinecker, E. T. Zellers, Belt-Mounted Microfabricated Gas Chromatographic Analyzer for VOC Mixtures Encountered in the Industrial Workplace, *poster presentation*, MBSTP/BI Symposium, Ann Arbor, MI. May 3rd, 2017.
- J. Wang, N. Nuñovero, Z. Lin, Z, R. Nidetz, S. Buggaveeti, K. Kurabayashi, W. H. Steinecker, E. T. Zellers, A Wearable MEMS GC for Multi-Vapor Determinations, *poster presentation*, The Karle Symposium, Ann Arbor, MI, July 25th, 2016.
- J. Wang, N. Nuñovero, Z. Lin, Z, R. Nidetz, S. Buggaveeti, K. Kurabayashi, W. H. Steinecker, E. T. Zellers, Wearable Microfabricated Gas Chromatography for Volatile Organic Compound Complex Determinations, *poster presentation*, WIMS IAB Meeting, Ann Arbor, MI, May 19th-20th, 2016.

END OF REPORT

Signed:

E. T. Zellers, PI